Republic of Iraq

Ministry of Higher Education and

Scientific Research

University of Babylon

Faculty of Materials Engineering

Department of Metallurgical Engineering

Hardfacing of Low Alloy Steel with WC-Ni Composite by Tungsten Inert Gas Process

A Dissertation

Submitted to the Council of the Faculty of Materials Engineering/University of Babylon in Partial Fulfillment of the Requirements for the Master Degree in Materials Engineering/Metallurgical Engineering

by

Hawraa Najim Abdoun Majeed

Supervised by

Asst. Prof. Abdul Sameea J. A. Z. Jilabi (Ph.D)

2023 A.D **1444 A.H**

بِسْمِ اللَّهِ الرَّحْمَٰنِ الرَّحِيمِ

﴿وَمَا تَوْفِيقِي إِلَّا بِاللَّهِ عَلَيْهِ تَوَكَّلْتُ وَإِلَيْهِ أُنِيبُ﴾

صدق الله العلي العظيم

(سورة هود اية 88)

Dedication

This dissertation is lovingly dedicated to

Lord of the Age (Alimam Almahdi).

☆ ☆ ☆

Acknowledgements

Thank be to Allah for reaching where I am now. I wouldn't have reached what I've reached had it not been for God empowering me. Praise be to Allah first and last.

To whom was his endless giving continually ashamed me. To the one who supported me and straightened me in my difficult journey, the spiritual father (**Asst. Prof Dr. Abdul Sameea Alkilabi**). My thanks and gratitude to you has no limit.

To whom I wish was his presence: my father, may Allah have mercy on him.

To the one who his presence strengthens me, and I share him in my affairs. To my third father: my husband. My thanks and gratitude are to him.

Supervisor Certificate

I certify that this dissertation entitled "**Hardfacing of Low Alloy Steel with WC-Ni Composite by Tungsten Inert Gas Process**" is prepared by **(Hawraa Najim Abdoun Majeed)** under my supervision at the Department of Metallurgical Engineering/ Faculty of Materials Engineering/University of Babylon in partial fulfillment of the requirements for the Master Degree in Material's Engineering/Metallurgical Engineering.

Signature:

Name of Supervisor:

Assist. Prof. Dr. Abdul Sameea J. A. Z. Jilabi

Date: / / 2023

ABSTRACT

Nowadays, surface modification of steel alloys has become a necessity for the scientific and industrial communities. Tungsten inert gas (TIG) cladding is one efficient way to modify the surfaces of these alloys. This study aims to probe the effect of tungsten carbide-nickel (WC-Ni) composite coatings deposited using TIG cladding on the surface properties of low alloy steel substrates. The study also aims to explore the influence of the mass fraction of WC in WC-Ni composite coatings, and heat input corresponding to the TIG cladding current intensities on these properties. 1mm thick pre-placed composite pastes with different wt.% of WC (30, 40, 50, 60 and 70) were used to deposit the coating layers using various current values (80, 120, 130 and 140A). The findings revealed a distinct clad layer-substrate interfacial bonding in all the coated samples except that showed a destructive clad layer resulting from the deposition of a 70% WC-Ni composite using a current value of 80A. The defective regions were tiny compared to the whole cross sections of the clad layers. Optical and scanning electron microscopy exhibited various microstructures across the clad layers, mostly nickel solid solution dendrites with WC particles distributed through the matrix. Based on the cooling rates and the dense of WC in the composite, the dendrites at different locations across the clad layers were few or dense, finer or coarser, equiaxial or columnar, densely or less densely branched. In addition to the large columnar grains, tiny grains at the clad-substrate interface were predominant on the coating sides. A fairly large sized of WC particles that remained intact were distributed heterogeneously through the matrix of some clad layers. Increasing the cladding current intensity was however not sufficient for the decomposition of the WC. The energy dispersive spectroscopy proved that the Fe element that picked-up from the substrate material to the molten pool was mainly concentrated in the matrix rather than the dendrites, while the distribution of W element clearly indicated the locations and orientations of dendrites.

Vickers micro-hardness significantly increased with increasing the content of WC in the composite of the clad layer. The highest average hardness value was 756HV for the clad layer deposited with 60% wt. of WC in the composite and 120A current value, which is about 2.9 times that of the substrate material. Increasing the current values to 130A and 140A for the clad layers deposited with 70% WC increased the hardness to some extent, while the hardness notably increased to 850HV with the current reduced to 80A. Increased hardness in a region was not necessarily associated with a decreased rate of weight loss during wear in that region. Increasing the wt.% of WC in the coating layers generally presented a lower rate of weight loss and thus an increase in wear resistance. Increasing the current value to 130A and 140A for the clad layer deposited with 70% WC decreased the weight loss rate (9.5×10^{-6} and 6.4×10^{-6} g/m respectively). A remarkable decrease in the rate of weight loss (2.83×10^{-6} g/m) was as a result of decreasing the TIG cladding current intensity to 80A (with 70 wt.% WC), for the sample showed a destructive coating layer and somewhat improper interfacial bonding with the substrate. However, the weight loss mostly decreased with increasing the wear test sliding distance.

List of Tables

List of Figures

Table of Abbreviations and Symbols

CVD	Chemical Vapor Deposition
PVD	Physical Vapor Deposition
WC	Tungsten Carbide
Ni	Nickel
TIG	Tungsten Inert Gas
GTAW	Gas Tungsten Arc Welding
wt.%	Weight Percentage
EB	Electron Beam
HAZ	Heat Affected Zone
MMA	Manual Metal Arc
MIG	Metal Inert Gas
SAW	Submerged Arc Welding
DCEN	Direct Current Electrode Negative
DCSP	Direct Current Straight Polarity
DCEP	Direct Current Electrode Positive
DCRP	Direct Current Reverse Polarity
AC	Alternating Current
Ar	Argon
He	Helium
MMC	Metal Matrix Composite
H	Heat Input Per Unit Length
V	Voltage
I	Current
S	Scan Speed
D	Dilution Ratio
WF	Widmanstatten Ferrite

AF	Acicular Ferrite
μ	Friction Coefficient
W	Applied Force
v	Slip Speed
Q	Heat Generated
Wr	Wear Rate
Δm	Loss of Mass
F	Applied Force
L	Travelled Distance
ρ	Coating Density
CGHAZ	Coarse Grained Heat Affected Zone
FGHAZ	Fine Grained Heat Affected Zone
ICHAZ	Intercritical Heat Affected Zone
SCHAZ	Subcritical Heat Affected Zone
BM	Base Metal
LCT	Laser Coating Texturing
OM	Optical Microscopy
SEM	Scanning Electron Microscopy
EDS	Energy Dispersive Spectrometer
AISI	American Iron and Steel Institute
PVA	Polyvinyl Alcohol
HV	Vickers Hardness
La	Lanthanum
Al	Aluminum

List of Contents

CHAPTER ONE:

INTRODUCTION

CHAPTER ONE: INTRODUCTION

1.1 General View

Alloy steels have been developed for several reasons, one of the most important being to overcome the limitations of employing carbon steels. It is difficult to obtain superior tensile strength when using carbon steel if ductility and toughness are desired as well. Carbon steels also have a low corrosion resistance [1,2]. Alloy steels are generally stronger and have better thermal and corrosion resistance than carbon steels, along with other properties such as machinability, hardenability, and ductility. This is attributed to the effect of alloying elements added to steels in different quantities [3]. Alloy steels are typically used in a variety of applications. The most common of which are oil and gas industries, gas turbine components, storage tanks and industrial equipment [4].

Low alloy steels made some progress in vehicle structural applications before becoming the preferred material. Mass reduction potential of these steels has been clearly demonstrated in the theoretical literature, experimental applications and industrial equipment [4].

Surface modification has recently become necessary for the scientific community because the surface properties of wettability, adhesion, hardness, corrosion and wear resistance of new materials are frequently inadequate. Furthermore, it is difficult to find an alloy with a different surface behavior than the bulk for various reasons. In order to improve properties in metals and alloys suitable for severe environments, strategies of surface modification depend on a direct action on the metal/alloy or incorporating coatings provide these properties or functionalize its surface for complex requirements have to be applied. The most significant of these properties are corrosion and wear resistance, mechanical and fatigue strength, thermal, magnetic, electrical, or even their combined effect [5].

Some of the most generally used surface treatment procedures are induction hardening, carburizing, nitriding and deposition techniques such as chemical vapor deposition (CVD), physical vapor deposition (PVD), electrolytic coating, and hardfacing. Hardfacing methods include laser cladding, TIG cladding, thermal spraying, and others [6]. Figure (1.1) shows some of the most significant applications of TIG cladding technique.

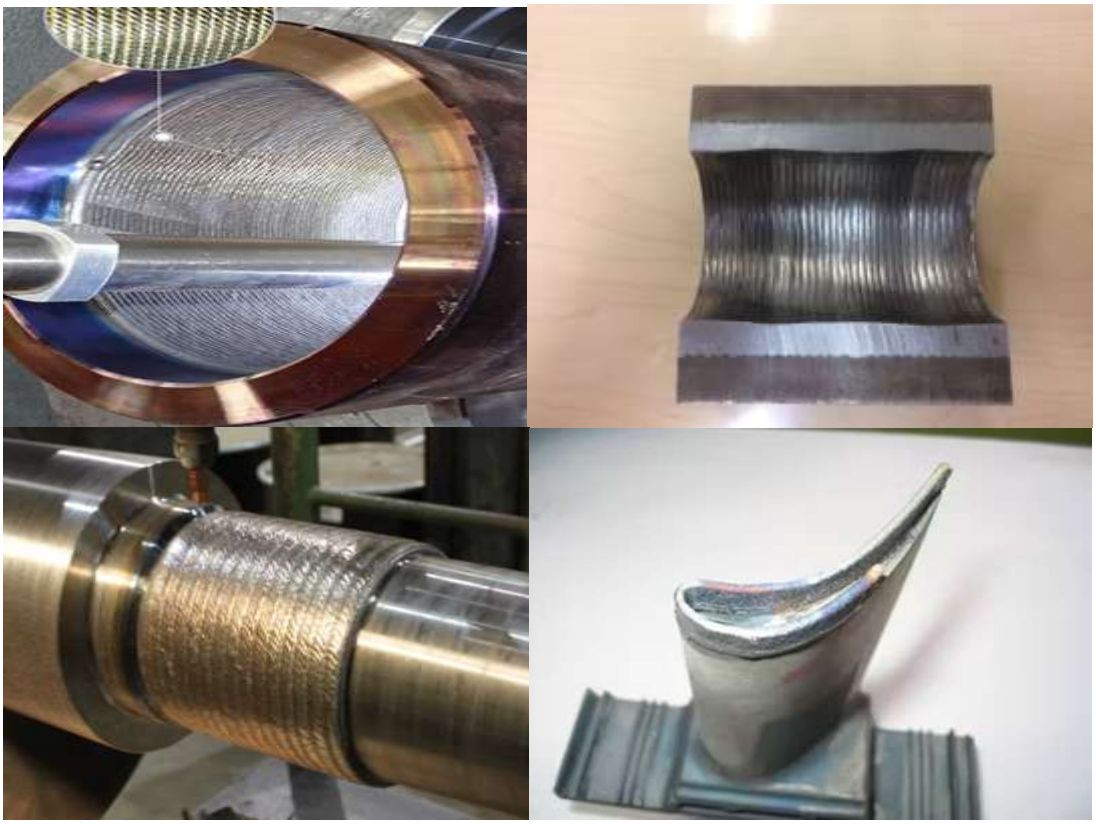

Figure (1.1): Some applications of TIG cladding technique.

1.2 The Benefits of Cladding

- Modifying the surface properties without affecting the interior.
- Producing an excellent metallurgical bonding between the clad layer and the substrate.
- Cost-effectiveness technique.
- Increasing hardness, wear and/or corrosion resistance of surface.
- A wide range of clad layer materials can be used [7].

1.3 The Objective of this Study

The aim of this study is to investigate the influence of tungsten carbide-nickel (WC-Ni) composite coatings deposited using tungsten inert gas (TIG) cladding on surface properties of low alloy steel substrates. The study also aims to explore the effect of the mass fraction of WC in WC-Ni composite coatings, and heat input corresponding to the TIG cladding current values on these properties.

1.4 Dissertation Outline

This dissertation consists of five chapters. The present chapter deals with a general introduction as well as the objective of this study. Chapter two provides important details about the material being used as a substrate (low alloy steel), and the reason behind using it, its applications, the effects of alloying elements, and the WC-Ni clad layers by TIG cladding technique. A literature review also given in this chapter. Chapter three precisely describes the experimental part, where low alloy steels were used as a substrate. WC-Ni powder was also used. Preparation of specimens for physical and mechanical testing were described as well. In chapter four, the results of the experimental work on low alloy steel substrate were analyzed and discussed. Lastly, chapter five deals with the most significant conclusions in addition to future recommendations for other researchers.

CHAPTER TWO:

THEORETICAL PART &

LITERATURE REVIEW

CHAPTER TWO: THEORETICAL PART AND LITERATURE REVIEW

2.1 Introduction

This chapter explains low alloy steels and their surface modification by cladding using the gas tungsten arc welding (GTAW) process; the principle work of this process, in addition to gases and fillers used with GTAW of low alloy steels. Additional details about the metallurgical impacts of the thermal cycle of gas tungsten arc steel welds have been dealt with. Literature review for studies about the current work has been highlighted too.

2.2 Low Alloy Steels

Low alloy steels can be defined as metal mixtures composed of steel and other elements. They typically contain about (1-5%) of alloying elements to enhance the mechanical properties [8].

Low alloy steels have significant advantages such as high yield strength, ability to withstand high temperatures, good creep strength, oxidation resistance and low temperature ductility [9].

Low alloy steels can be classified according to [10]:

1- The chemical composition, such as nickel steels, nickel-chromium steels, molybdenum steels, chromium-molybdenum steels.
2- Heat treatment, such as quenched and tempered, normalized and tempered, annealed.
3- The weldability.

Storage tanks, oil and gas pipelines, bridges, towers of power transmissions, light poles, industrial equipment, off-road and heavy-duty high way vehicles, farm and construction machinery, passenger car components, mine and railroad cars, building beams and panels, the automotive, heavy equipment, aerospace and lawn mowers etc., are common applications of low alloy steels [11,12].

2.2.1 Alloying Elements

Alloying elements are widely added to steels for several significant functions, including greater strength, increasing hardenability, corrosion resistance, grain size control and improving ductility, machinability and mechanical properties at both low and high temperatures [13,14].

The most usual alloying elements added to steels are as follows [10]:

1. Carbon: affects hardness, tensile strength, machinability and the melting point.
2. Manganese: contributes markedly to increasing hardness and strength. It also reduces both ductility and weldability when presented in a high weight percentage (wt.%) with a high carbon content in steels.
3. Silicon: improves the strength and oxidation resistance of low alloy steels.
4. Nickel: enhances toughness and thus the impact resistance. A high percentage of nickel increases corrosion resistance.
5. Chromium: is usually added to attain deep hardenability with better abrasion resistance. It also assists avoiding oxidation and corrosion.
6. Molybdenum: raises the hardenability of steels, refine grains, in addition to the increase of creep and tensile strengths at high temperatures.
7. Vanadium: encourages fine granules in steel and increases strength while maintaining ductility.

8. Tungsten: provides higher hardness and strength at high temperatures, resists heat and promotes micro grains.

9. Cobalt: contributes to obtaining the red hardness by hardening of ferrite.

10. Copper: when added with a (0.2-0.5%) to steels, it improves resistance to atmosphere corrosion and acts as a strengthening agent.

2.3 Surface Modification of Steels

Steel components are the most widely utilized materials in modern industry due to their massive advantages, which involves its excellent mechanical properties and economic manufacturing cost [15]. Many industrial components work continuously in severe conditions such as high temperatures and stresses, cyclic forces, high pressure and impacts, which cause wear and damage of the components. In order to improve the efficiency and increase service life, these components require treatments to modify the surface characteristics. Various surface modification techniques are typically used to improve the surface properties such as hardness, wear and corrosion resistances of steels without changing their interior properties [16]. Several of these techniques are based on applying thin films of functional materials with superior surface properties to a substrate [17].

Different kinds of hardening techniques such as induction hardening, carburizing, nitriding and deposition techniques such as chemical vapor deposition (CVD), physical vapor deposition (PVD), electrolytic coating and hardfacing are some of the widely used surface treatment techniques. Laser cladding, TIG cladding and thermal spraying are commonly types of hardfacing techniques [6].

Various approaches to the different surface hardening techniques are as follows [18]:

1. Thermo-chemical diffusion techniques, which modify the surface composition using elements such as carbon, nitrogen and boron.

2. Energy or thermal techniques, which improve required properties without changing the surface composition by altering the surface structure using a quench hardening, with no alloying elements added.

3. Surface coating techniques, which include creating or adding new layer/s on the substrate.

2.3.1 Thermo-chemical Diffusion Techniques

There are many techniques used to modify surfaces depending on the change of the chemical composition of the surfaces by diffusion of elements [19].

- **Carburizing**: It is widely used for low carbon steels, which involves heating the steel in a carbon rich medium at temperatures (850-980)°C followed by quenching in order to harden the surface layer.

- **Nitriding**: In this technique, surface hardening of steels is carried out by introducing nitrogen into the steel surface with temperature range of (500-550)°C.

- **Carbonitriding**: It depends on the diffusion of carbon and nitrogen into steels resulting in the formation of hardened surface layers with temperatures lower than that of carburizing.

- **Boronizing**: Using this technique, the creation of hard boron compound at the material surface can be achieved by a thermo-chemical diffusion of boron atoms into the base material. The temperature of boronizing (sometimes called boriding) ranges from 700°C to 1000°C. This technique can be applied to any ferrous and nonferrous material.

The surface hardness obtained using these techniques is typically 750-1600 HV, and can be reached with boriding up to 2800HV.

2.3.2 Applied Energy Techniques

These involve traditional heat treatments such as induction hardening and flame hardening in addition to high energy treatments such as electron beams and lasers [20].

- **Induction hardening**: This technique is used to acquire higher hardness, fatigue life and wear resistance by creating a hard surface layer, without affecting the core microstructure. The alternating current applied to the copper coil causes heating the workpiece which is placed inside the coil resulting in an induced alternating magnetic field within the workpiece. This raises the temperature of the outer surface of the part to or above the transformation range. This technology is followed by rapid cooling.

- **Flame hardening**: It is used to obtain higher hardness and wear resistance of the medium carbon or alloy steels. The steel is heated by an oxy-flame at an elevated temperature followed by quenching to form a hard and wear resistant surface layer.

- **Laser surface heat treatment**: This technique is widely used to harden components made of steel and cast iron. It is sometimes named as laser transformation hardening. In this technique, a hardened layer is formed on the base metal due to the interaction of the metal with a laser beam [21]. It improves wear and fatigue resistances with minimal distortion. It includes heating the material to the austenitizing temperature. It involves different techniques like surface melting and surface alloying.

Surface melting is used to modify surfaces by heating the base metal to its melting temperature, followed by rapid solidification, which improves the surface properties such as wear and corrosion resistances.

In *laser alloying*, the required properties of the surface are obtained by melting and mixing alloying elements on the surface with no effect on the bulk material [22].

- **Electron beam (EB) hardening**: In this technique, a high-speed electron beam impinges the surface to be hardened resulting in heat the material to the austenitizing temperature, followed by self-quenching.

2.3.3 Surface-modification by Coating Deposition

There are many techniques utilized to modify surfaces depending on creating or adding new layers on the substrate [23].

- **Chemical Vapor Deposition (CVD)**: It is a chemical process utilized to deposit a wear resistant coating on a substrate with metallurgical bonding. This technique creates a thin film coating on the substrate as a result of the reaction or deposition of volatile gaseous phases on the substrate surface to obtain the required coating.

- **Physical Vapor Deposition (PVD)**: Similar to CVD, it is also used to produce a thin film coating. It is essentially a high-temperature vacuum deposition technique, in which the coating material is vaporized that forms a compound during interacting with a nitrogen or carbon containing reactive gas. As a result, a thin coating with improved hardness and high quality adhesives is deposited on the substrate surface. The coating material can be evaporated by heating or sputtering of ions to enhance high density.

- **Electroplating**: It is also called electrodepositing. In this technique, a metallic coating is deposited on a metal substrate through an electrochemical process. Thus, the properties of the workpiece surface chang**e.** The coating is carried out inside a container contains a solution of one (or more) metal salts and the workpiece to be coated is connected to cathode of an electrical circuit. When the current is applied, ions are attracted from the solution towards the cathode, and then deposited on the workpiece. Steel, nickel and copper based alloys are widely used in the electroplating technique.

- **Electroless plating**: It is an auto-catalytic reaction technique used to deposit a nickel or copper coating onto the substrate surface without an applied current. As a result, a completely uniform deposit is achieved, even with complex shapes, for improving wear resistance.

- **Hardfacing**: It involves applying a layer or layers of material with superior properties to the substrate surface. Thermal spraying, laser cladding and welding are different types of hardfacing to deposit a wear resistant material to the chosen areas of the components. It can also be used to repair worn parts. The most widely hardfacing materials used for wear resistance are nickel, cobalt and iron/chromium alloys.

2.4 Different Types of Hardfacing Techniques

2.4.1 Thermal Spraying

In this technique, a material in the form of a molten powder is sprayed onto the substrate surface to provide a coating. The powder is typically melted by an oxy-fuel flame to be sprayed as a fine spray. The resulting coating layer is thick with a deposition rate higher than any other coating techniques like electroplating, PVD and CVD [24].

2.4.2 Laser Cladding

It offers a wide range of possibilities to change the microstructure and therefore mechanical properties of the substrate surface. Using a laser beam, a thin layer of the surface is melted and then mixed with molten clad powder alloys to form a metallic bond. It introduces several advantages over various conventional coating techniques including narrow heat affected zone (HAZ), low dilution and low heat input. It results in a strong metallurgical bond between the cladding layer and the substrate. It has been used for depositing various powder mixtures such as tungsten carbide-cobalt, and satellite on steel, cast iron and titanium alloy substrates. It has different applications in boiler firewall, engine valve components and turbine blades [25].

2.4.3 Hardfacing by Welding

It is used to deposit a wide variety of coating materials on the substrate surface with a high bonding strength. Different welding processes can be utilized for hardfacing or cladding such as manual metal arc (MMA), metal inert gas (MIG), tungsten inert gas (TIG) and submerged arc (SAW). These processes differ in efficiency, dilution ratio and deposition rate. Cladding by welding however results in deposit relatively thick layers with high deposition rates [26,27].

2.5 Tungsten Inert Gas Welding

Tungsten inert gas (TIG) welding or sometimes called gas tungsten arc welding (GTAW) is a process that depends on melting and joining metals being welded by heating them with an electric arc ignited between a non-consumable tungsten electrode and the metals (workpieces), as shown in Figure (2.1). The torch that holds the tungsten electrode is connected to one terminal of the power supply as well as a cylinder of a shielding gas, as shown in Figure (2.1a). Usually, the tungsten electrode is in contact with a

water cooled copper tube, named the contact tube (Figure 2.1b), connected to the terminal by a welding cable (cable 1). This connection makes the welding current flows from the power supply to the electrode in addition to cooling the electrode to avoid overheating. The other terminal of the power supply is connected to the workpiece using another cable (Cable 2). The shielding gas flows through the torch and is directed towards the weld puddle by a ceramic nozzle to avoid contamination of the weld from atmosphere. This protection in the TIG process is much better than in SMAW process due to the usual use of an inert gas such as argon or helium as the shielding gas, in addition to directing the shielding gas towards the weld puddle. For this reason, this process is called tungsten inert gas welding. In special cases, active gases can be mixed in small quantities to the shielding gas. Therefore, GTAW is considered a more suitable name for this welding process in these cases. A filler rod, if required, for example, for joining thicker metals, can be fed separately either manually or sometimes automatically into the electrical arc [28].

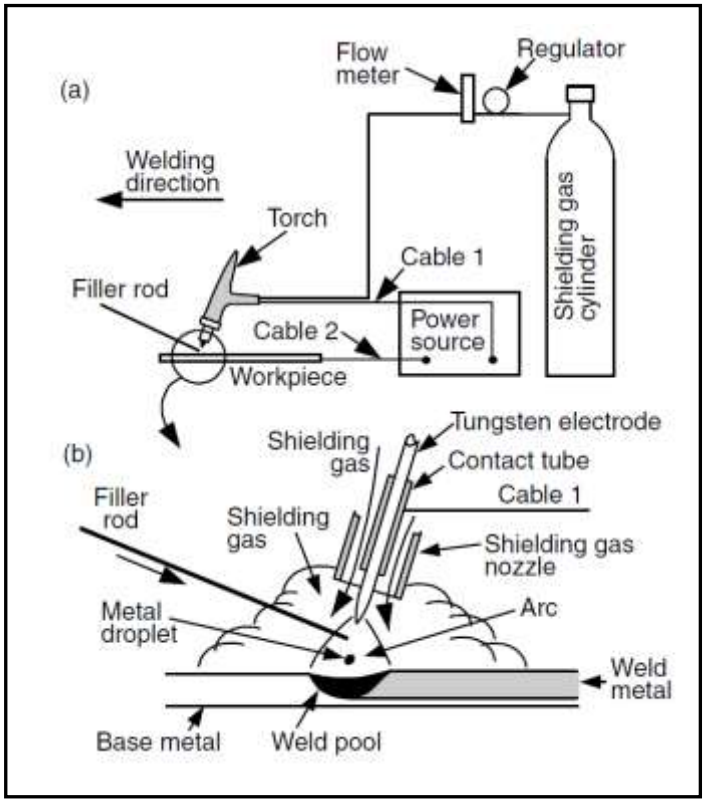

Fig. (2.1): Principle work of the TIG process, a: overall b: enlarged welding area [28].

2.5.1 Polarity

There are three different polarities can be used with the TIG welding process as follows [28]:

A. Direct Current Electrode Negative (DCEN), sometimes called the direct current straight polarity (DCSP), is considered the most common polarity used with the TIG welding process. With this polarity, the tungsten electrode is connected to the negative terminal of the power source (Figure 2.2a). Electrons are released from the electrode and then accelerated whilst moving through the arc. In the TIG welding process with the DCEN polarity, more power, about two thirds, is located at the workpiece end of the arc and less power, about one third, at the electrode end. Therefore, a weld bead with a relatively narrow and deep penetration is produced.

B. Direct Current Electrode Positive (DCEP) is sometimes called the direct current reverse polarity (DCRP). With this polarity, the tungsten electrode is connected to the positive terminal of the power supply (Figure 2.2b), and about two third of the power in located at the electrode. Thus, a weld bead with a relatively wide and shallow penetration is produced. Therefore, this polarity can be utilized for welding thin workpieces of strong oxide forming metals such as aluminum and magnesium and their alloys, where deep penetration is not desired. Moreover, water cooled large diameter electrodes have to be used to prevent melting the electrode tip.

C. Alternating Current (AC) gives a moderate penetration between the two polarities above (Figure 2.2c).

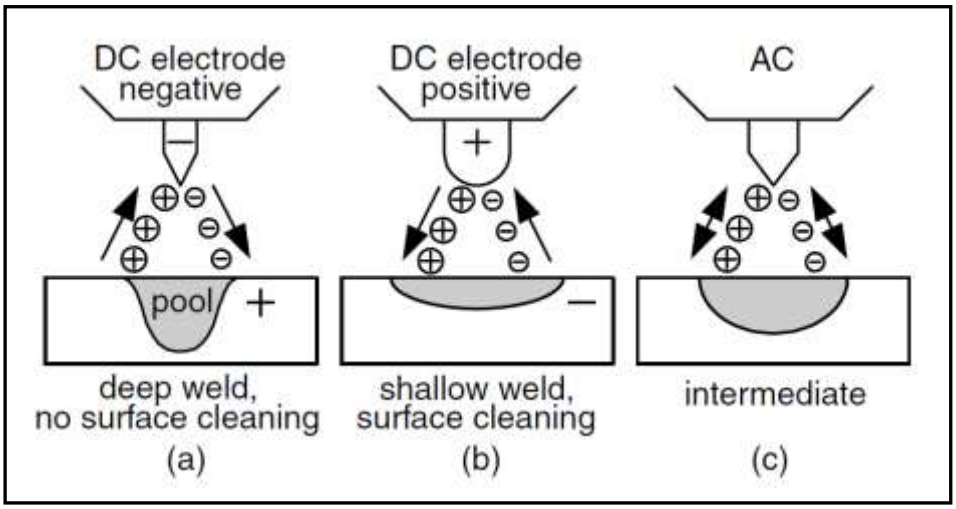

Figure (2.2): Three different polarities used with the TIG welding process [28].

2.5.2 Electrodes

Tungsten electrodes containing 2.0% thorium, zirconium or cerium have better emissivity of electrons, capacity of current carrying and contamination resistance than pure tungsten electrodes. Therefore, arc ignition is easier and the electrical arc has more stability. Lower emissivity of electrons needs the electrode tip to have higher temperature in order to increase releasing the electrons, and therefore a greater risk of tip melting [28,29].

2.5.3 Shielding Gases and Filler Metals

Both argon (Ar) and helium (He) can typically be used as shielding gases. The "ionization potential" of Ar (15.7eV) is lower than He (24.5eV), therefore, Ar is easier to ionize. As a result, arc ignition is easier and the drop in voltage across the arc is less with Ar. Since Ar is heavier than He, it provides more efficient protection and higher resistance to atmosphere draft. Also, Ar has a greater action of oxide removing with DCEP or AC polarity. These advantages along with the lower cost of Ar make it more suitable to use with the TIG welding process than He. However, higher power input and greater sensitivity to changes in the arc length can be occurred with He due to its larger voltage drop across the arc. Finally, He offers the welding thicker sections and with higher welding speeds. On the

other hand, Ar gives more controlling the arc length during the automatic TIG welding process [28].

Filler metals are generally used for welding thicker sections with beveled edges. It is preferable for the filler metal to have the same chemical composition and diameter with the same thickness as the base metals to be welded. For the TIG welding process, filler metals are supplied as wires in the form of cut lengths or coiled around special spools [30,31].

2.5.4 Advantages and Limitations of Tungsten Inert Gas Welding

The TIG welding process is appropriate for joining thin sections due to its ability to the use of low current values. The feed rate of the filler metal is independent on the welding current value to some extent, resulting in the relative amount of the base metal and the filler metal fusions to vary. Consequently, the dilution and heat input into the weld can be controlled without changing the weld pool size. This process can also be utilized to butt-weld thin sections by fusion alone, i.e., without adding filler metals. Because the TIG welding is a very clean welding technique, it can be utilized to join reactive metals, for instance, aluminum, magnesium, titanium and zirconium. On the other hand, the deposition rate using the TIG process is low. Excessive values of the welding current can result in the tungsten electrode to melt and lead to brittle inclusions of tungsten in the weld metal [32].

2.6 Tungsten Inert Gas Cladding

TIG cladding has proven to be one of the most common and economical techniques for surface coating processes, which can easily offer a metallurgical bonding between the substrate material and clad layer [33]. TIG surface coating produces surface modification through melting alloy powders or mixture of powders or powders pasted on the substrate [34]. The resulted surface layer on different substrate materials has a fine

microstructure with higher hardness and wear resistance than those of the substrate [35].

TIG surface coatings offer several advantages in depositing hard and wear resistant layers on a wide range of substrates by melting both the coating material and a thin layer of the substrate simultaneously [6,36]. In comparison with other techniques, thick deposits, within a few millimeters, can be obtained by this technique [37]. Figure (2.3) shows the principle work of this technique.

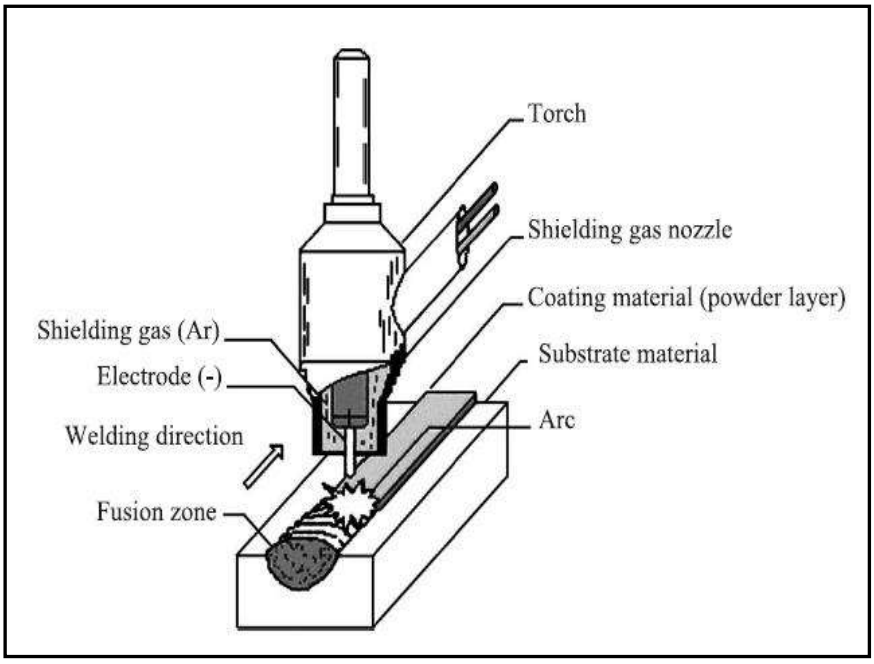

Figure (2.3): Schematic representation of the principle work of the TIG cladding [38].

2.6.1 Advantages and Disadvantages of the TIG Cladding

The TIG cladding has several advantages over other techniques as follows [39]:

1. High deposition rate and low dilution.
2. High portability.
3. Wide availability.
4. Low equipment cost.
5. Suitable for a wide range of materials.
6. Manual and automated operations are possible.

It however has some disadvantages like:

1. Slow compared to other techniques such as laser coating.
2. Produces large HAZ and sometimes surface deformation occurs if the operating conditions are not suitable.

2.6.2 Applications of the TIG Cladding

Below are some of the most important applications of this technique [39]:

1. Repair of worn parts operating under severe service conditions.
2. Protective protection for specific areas or entire workpiece to withstand severe wear conditions such as corrosion and abrasion.
3. Oil and gas industries.
4. Gas turbine components.

Figure (1.1) shows some of these applications.

2.7 Metal Matrix Composite Coating

Nowadays, coatings by the use of hard ceramic particles to produce a metal matrix composite (MMC) layer are gaining wide popularity [40]. In industries, ductile materials have significant limitations of low wear resistance, which can be improved by applying a coating layer of a hard material to the substrate surface. Typically, most of the hard materials are brittle by nature, and thus break during wear. The broken particles also contribute to wear. MMCs have however an incorporated advantage of ductile and tough matrix with hardness and superior compressive strength of carbide. MMCs have hard carbides such as TiC, WC or TiB_2 with matrices such as Fe, Co or Ni ordinarily exhibit high hardness and wear resistance. Coating by MMC layer can however be achieved easily using the TIG cladding [41].

2.7.1 Tungsten Carbide Reinforced Metal Matrix Composites

Generally, hard ceramic particle reinforced MMCs retain high hardness, strength and wear resistance compared to the base substrate, along with superior toughness than the composite ceramics [42]. However, fabrication of entire MMCs is considered wasteful and uneconomical due to the complexity of manufacturing in addition to the high cost of the reinforcement ceramic particles [43]. Layer/s of ceramic particle reinforced MMCs on the substrate surface created by deposition techniques of high energy density such as thermal spraying, laser cladding and TIG cladding can modify the surface properties without affecting the bulk characteristics of the components [44]. Despite, different hard ceramic materials are beneficially employed as particle reinforcement in the MMCs, WC has been proved to be a promising choice as a coating in various engineering components. This is due to its high hardness and melting temperature with excellent corrosion and wear resistance, in addition to its stability at high temperatures, which makes it widely used in cutting tools, excavation drills and corrosion resistant coatings [45-49]. As compared to other reinforcement carbides, WC has favorable properties, such as high hardness (3,000–4,000HV) [50], good wettability by molten metal matrices, and a certain value of plasticity [51,52].

Recently, the laser cladding has been widely used to build up thick coatings of WC or WC reinforced MMCs on different substrate materials [45,53,54]. The speed of this technique is high, and by selecting appropriate variables, MMC surface layers with a thickness of several millimeters can be obtained [55,56]. Although these particular advantages, applying laser surface modification is improper in industries due to the complexity of the technique, and the high cost of the equipment. Alternatively, TIG cladding is a low cost technique for depositing thick coating layers, due to its ease of use and low setup cost [57]. The deposited layers by this technique are not very different from that deposited by laser

[58-60]. However, the layer deposited by the TIG cladding has a thickness of almost twice that deposited by laser [61-63].

The major issue related to laser cladding is the formation of defects such as cracks, surface roughness and cavities, which can be minimized by employing the TIG technique. In order to reduce the possibility of cracking, preheating of the base substrate is typically used [64,65].

Some researchers have interested on TIG cladding by the use of WC and W_2C as reinforcement on different substrate materials such as AISI 1010 steel [66] and AISI 1016 steel [67]. The resulted WC reinforced coating demonstrated a considerable improvement in the hardness and wear resistance values than the substrate material. However, the main challenge associated with the production of WC reinforced steel-composite coating is to achieve a suitable interfacial bonding. In order to obtain a proper bonding between the steel substrate and the WC particles, an interfacial material such as Ni or Co, which offers a high wetting property between them, should be provided [68]. With thermal spraying technique, these interface materials create a separate layer between the steel substrate and the ceramic coating with a minimum ratio of dilution [69]. A similar situation might also occur with the laser cladding technique [70]. With the TIG cladding technique, pre-placed coating layers of pure carbide ceramic particles might result in arc interruption due to the low electric conductivity of carbides, thus reducing the efficiency of the technique. Appropriate bonding metal additives with carbide particles reduce the current required, and thus the heat input to the substrate. This may minimize the HAZ width, and thermal stresses induced in the substrate [71]. At elevated temperatures (molten state), the solubility of carbides in the Ni matrix increases, and thus improves the strength of bonding between the carbide particles coating and the steel substrate, which then increases the wear resistance of the coating [68]. Several studies have been carried out to improve the strength of the

WC reinforced MMC coating by Ni or Ni-based matrix as a binding material for various high energy density techniques [66,67,72,73]. Due to the higher wettability of the Ni element with hard carbide particles, the addition of Ni improves the surface properties of the fabricated components [74]. However, with the carbide-Ni composite coatings produced by the TIG cladding technique, the current and scan speed of the arc have noticeable effects on the microstructure and mechanical behavior [75].

2.7.2 Microstructure of WC-Ni Composite Coatings Produced by the TIG Cladding Technique

Solidification is the first transformation that takes place in the molten pool. The solidification mechanism of metals is summarized through nucleation and grain growth, as in the case of solidification that occurs in castings. The molten pool typically solidifies within few seconds owing to very rapid cooling rate caused by the heat absorbed by the cold, relatively large sized substrate. The heat lost due to radiation to the atmosphere is really another cause [30]. It is indicated that the heat input (energy input) in the TIG cladding technique is dependent on the applied current, voltage and travel speed as in the equation suggested by Mridha and Baker (2015) [40] below:

$H = \eta (V.I/S.1000)$ …… (1),

where: H is heat input per unit length (J/m), V, I, S are voltage (V), current (A) and scan speed (mm/s) respectively. The heat absorption efficiency ŋ is considered as 48%.

In steel alloys, the molten pool solidifies forming a solid solution of C, Mn and some other elements with iron. Based on cooling rate, the resulting grains might be dendritic or columnar. Heat typically flows from the molten pool towards the adjacent colder substrate metal. The coating layer therefore, has columnar grains with right angles to the fusion line. This is what distinguishes grains resulting from depositing a single layer.

With multi-layer cladding, and due to repeated heating, these grains transform into equiaxid grains, where each layer reheats the previous layer. The coating layer is generally a mixture of the pre-placed WC-Ni composite powders with the molten substrate metal. The mixing of a portion of the substrate metal with the powders is known as dilution process, which can be expressed as [76]:

$$\text{Dilution ratio (D) \%} = \frac{\text{weight of the molten parent metal}}{\text{total weight of the molten metal}} * 100 \quad \ldots\ldots\ldots\ldots (2)$$

It is worth mentioning that the first layer in the case of multi-layer cladding smelts a large proportion of the substrate metal in comparison with the subsequent layers.

The WC-Ni deposited coating will mostly have a dendritic structure resulted from the rapid solidification during the TIG cladding technique. Another cause for the dendritic structure could be the difference between the melting points of the molten pool constituents [66,67]. Since the temperature of the resulting molten pool is much lower than the melting point of the WC, it is expected that the deposited WC particles remain intact, without decomposition. However, some of the finer particles may suffer from decomposition or surface melting during contact with the molten constituents [77,78]. By increasing the weight percentage of WC particles in the molten pool, the dendritic structure becomes finer. This could be attributed to the fact that these particles act as an obstacle to the growth of dendrites [79,80]. In general, with cladding technique, the structure at the bottom of the molten pool is firstly planar and dentate towards the center and top of the pool, and then the structure becomes dendritic with releasing heat latent of solidification [67]. Due to the contact of the molten pool with the atmosphere, the solidification rate is higher, and the structure transforms into a fine dendritic. The presence of WC particles in the molten pool which activate the heterogeneous germination mechanism can be a cause of the denderitic microstructure [67].

WC particles tend to sink towards the bottom of the molten pool due to the large difference in powder densities between WC and Ni. The lower melting point and slower solidification rate of the Ni provide time for the WC particles to sink towards the bottom of the molten pool [66].

Microstructures of clad layers typically vary with the TIG cladding parameters such as coating thickness and heat input values [81]. In 2014, Tosun [66] proved that with increasing current intensity (power input), the composite needle-like Ni/WC alloy transformed into a spherical-shaped granular structure, and the higher heat inputs are effective in producing phases of higher temperature transformation, like pearlite.

2.7.3 Mechanical Behavior of WC-Ni Composite Coatings

Micro-hardness values mainly depend on the density and distribution of the hard carbide particles in the matrix, the size of the carbide particles in the coating, the molten pool profile and the morphology of the composite structure [82]. The microstructural characteristics are also strongly dependent on heat input values, which in turn lead to different microstructures [6].

High current values are known to increase heat inputs and to result in the lower cooling rates experienced by the molten pool. Low cooling rates allow the grains to grow considerably due to the longer solidification time and thus coarsening the grain structure. Micro-hardness values seem to be closely related to microstructures. Refinement of grain structure generally improves the hardness [83]. Typically, when the current increases, the hardness is expected to decrease due to the coarsening of the grain structures. On the contrary, Tosun revealed in 2014 [66] that the hardness of the WC-Ni composite coating layer increases significantly with increasing the current values. This could be attributed to the formation of Widmanstatten ferrite (WF), acicular ferrite (AF) and some bainite, and to the considerably high carbon content of the coating layer [84].

Tosun explained that the high hardness of carbides concentrated in high dendritic structures is another reason for increasing hardness. The micro-hardness of the composite coating matrix however increases with increasing the WC particles [81,85].

The friction coefficient (μ) of WC-Ni composite coating is generally related to the wear resistance [86,87]. With the increase of the WC amount in the WC-Ni composite coating, the μ decreases and the wear resistance increases. The decrease in the amount of μ can be clarified using Equation (3) below. With the increase of the applied force (W) and the slip speed (v), the heat generated (Q) at the surface increases [88,89]:

$$Q = \mu W v \qquad (3)$$

Increasing the temperature of the wear surface can result in two conflicting effects. The first effect is to decrease the strength and increase the softness, which increases the wear. Another effect is that increasing the temperature increases the oxidation rate at the wear surface forming a stable oxide film that reduces the contact between the wear surface and the disc, thus reducing the μ and wear rate [90,91].

The strong bond between WC reinforcement particles and the Ni matrix of the composite coating reduces the μ and wear rate. Such bonding makes it difficult for the WC particles to separate from the coating surface while sliding in the wear test at increased load [67].

To calculate the wear rate, Equation (4) is used [92]:

$$W_r = \frac{\Delta m}{F.L.\rho} \times 10^6 \qquad (4).$$

Where, W_r is the wear rate ($mm^3/N.m$), Δm is the loss of mass (mg), F is the applied force (N), L is the travelled distance (m), and ρ is the coating density (g/cm^3).

It is noteworthy that with certain high sliding distances, the slope of the wear rate curve may decrease. The reason behind this could be the accumulation of dislocations and the formation of cold work in the layers below the abrasive surface [91,93]. Extremely increasing the mass fraction of the WC reinforcement particles generally reduces the amount of matrix phases between these particles. In some cases, this decrease reaches to the extent that the particles come into contact with each other. This phenomenon minimizes the supporting effects of the WC reinforcement particles in decreasing wear rates, and in some cases increase the wear rate as well [94,95]. However, at the onset of the wear test, the wear rate is normally fast, and after a while, the wear rate becomes steady [96].

2.7.4 Thermal Effects of TIG Cladding Technique on the Substrate and its Mechanical Properties

The substrate metal adjacent to the molten pool is typically divided into two zones:- the heat affected zone (HAZ), and unaffected metal.

2.7.4.1 Heat Affected Zone

It is the region just adjoining to the molten pool which represents the substrate metal that is not melted by the cladding heat, but is heated to a temperature and for a sufficient time for grain growth to occur.

This region experiences complex thermal cycles represented by the sudden heating of different temperatures, ranging from the melting temperature to that of the unaffected metal. Consequently, the heating is followed by fast cooling due to the nearby cold metal and the surrounding air. This heating and cooling cycle acts as a different heat treatment for each region of the HAZ. Hence, this zone consists of a series of structures gradient and different in their mechanical properties. In low alloy steels, these structures might vary from hard martensite to coarse pearlite. When TIG cladding low alloy steels with a single layer, three different metallurgical regions may be observed: grain growth region, grain refined region and transition region.

A. Grain Growth Region: it is exactly adjoining to the interface line (molten zone). In this region, the substrate metal is heated to temperatures ranging from above the upper critical temperature (A3) to melting temperature (Figure 2.4). This results in coarsening the structure or grain growth. The largest grain growth region and maximum grain size take place with the slowest cooling rate. The cooling rate depends on the amount of heat generated during cladding, the initial temperature of the substrate metal, as well as the thickness of the substrate and the clad layer. The high initial temperature of the substrate and high cladding heat result in slow cooling rates, while the large substrate thickness results in a fast cooling rate. The cooling rate of this region is generally greater than those in the other regions of the HAZ, because of the extreme thermal drop from the temperature of this region to that of the cold substrate metal. This region is therefore the hardest of the HAZ of low carbon steels [97].

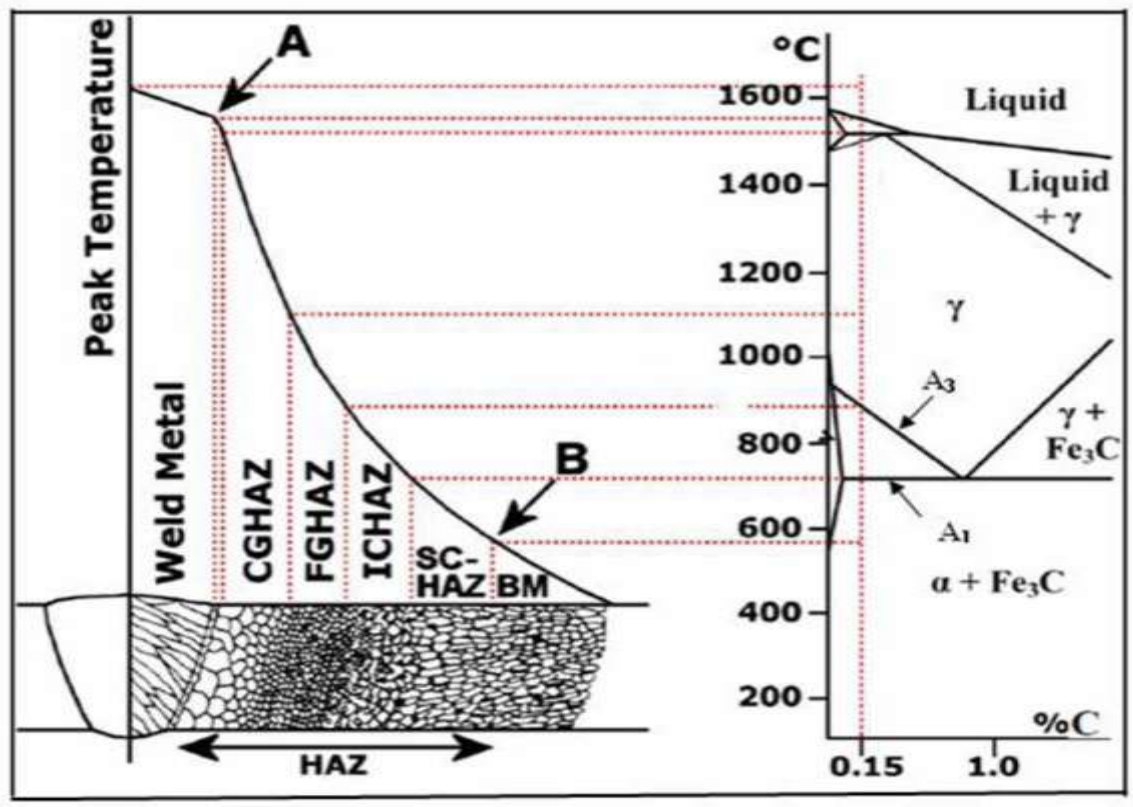

Figure (2.4): The Fe-C phase diagram [98].

The microstructure of this region depends on the wt.% of carbon and alloying elements, grain size and the cooling rate. With low carbon steel substrates, the structure in the grain growth region is pro-eutectoid ferrite at the grain boundaries of the prior austenite, while the grains themselves are usually ferrite with pearlite, or ferrite with bainite. With the increase of the cooling rate or the content of carbon and alloying elements, the ferrite grains disappear. The austenite grains then transform into upper or lower bainite, martensite or a mixture of these microstructures. The resulting grain size depends on the size of the austenite grains. If the austenitic grains are large, the resulting structure will be coarse [99]. In general, the metal in this region loses some of its ductility. Figure (2.5) shows the structure of this zone.

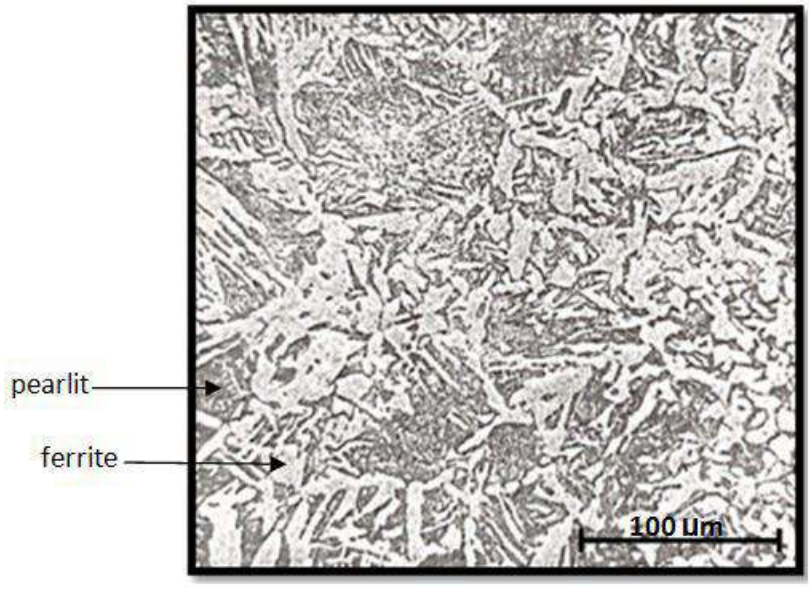

Figure (2.5): Grain growth region of a low carbon steel weld [30].

B. Grain Refined Region: it is the region adjoining to that of grain growth, at which the metal is heated to a temperature directly above the A3. The metal of this zone completely transforms into a new, fine-grained austenitic structure, in which the heating time is not long enough for the growth of the austenite grains. Therefore, moderate cooling will form fine pearlitic grains. This is identical to the *normalizing* heat treatment applied

in carbon steels, which includes heating to A3 and then cooling with still air [100]. This region has relatively high strength and toughness, the same features and properties of normalized steels. Figure (2.6) shows the structure of this region, where dark areas indicate pearlite and light areas indicate ferrite.

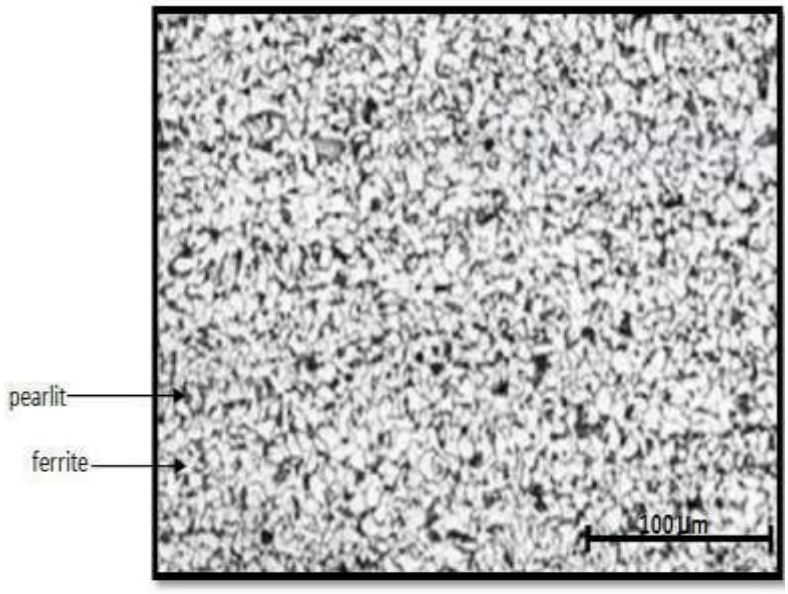

Figure (2.6): Grain refined region a low carbon steel weld [30].

C. Transition Region: this region is exposed to temperatures between A3 and A1 (Figure 2.4). This heating transforms pearlite grains (at least partially) into fine austenite grains, but is not sufficient to transform ferrite grains. A partial allotropic recrystallization takes place in this region. Upon cooling, the fine austenite grains transform into fine pearlite. Obviously, in this case, the pearlite grains are reduced while the ferrite grains remain the same [30]. Figure (2.7) shows the microstructure of this region.

For alloy steels, this region has special significance, as the same cooling rate might be enough to transform the fine grains of austenite to martensite, resulting in high hardness and brittleness in this region. This might expose these kinds of steels to hydrogen cracks. It should be noted that the main reason for the formation of martensite in this region is carbon, as with the increase in the proportion of carbon and other alloying elements, the hardenability of steels increases.

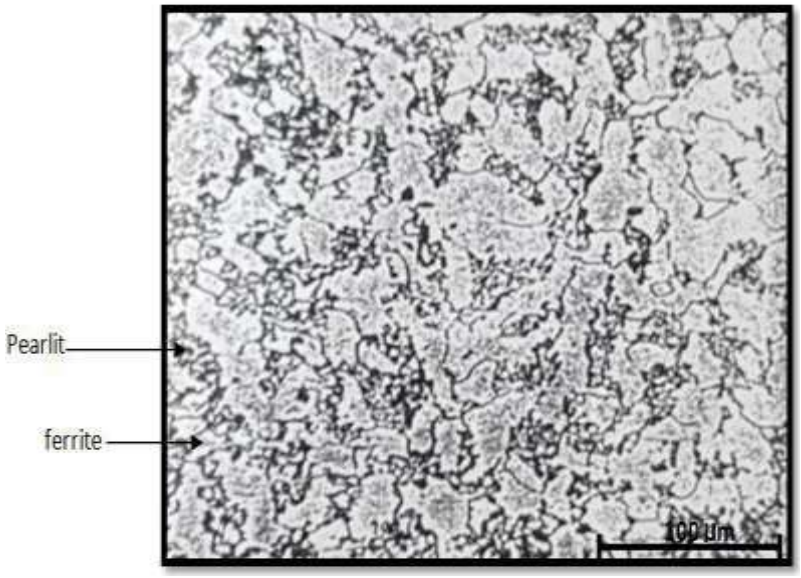

Figure (2.7): Transition region a low carbon steel weld [30].

2.8 Literature Review

The literature review provides detailed information on studies that explore the influence of tungsten carbide-nickel composite coatings on the surface properties of steel substrates, in addition to mass fraction of tungsten carbides and heat input on these properties.

In 2003, Huang et al. [53] investigated WC-Ni composite clad layers created with various wt.% of WC (10, 30, 50 and 70) on AISI H13 tool steel substrates using a pulsed Nd:YAG laser and optical fibers. The effects of volume fraction of the WC reinforcement particles, as well as laser pulse energy, beam profile and travel speed on clad layer development and characteristics were investigated. The findings showed that relatively fully dense, thick (> 0.5mm) and crack-free WC-Ni clad layers can be deposited on the substrates without any preheating. The findings also demonstrated that the volume fraction of the WC particles is the most important factor influencing on most properties of the clad layers, such as micro-hardness, wear resistance and porosity. The higher the volume fraction of reinforcement WC particles, the higher the micro-hardness and wear resistance, and the lower the porosity of the clad layer. Micro-hardness of the matrix was on average as high as 800HV.

Zhong et al. (2004) [101] studied the WC-Ni hard layer created by laser cladding associated with coaxial feeding of a W/C/Ni powder mixture with different wt.% (W: 51-90, C:1.25-5.0 balanced by Ni) on an AISI A29/A29M steel cylinder of 20×100mm. A crack-free WC-Ni coating was obtained. The deposited WC particles have a rectangular or quadrangle cross section with a size of 2~30μm. The deposited layer showed rotary, step and cross growth morphologies of the WC formation. In addition to the WC, the clad layer had phases such as W_2C, W_3O, FeW_3C, CW_3, Fe_6W_6C, W, C, (Fe, Ni).

Acker et al. (2005) [45] discussed the effect of particle size and distribution of WC/W_2C carbides on the wear resistance of nickel-based composite coatings deposited with an average thickness of about 800μm by CO_2 laser cladding on low carbon steel substrates. Different layers were created using three various carbide particle sizes with volume fractions ranging from 0% up to 50%. Three various wear modes were evaluated. Tests of ball-on-disc with an Al_2O_3 ball were performed at first. The test of ball cratering with a 4μm SiC abrasive was used to evaluate mild wear. Finally, the test of pin-on-disc was also used to determine the resistance to severe two-body abrasion. The wear resistance of the coating layers with the finest WC/W_2C carbides was found to be highly dependent on the carbide concentration. However, the amount of the wear reduction was significantly dependent on the mode of wear. A small quantity of carbides was sufficient to greatly increase the wear resistance in the two-body abrasion and sliding wear. Microstructure and hardness, in addition to internal stress of the coatings were also evaluated.

Wan et al. (2007) [102] studied the laser coating-texturing (LCT) process on AISI A29/A29M bearing steel substrates with WC-Ni alloy powder using laser pulses at extremely high repetition rates to create a myriad of

micro-craters of the desired shape on the substrate surfaces. Besides, surface alloying of these dimples was applied by melting nanoparticles of the WC-10%Ni alloy powder mixture on the substrates. The pre-coating alloying powder thickness was about 80μm. Results revealed good bonding for the texturing layers with the substrates, and that the texturing layers mainly had a dense, hard and fine-grained structure. The wear resistance of the coating surface was five times greater than the substrates. The average Micro-hardness value of the surface was up to 850HV.

Paul et al. in 2013 [103] studied air-jet erosion behavior of WC-Ni laser clad coatings deposited on AISI 316L austenitic stainless steel (75mm dia. and 12mm thickness) substrates with various wt.% of WC (5, 10 and 15) in potential power plant applications. The results revealed an excellent metallurgical bond between the WC-Ni coatings and the substrates. In the laser clad layers, no dissociation, partial melting or full melting of the WC particles was observed. Micro-hardness of the cladding layer was 900–2400 HV, while for the substrate was 230–270HV. The air-jet erosion resistance of the WC-Ni clad layer was revealed to be four times (at least) that of the nickel clad layer without WC reinforcing particles.

Tosun (2014) [66] investigated the effects of current value (100, 120 and 140A) and thickness (1 and 2mm) of the pre-placed WC-95%Ni mixed powder layer on the microstructure and hardness of the alloyed coatings deposited on an AISI 1010 plain low carbon steel substrate using the TIG cladding technique. The findings exhibited good metallurgical bonding between the coating layers and the substrate. The results also showed a heterogeneous WC particles distribution with clear bonding between the particles and the matrix without cracking. Some fairly coarse WC particles could not melt entirely and remain in the clad coating, particularly at the bottom and sides where the temperature was lower than that at the middle.

Microscopy of the deposited coating surfaces, depending on the cladding conditions, showed different microstructures such as WF, AF, grain boundary ferrite, bainite and a slight amount of martensite. When current values increased, the micro-hardness of the composite coatings increased.

Zhang et al. (2016) [73] studied the WC-Ni composite clad layers created on an AISI 316L stainless steel substrate using laser cladding. The results revealed that the incompletely dissolved WC particles were distributed uniformly throughout the clad coating, and were inserted in the eutectic structural matrix. The coating wear was mostly characterized via plough wear besides oxidation wear, but it is also accompanied by abrasive wear, according to dry sliding wear tests. In comparison to the substrate, the composite coating has significantly improved wear resistance and hardness. The results also demonstrated that the WC particles distribution in laser composite coatings could mainly affect the wear rate of the coatings under harsh environments.

In 2016, Shu et al. [54] investigated Ni-based composite coating with WC-reinforcement particles deposited by laser cladding on the mild steel substrate. Graphite and tungsten powders were mixed to form a 1:1 molar ratio, which then mixed with Ni powder in terms of mass ratios 3:7, 1:1, and 7:3. The pre-placed powder thickness was 1.5mm. The results showed planar grains at the interface, as well as some moderately large columnar dendrites on the coating sides near the substrate. The WC particles were distributed homogenously throughout the layer, with no cracks or pores. The maximum micro-hardness value of the coating reached to a 755HV. The deposited WC particles mostly showed a unique triangular prism-like shape. It was deduced that the crystal structure and the interface energy played an important role in controlling the shape of the WC that developed from a sphere to a hexagonal prism and then to a triangular prism.

Sabzi et al. in 2018 [67] evaluated the influence of volume fraction of W_2C nanoparticles (0, 5, 10, 15 and 20 wt.%) on properties of the Ni-W_2C nanocomposite coating deposited with a thickness of (3-4mm) on DIN St37 plain carbon steel substrate using TIG cladding technique with a current of 150A. Microscopy exhibited that the deposited Ni-W_2C coatings had dendritic microstructures with a uniform distribution of W_2C nanoparticles. The findings also showed that by increasing the volume fraction of W_2C nanoparticles, the size of the dendrites decreased, with a sharp increase in hardness and wear resistance. In addition, the wear mechanism changed from complicated abrasive-sheet like to complicated adhesive oxidation.

2.8.1 Summary

The recently reviewed literature mostly relevant to the current study is summarized in Table (2.1).

Table (2.1): Summary of the reviewed literature mostly related to the present study.

I	Researchers	Year	Cladding Type	Substrate	MMC (wt.)	Major Results
1	Huang et al.	2003	laser	AISI H13 tool steel	(10, 30, 50, 70%) WC/Ni	The clad layer's average micro-hardness values were as high as 800HV, with higher wear resistance.
2	Wan et al.	2007	laser	AISI A29M bearing steel	90%WC/ Ni	Wear resistance of the coating surface was 5 times higher than that of the substrate with an average micro-hardness values up to 850HV.
3	Tosun	2014	TIG	AISI 1010 plain low carbon steel	5%WC/ Ni	The micro-hardness of the composite coating increased as the amount of WC particles in the composite coating increased.
4	Sabzi et al.	2018	TIG	DIN St37 plain carbon steel	(0, 5, 10, 15, 20%) W2C/Ni	The deposited coatings had a hardness range of 300 to 1000HV. Wear resistance increased with increasing the amount of tungsten carbide.

After reviewing the previous literature, it was clearly noted that most studies and researches were dealing with the use of the laser cladding technique, but few researchers have dealt with the usage of TIG cladding technique. The TIG technique was chosen in the present study because it is suitable for a wide range of materials, easy to transport and widely available. It also has low equipment cost, low dilution ratio and high deposition rate. In addition, manual and automated operations can be employed. To the knowledge of the author of the current study, the former literature was confined to limited wt.% of tungsten carbide (up to 20%). In addition, there has been no comprehensive study involving the usage of a wide range of wt.% of tungsten carbide and its effects on the properties of WC-Ni composite coatings deposited using the TIG cladding technique. Furthermore, the TIG technique has not previously been used to deposit the clad composite layers on low alloy steel substrates, but has been confined to plain carbon steels. In addition to the gap in the previous literature mentioned above, the present study deals with investigating the influence of energy input by controlling current values on the performance of TIG clad WC-Ni composite coatings.

CHAPTER THREE:

EXPERIMENTAL PART

CHAPTER THREE: EXPERIMENTAL PART

3.1 Introduction

This chapter presents a general description of the experimental work procedures, and describes all the conditions under which the tests have been conducted. It involves materials, equipment, and experimental techniques used in this study including the deposition of coating layers on low alloy steel substrates using the TIG cladding technique, in addition to preparing specimens for tests (cutting, milling, grinding...). The mechanical properties of the clad layers were examined by micro-hardness and wear tests. In addition to macrography, the changes in microstructure were also evaluated by the optical microscope (OM), scanning electron microscope (SEM) and energy dispersive spectrometer (EDS). Moreover, the particle size of powders and chemical composition of the materials used in this study were analyzed. Figure (3.1) shows the general program plan utilized in this study.

3.2 Materials and their Specifications

3.2.1 The Substrate used in this Study

The chemical composition of the low alloy steel plates used in this study as substrates according to the American Iron and Steel Institute (AISI) [104] is shown in Table (3.1). The cross section of the plate is (9*70) mm, knowing that the raw material is annealed. The pieces (substrates) to be coated were prepared from the raw material with a length of (100mm) for each piece. The chemical composition analysis for the raw material was carried out using Spectro Max Metal Analyzer at the State Company for Engineering Rehabilitation and Testing–Baghdad. Table (3.1) shows the chemical composition (with an average of three readings) of the raw material used as a substrate. It falls within the range of the chemical composition according to AISI (nominal).

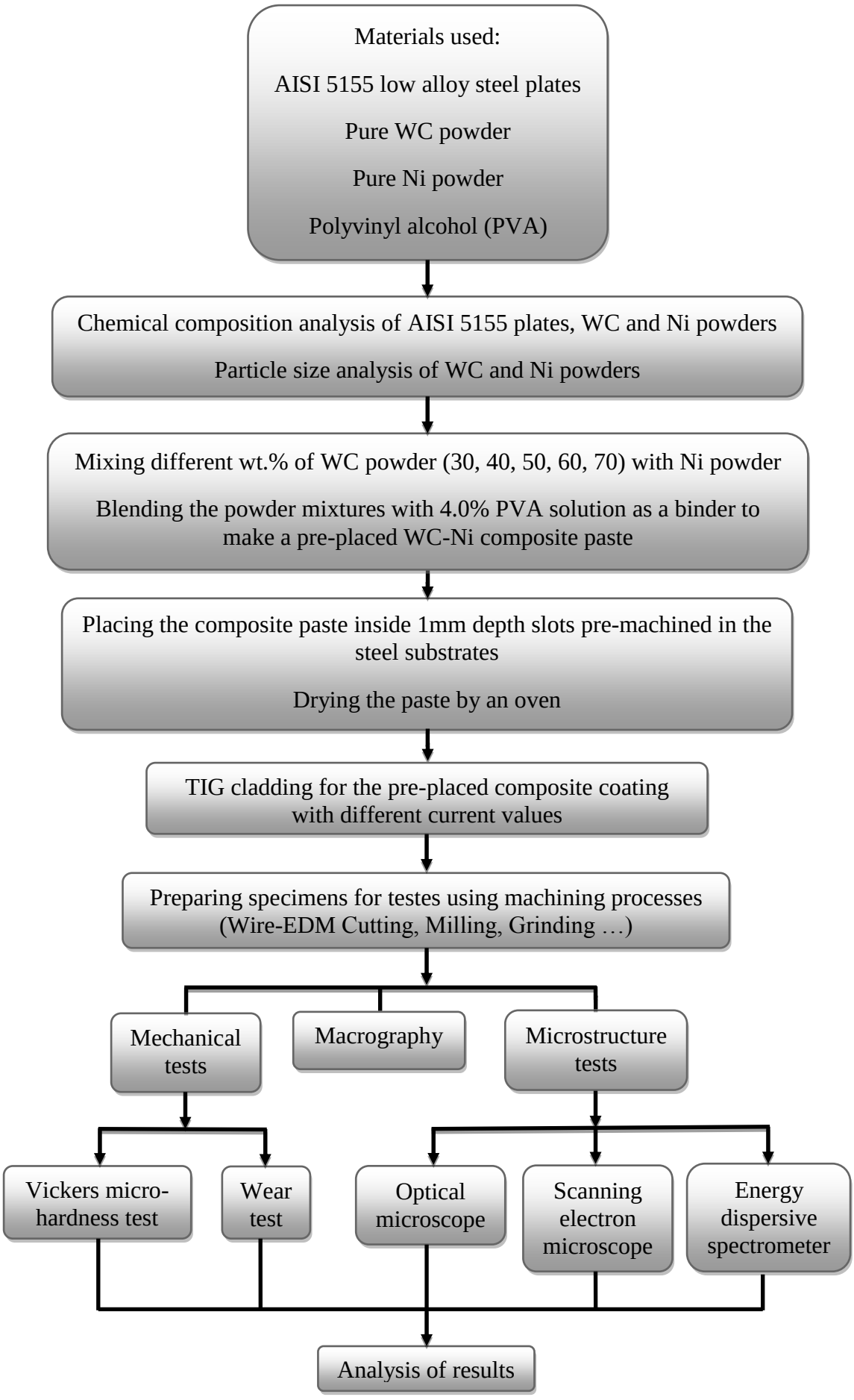

Figure (3.1): Flowchart of the current work.

Table (3.1): Nominal and actual chemical composition of the substrate material.

Alloy		Chemical composition (wt. %)						Spec. symbol (AISI)
		C	Mn	Si	Cr	P	S	
Low alloy steel	Nominal	0.51-0.59	0.7-0.9	0.15-0.3	0.7-0.9	0.04 max.	0.04 max.	5155
	Actual	0.533	0.764	0.258	0.863	0.0119	0.0069	

3.2.2 Cladding Materials

3.2.2.1 Pure Nickel Powder

Table (3.2) shows the specifications of pure Ni powder, according to Oerlikon Metco LTD. Chobham, Woking, England. The particle size of Ni powder was analyzed using a Bettersize 2000 laser particle size analyzer located in the laboratories of Ceramic Engineering and Building Materials Department/Faculty of Materials Engineering/University of Babylon. The particle size was (3-23μm). The chemical composition analysis performed at the Ministry of Sciences and Technology-Baghdad revealed that the purity of Ni powder was > 98.59 wt.%..

Table (3.2): Nickel powder specifications.

Product	Chemical composition (wt.%) min.	Nominal particle size distribution (μm)	Manufacturing method
Metco 56C-NS	99.3	-75 +45	Precipitated

3.2.2.2 Tungsten Carbide Powder

The purity of WC powder used in this study was 99.8% according to Changsha Santech Materials Co. LTD. China. The particle size of WC powder was analyzed using a Bettersize 2000 laser particle size analyzer located in the laboratories of Ceramic Engineering and Building Materials Department/Faculty of Materials Engineering/University of Babylon. The

particle size was (3.5-5μm). The chemical composition analysis of WC powder carried out at the Ministry of Sciences and Technology-Baghdad revealed that the amount of tungsten element was > 97.19 wt.%.

3.2.3 Binding Material

Polyvinyl Alcohol (PVA) was used as a binder material to make a pre-placed WC-Ni composite paste. Table (3.3) shows the specifications of PVA, according to ME Scientific Engineering Ltd. product of Germany, packed in the UK.

Table (3.3): Polyvinyl Alcohol specifications.

Product	PVA code	Molecular formula	Viscosity
MESE	8-88	$(C_4H_6O_2.C_2H_4O)x$	8 mPa.s (in 4% aqu. Solution)

3.3 Procedures before the Cladding Process

The following procedures have been carefully carried out before the start of the cladding process:

1. Removing rust from the substrate surfaces using a surface grinding machine by (0.5mm) from each surface, and then cleaning the surfaces from oils, grease and the residues of chips and other impurities.
2. Eight slots with dimensions of (1x6x30mm) were made in the substrates (Figure 3.2a) using a universal milling machine, inside which the pre-placed WC-Ni composite coatings were deposited.
3. To prepare the binder, 4.0% of PVA was dissolved in 96% of hot distilled water (50°C) for (15min.) using a magnetic stirrer located in the laboratories of the Metallurgical Engineering Department/Faculty of Materials Engineering/University of Babylon.

4. Different wt.% of WC powder (30, 40, 50, 60 and 70) and Ni powder were weighed using a sensitive balance in the laboratories of the Metallurgical Engineering Department to be then mixed as WC-Ni mixtures.
5. To keep the powder mixtures under the flow of Ar gas during TIG cladding, these mixtures were blended with a 4.0% PVA solution binder to form a pre-placed WC-Ni composite paste to be subsequently deposited in the slots (Figure 3.2b).
6. Drying the paste by an oven at 100°C for an hour.

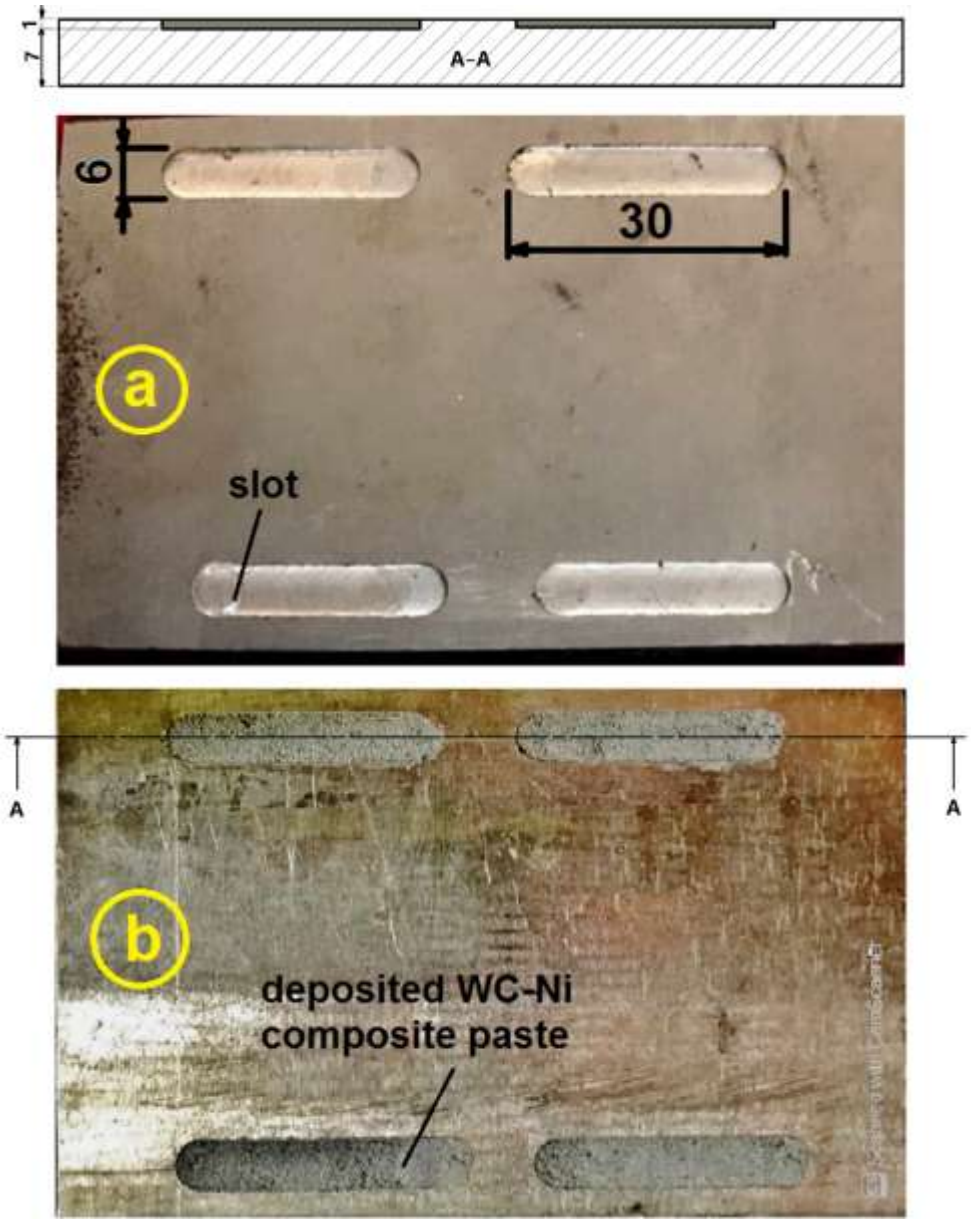

Figure (3.2): (a)-dimensions of slots machined in the substrates in mm (b)-WC-Ni composite paste deposited in the slots.

3.4 Tungsten Inert Gas Cladding of Tungsten Carbide-Nickel Composite Coating on Low Alloy Steel Substrate

The cladding process was carried out using a TIG welding machine combined with a lathe machine to make the tungsten arc travels along the composite layers at automatic and constant speeds. The arc ignition and extinguishing were on the substrate for each coating layer (Figure 3.3). Table (3.4) shows the TIG cladding parameters based on the trial and error method and previous literature.

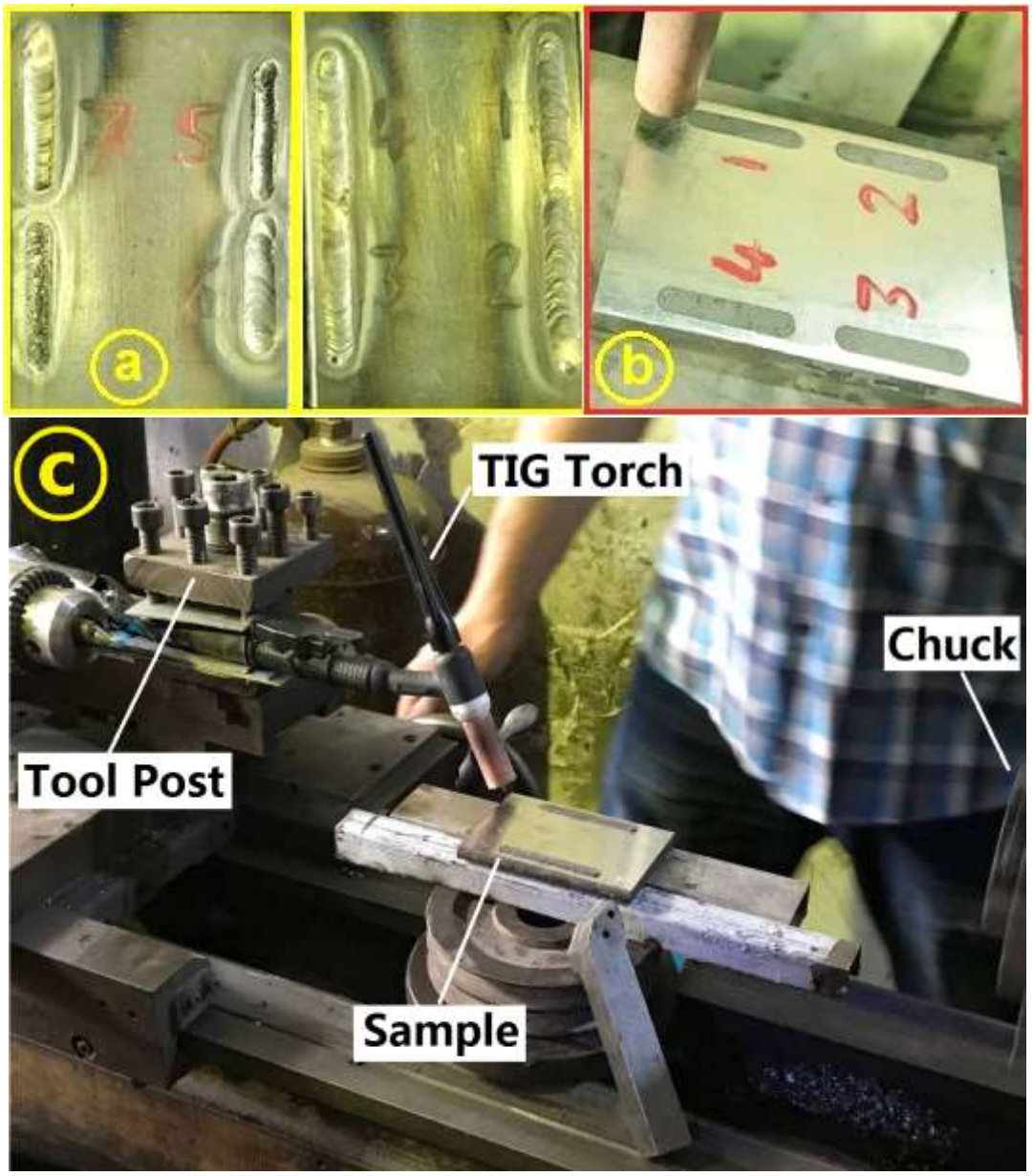

Figure (3.3): (a) - samples before preparing test specimens (b) - samples under cladding (c) - the TIG torch combined with a lathe machine.

Table (3.4): TIG cladding parameters of low alloy steel substrates.

Cladding by the use of	**Pure WC powder of (wt.%)**							
	30	**40**	**50**	**60**	**70**	**70**		
Clad symbol	C1	C2	C3	C4	C5	C6	C7	C8
Current value (A)	120					130	140	80
Travel speed (mm/min.)	69							
Voltage value (V)	15							
Position	Flat							
Polarity	DCEN							
Thickness of layer (mm)	1							
Ar gas flow rate (l/min)	10							
Ar gas purity (%)	99.999							
Arc length (mm)	3							
Tungsten electrode diameter (mm)	2.4							
Tungsten electrode type	Thoriated Tungsten ESAB-WT20							

3.5 Preparing Test Specimens

After cladding the low alloy steel substrates, specimens were cut from the resulting samples (Figure 3.3a) using Wire-EDM for micro-hardness, macro-micrography and wear resistance tests.

3.6 Macro/Micrography

- **Optical Macro/Microscopic Examination**

Specimens for macro-microstructural analysis were prepared based on the standard metallographic techniques (according to ASTM E3-2017 and ASTM E 407-2015) which include the following steps:

1. Specimens should be cut to an appropriate size to facilitate handling and to detect the microstructure variations in different zones.

2. The wet grinding process was carried out by exposing the specimen surface to a rotary disc using sandpapers of (SiC) with different grades sequentially (180, 220, 320, 400, 600, 800, 1000, 1200 and 1500 grid size). The specimen was then washed with water and dried with hot air.

3. Mechanical Polishing: Diamond particle pastes were used to remove the new finer scratches introduced by the grinding step. Polishing was achieved with 3, 1 and 0.25μm pastes sequentially; the polishing was applied on special clothes fixed on electrically powered rotary disc.

4. Etching: Nital 2% (as an etchant for the substrate) and $HCl+H_2O_2$ (as an etchant for the clad layers) were used to reveal the phases by their chemical effects on the different phases with various levels. Following the etching, the prepared surface was cleaned with ethanol.

An optical microscope was then used to realize the microstructure and topography of different regions on the prepared specimen surfaces through the cross section of the clad layers. It was also used to observe and determine the type, size and location of potential surface defects across the clad layers. This inspection was carried out at the labs of Al-Razi Metallurgical Research Center-Tehran/Iran based on ASTM E883-2017.

- **Scanning Electron Microscope**

Microstructural examination and chemical composition analysis were performed using SEM and EDS at the labs of Al-Razi Metallurgical Research Center-Tehran/Iran. SEM images were taken for all prepared specimens in order to clearly investigate the microstructure with higher accuracy. The specimens were prepared with suitable grinding papers, polished and then etched with the same steps as optical microscopy. The EDS examination was performed in order to obtain the elemental analysis of the constituents of the deposited coating layers.

3.7 Mechanical Tests

- **Micro-hardness test**

Micro-hardness test was performed using digital Vickers micro-hardness tester type (HVS-1000) according to ASTM E92–17. Measurements were done for the deposited coating layers and the substrate after grinding and polishing the surfaces being measured. The test was conducted with a load of 500g for 10s with two measurements per point. This test was performed in the labs of the Metallurgical Engineering Department-Faculty of Materials Engineering-University of Babylon.

- **Wear Test**

For the wear test, a pin with 3×3 mm^2 cross section was cut from each coated specimen by the Wire-EDM to be used with the pin on the disk method. The wear resistance of the deposited cladding layers was measured based on weight loss at different sliding distances. The amount of wear depends on the applied force, sliding distance, speed and environmental conditions of the test procedure shown in Table (3.5). Subsequently, the specimens were weighed using a digital sensitive balance with 0.0001g accuracy. This test was done at the labs of Al-Razi Metallurgical Research Center-Tehran/Iran according to ASTM G 99 (2017).

Table (3.5): The wear test parameters used in this study.

Applied load (Kgf)	Linear speed (m/min)	Wear Sliding distance (m)	Test temp. (°C)	Test moisture (%)	Abrasive disc hardness (HV)
4.00	10	3000	23	50	>2060

CHAPTER FOUR:

RESULTS & DISCUSSION

CHAPTER FOUR: RESULTS and DISCUSSION

4.1 Introduction

In this chapter, the results of the experimental work were presented and discussed. Macrography and microanalysis of MMC coatings deposited on low alloy steel substrates have been evaluated by the OM, SEM with the assistance of the EDS. Results of mechanical tests (Vickers micro-hardness and wear resistance) for these coatings were also discussed.

4.2 Macrography

Macroscopic examination was carried out on eight specimens of low alloy steel substrates coated with WC-Ni composite by the TIG cladding technique using different wt.% of WC (30, 40, 50, 60 and 70) and various current values (80, 120, 130 and 140A). Figures (4.1 and 4.2) show a variety of defects or flaws such as porosity, cavities and cracks within the MMC clad layers.

It is well known that the clad layers generally suffer from severe thermal mismatch with the substrate, resulting in high cooling rates, which act as a main contributing factor to the occurrence of these defects [53,72]. Most of these defects appeared on both sides of the clad layers. This could be attributed to the fact that the cooling rates at the clad layer sides are higher. Another reason for the cavities at the clad sides is the lack of fusion in these regions because the heat is typically concentrated at the center of the clad layers rather than the sides. Poor fusion clearly appeared in the C8 clad due to the insufficient current value (80A) used with this clad.

Although the defective regions are small compared to the overall cross sections of the clad layers, the defects shown in the figures are considered as inherent flaws in the MMC coatings [107].

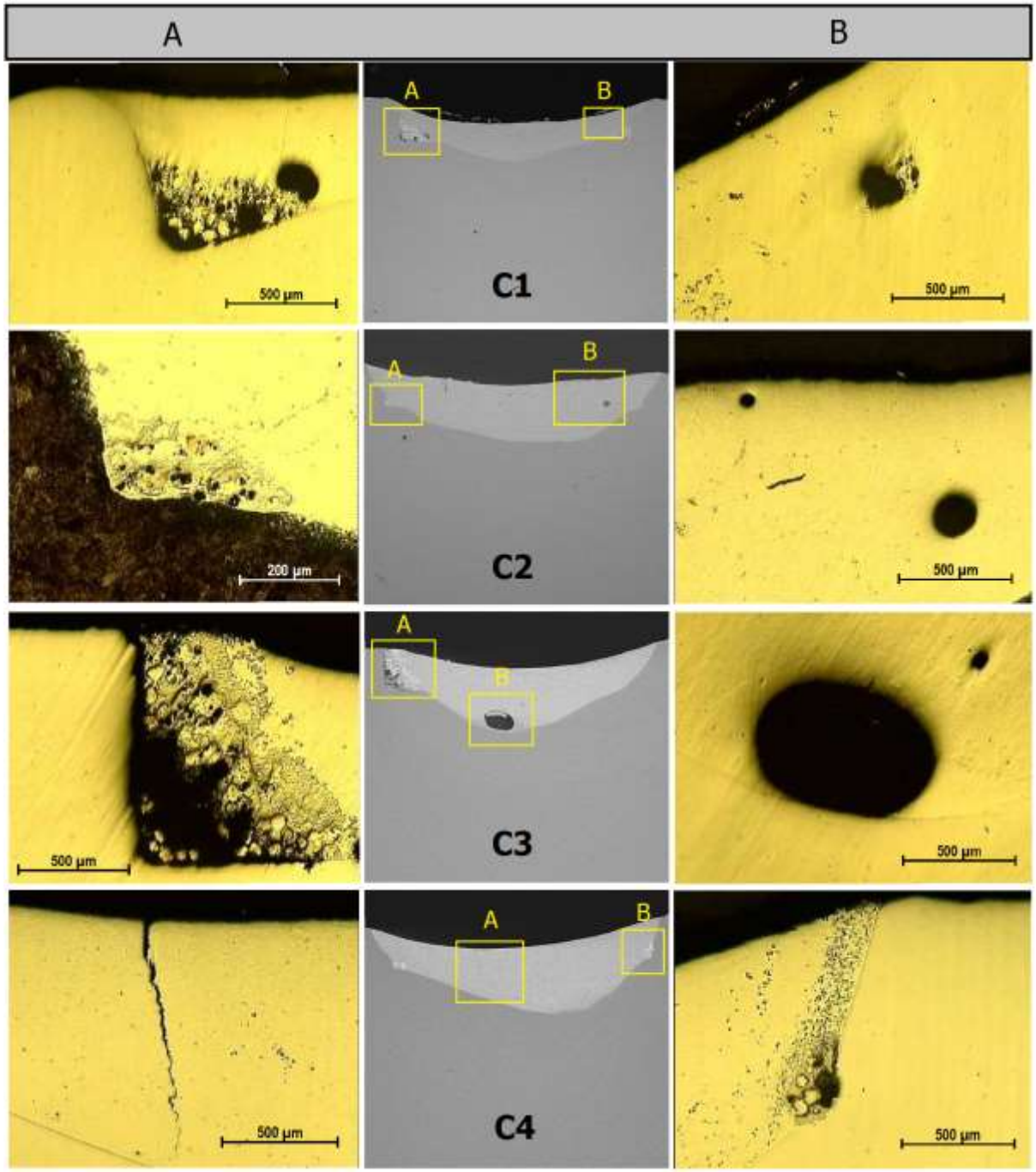

Figure (4.1): Macrography of the clad samples resulting from mixing different wt.% of WC powder (C1:30, C2:40, C3:50 and C4:60) with Ni powder using a current of 120A.

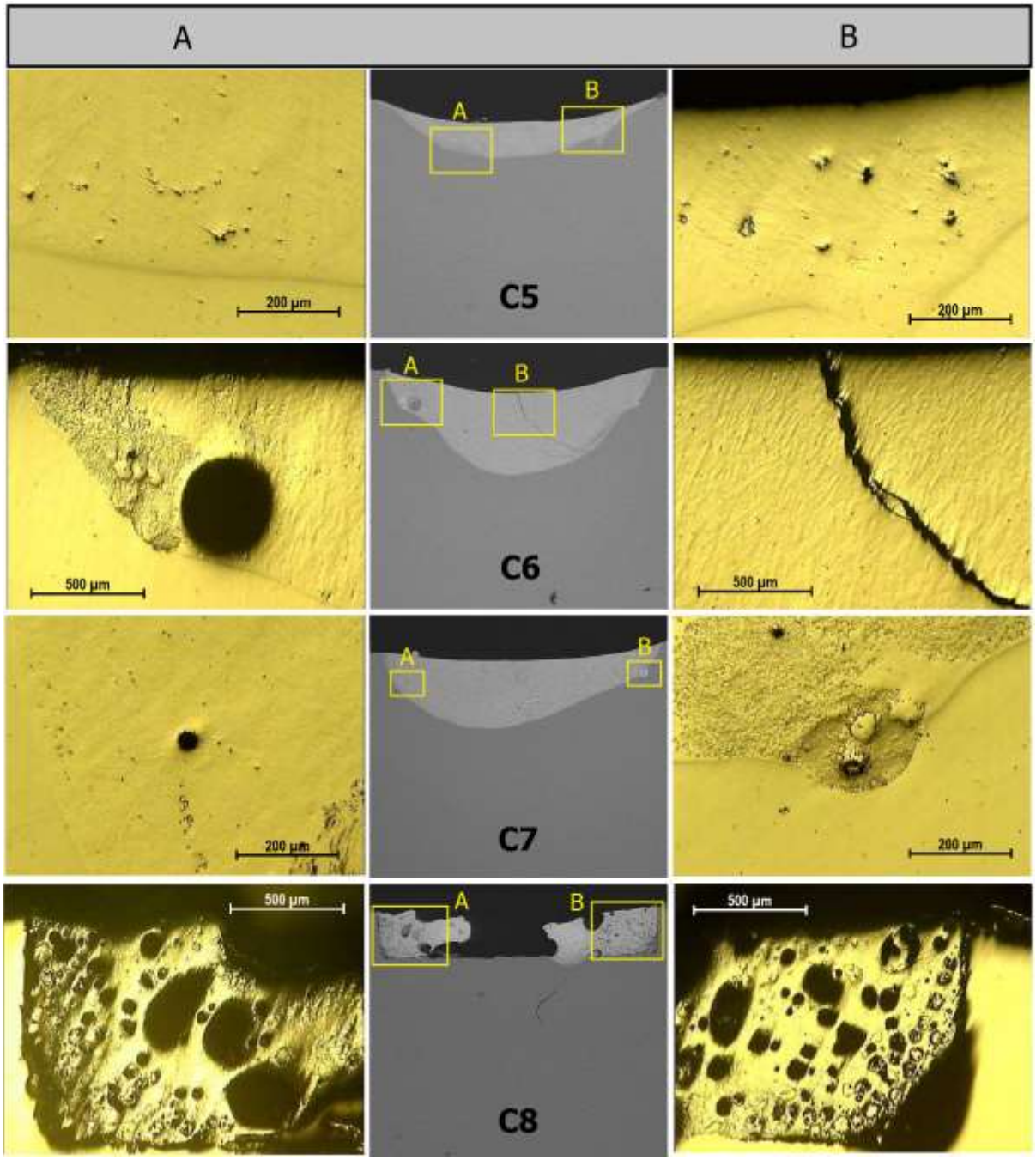

Figure (4.2): Macrography of the clad samples resulting from mixing 70wt.% of WC powder with Ni powder using different current values (C5:120A, C6:130A, C7:140A and C8:80A).

Porosity was observed in most of the clad samples despite the efficient inert gas protection used (Table 3.4). However, all clad samples except C8 exhibited relatively suitable interfacial bonding with the substrate.

Several studies [67,107,108,109,110,111] dealt with the use of preheating as an effective method to overcome the defects via reducing the cooling

rate. Lower cooling rates provide a sufficient time for gas bubbles to escape from the molten pool into the atmosphere before solidification of the clad layers, thus reducing the porosity [112]. Preheating also reduces extreme thermal gradients, thereby reducing the high thermal stresses that promote cracking [107,108,109,110,111]. Moreover, preheating has a significant role in reducing cavities [67].

Other studies have addressed the reduction of these defects by using multilayer deposition [113], and adding certain elements to the clad layers [53,110]. Multilayer deposition increases the heat input of the component, which in turn decreases the cooling rate, thus avoiding defects [113]. The addition of lanthanum (La) and aluminum (Al) could effectively eliminate porosity in the MMCs under an action of deoxidizing and refining [53,110]. La can easily react in the molten pool with oxygen, nitrogen, silicon and other detrimental elements such as sulfur [114,115]. In addition, the surface tension of La atom is relatively lower than that of Ni, which leads to improved wettability and flowability of the Ni matrix [116]. Al has also an affinity for oxygen much higher than that of carbon, which minimizes the formation of carbon dioxide and thus reduces the pores in the WC-Ni composite clad layers [53].

4.3 Micrography

Before discussing the microstructural variations across the coated samples, it is necessary to get acquainted with the microstructure of the substrate material prepared from low alloy steels having the chemical composition shown in Table (3.1). SEM showed in Figure (4.3) that the microstructure of the substrate alloy was mostly pearlite, mainly composed of sequential lamellar layers of ferrite and cementite, with a small amount of ferrite. This is the typical structure of an alloy that has such a chemical composition in the annealed condition.

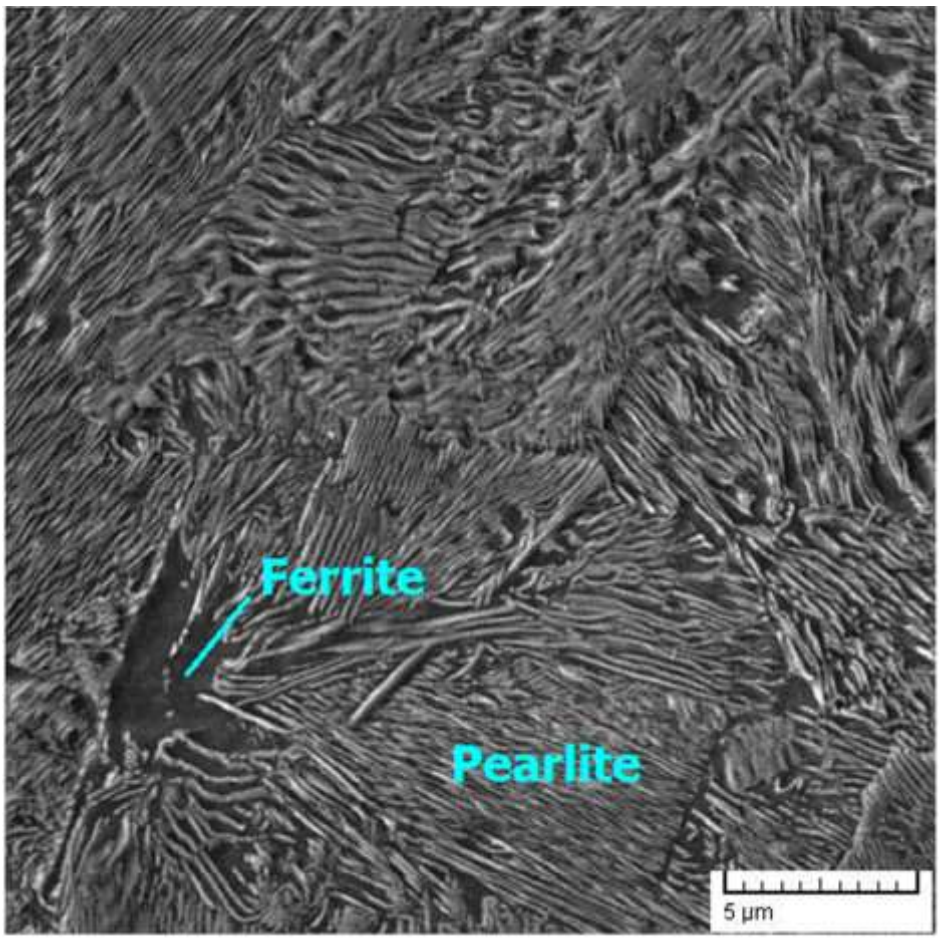

Figure (4.3): Microstructure of the substrate material using an SEM.

Microscopic examination of each sample showed variations in the microstructures of the clad layer and adjacent regions of the substrate. These variations are attributed to the differences in chemical compositions of the coating layers and the large thermal gradients to which the sample is exposed from the melting temperature to that of the substrate unaffected by heat. This is typically followed by a rapid cooling rate caused mainly by the relatively cold substrate and the atmosphere.

Figure (4.4) shows microstructures of the C1 sample coated with 30% WC-Ni composite by the TIG cladding technique using a current value of 120A. Micrography was performed for zones at different depths (four zones) along the centerline of the cross section of the clad layer.

Figure (4.4) exhibits that the optical microstructure of Zone 1 (near the clad surface) consists of nickel solid solution grains with WC particles distributed through the matrix. Figure (4.5) shows the microstructure of this zone with higher magnifications, where an acicular WC within the matrix was. The density of the acicular carbide significantly increased in Zone 2, where a bow-like shape of the acicular carbide formed near the clad surface, in addition to a small part of it formed at the clad-substrate interface. Figure (4.6) shows the microstructure of Zone 2 with higher magnifications.

The microscopy of Zone 3 revealed a mixture of aquiaxid and columnar grains of nickel solid solution with WC particles distributed through the matrix. The columnar grains are directed perpendicular to the cooling surface (clad-substrate interface) towards the clad surface. This is because heat typically flows from the molten pool towards the adjacent colder substrate metal. Figure (4.7) presents the microstructure of Zone 3 at higher magnifications.

The optical microscopy of Zone 4 exhibited in Figure (4.4) the microstructure of the bottom portion of the clad layer, substrate and the interface between them. It is clearly observed presence of tiny grains at the clad-substrate interface similar to the chilled crystals formed in the mould castings, in addition to a mixture of aquiaxid and columnar grains with WC particles distributed through the matrix. Figure (4.8) shows the microstructure of Zone 4 with higher magnifications, where the dilution between the clad layer and the substrate material is very clear. This indicates a good bonding between them, which can be easily introduced by the TIG cladding technique [33].

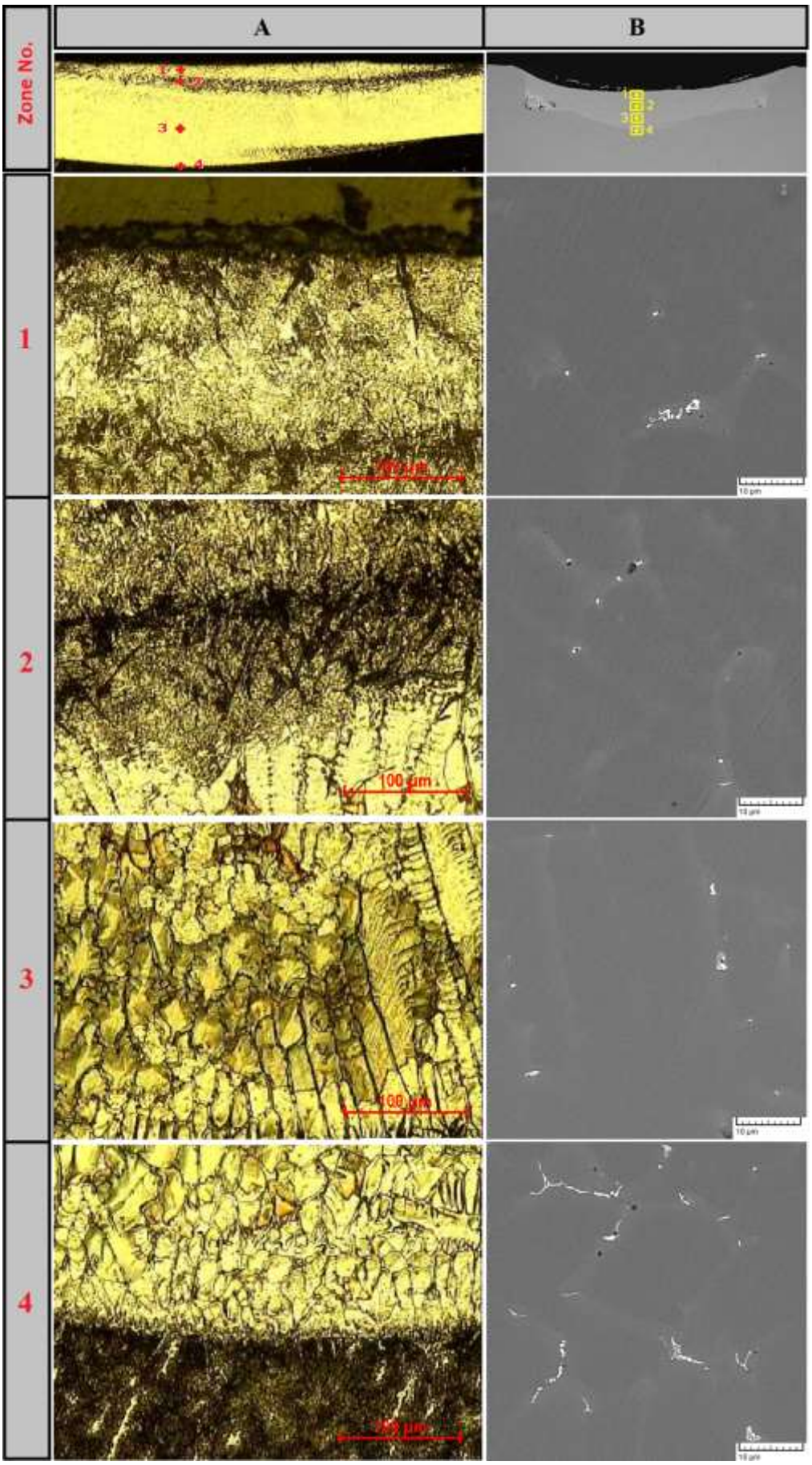

Figure (4.4): Microstructural map of the C1 sample at different depths along the centerline of the cross section of the clad layer using an (A): OM and (B): SEM.

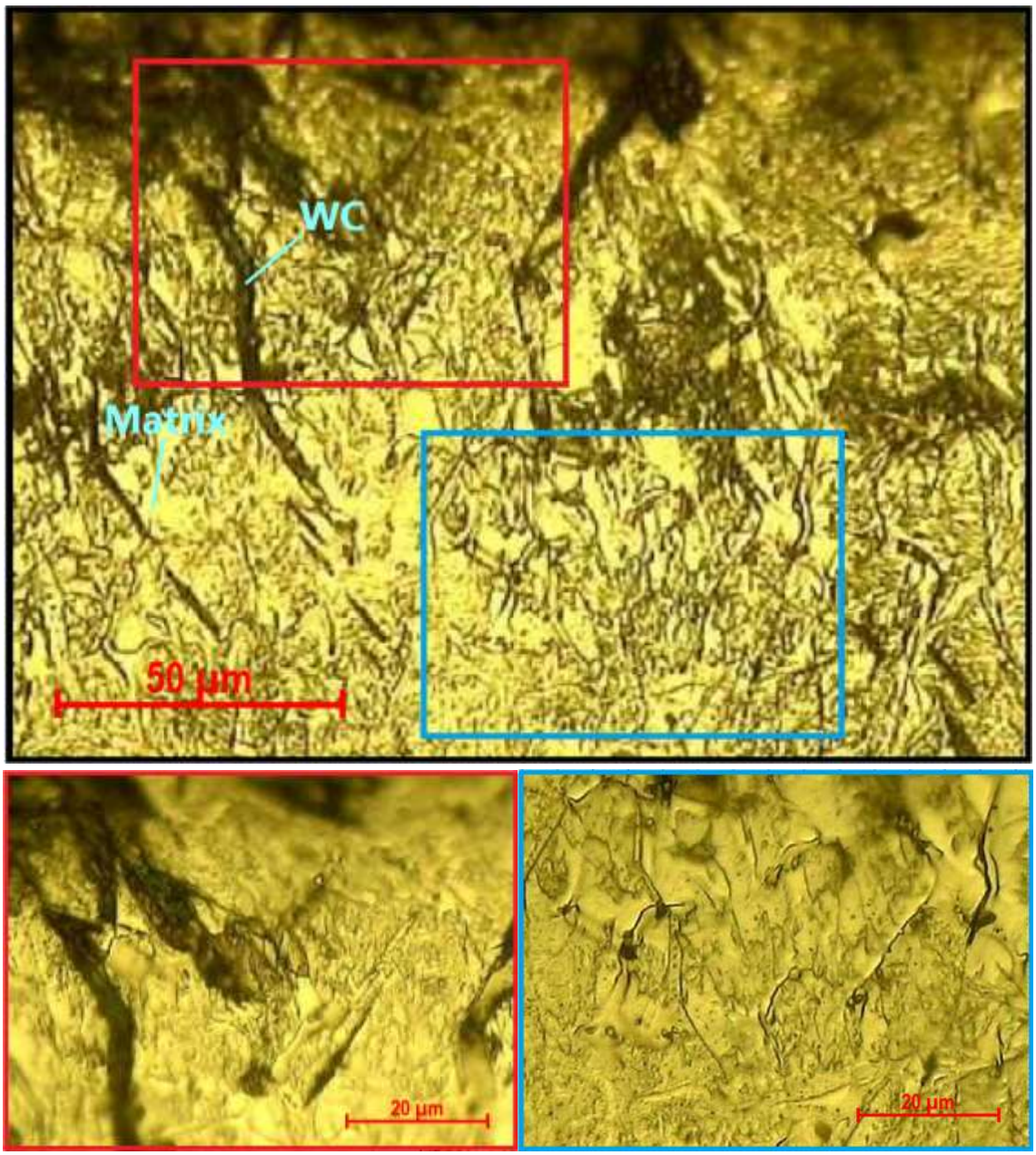

Figure (4.5): Optical microstructure of Zone 1 with higher magnifications.

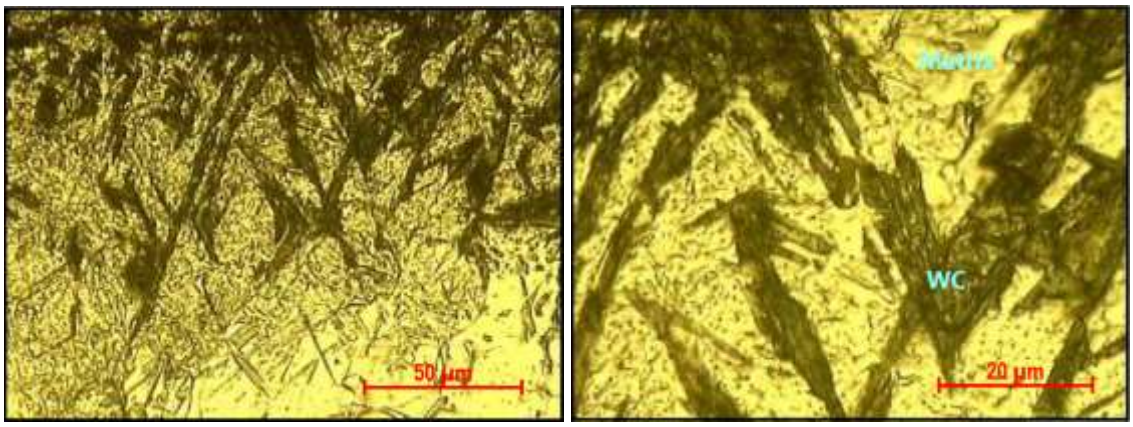

Figure (4.6): Optical microstructure of Zone 2 with higher magnifications.

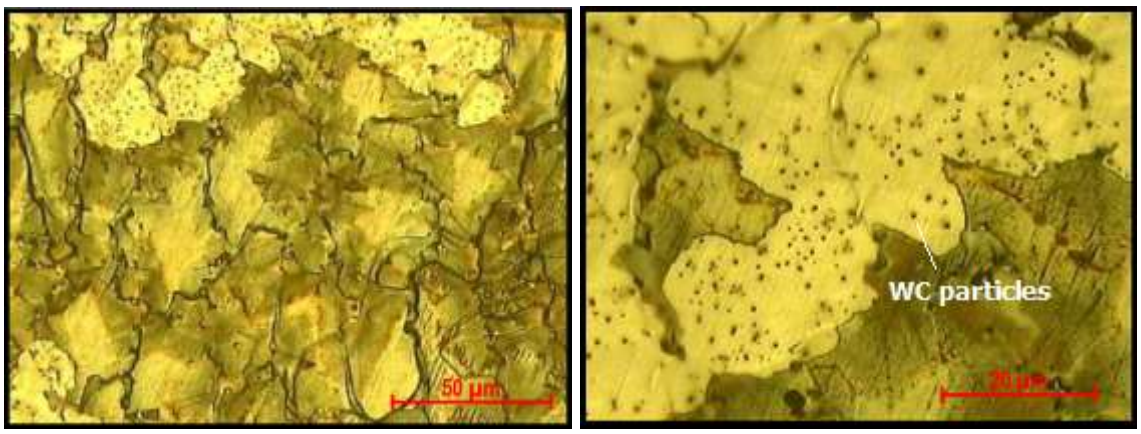

Figure (4.7): Optical microstructure of Zone 3 at higher magnifications.

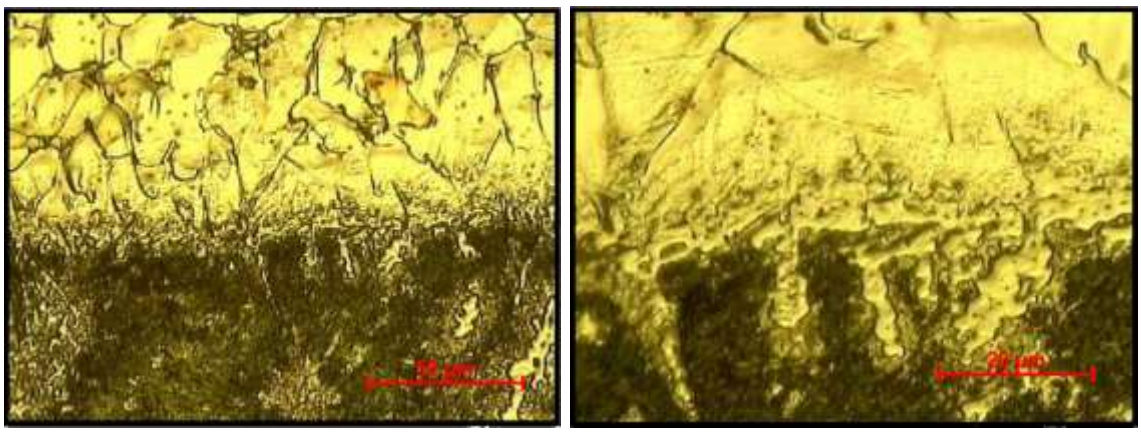

Figure (4.8): Optical microstructure of Zone 4 at higher magnifications.

The tiny grains at the clad-substrate interface and the large columnar grains were predominant on the coating sides as shown in Figure (4.9). This is because the temperatures at the sides are lower than those at the middle. Consequently, the thermal gradient and thus the cooling rate is higher [66]. This is consistent with what was revealed in 2016 by Shu et al. [54].

SEM for zones 1, 2 and 3 showed in Figure (4.4) a very small amount of carbides heterogeneously distributed through the matrix, which serve as nuclei for dendrites. The carbides and thus the dendrites increased in the zone 4. This could be attributed to the fact that the WC particles tend to sink towards the bottom of the molten pool due to the large difference in densities between WC (15.63g/cm^3) and Ni (8.9g/cm^3). The lower melting

point and slower solidification rate of the Ni provide time for the WC particles to sink towards the bottom of the molten pool [66]. Another reason is that the cooling rate at the bottom of the clad layer is faster due to its closer proximity to the cooling surface.

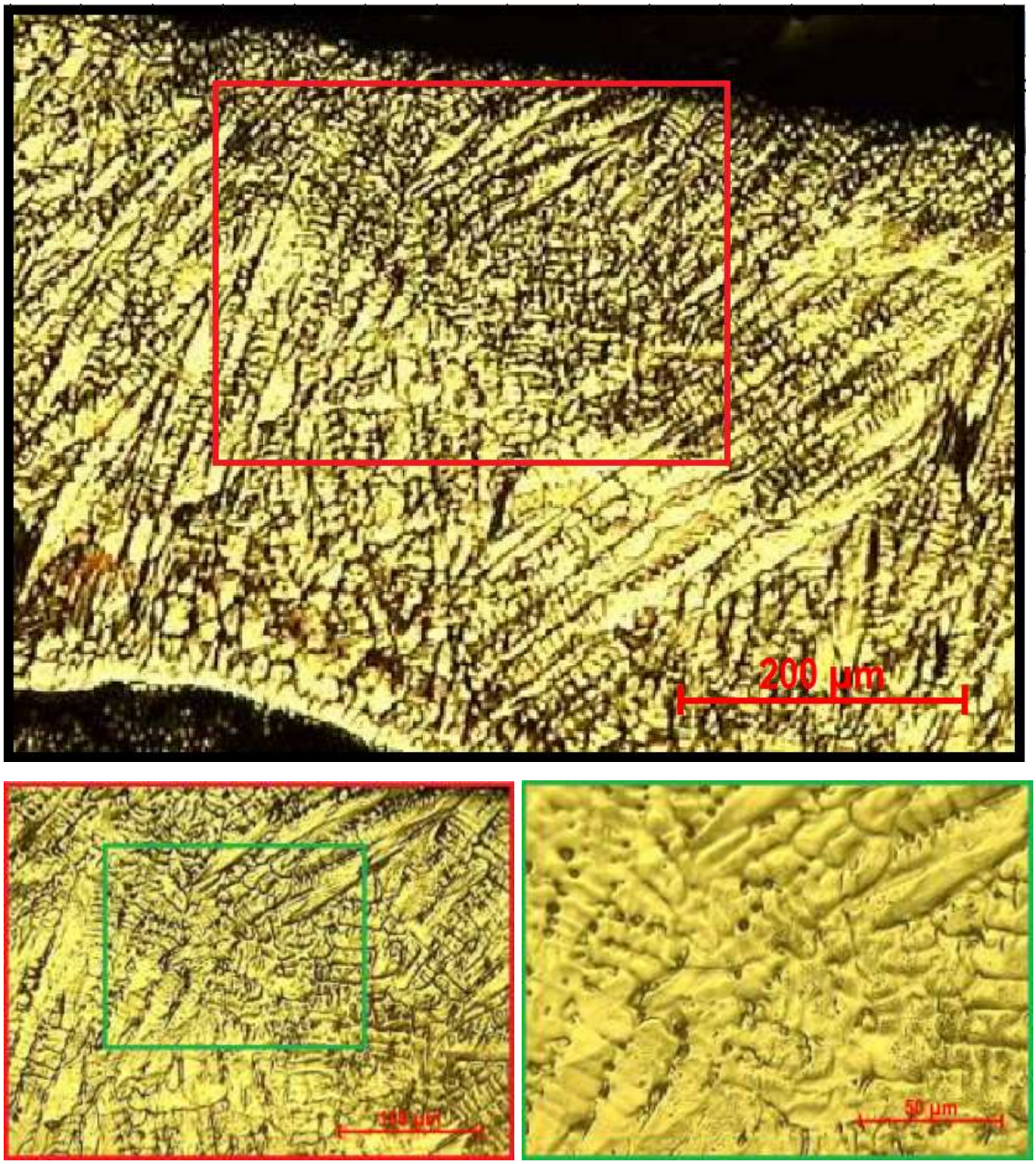

Figure (4.9): Optical microstructure of the coating sides.

The microstructure of the substrate adjacent to the interface was a mixture of various phases consisting mostly of a needle-like lower bainite, in addition to feathery bainite, pearlite and small amount of ferrite at the grain boundaries, as shown in Figure (4.10). Due to the relatively high cooling rate to which this region is exposed by the adjacent colder substrate metal, and depending on the chemical composition of the substrate (low alloy steel), the microstructure of this region was expected to consists of upper or lower bainite, martensite or a mixture of these microstructures. Figure (4.11) demonstrates the EDS map at different depths along the centerline of the cross section of the C1 clad layer.

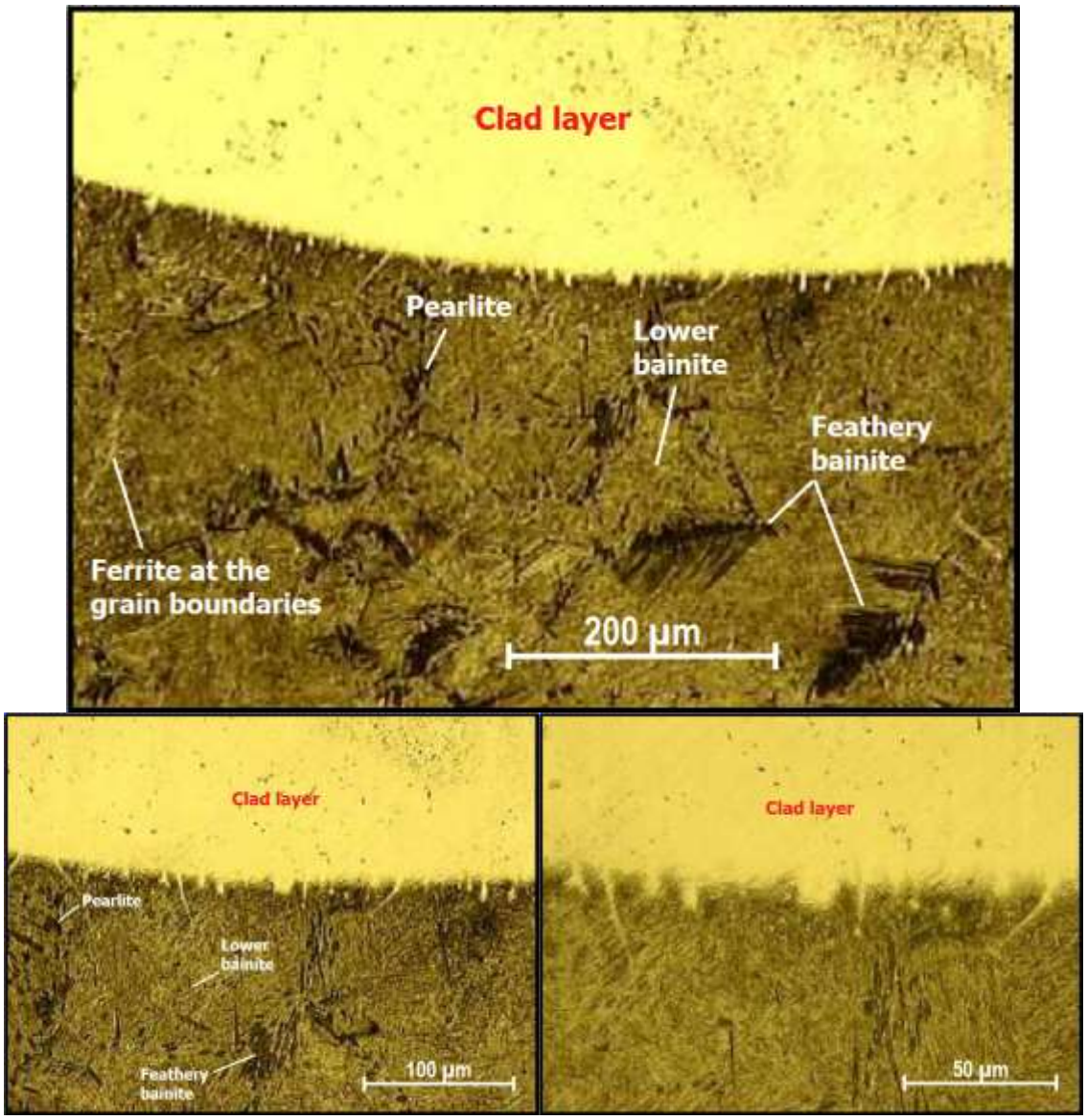

Figure (4.10): Optical microstructure of the substrate adjacent to the interface.

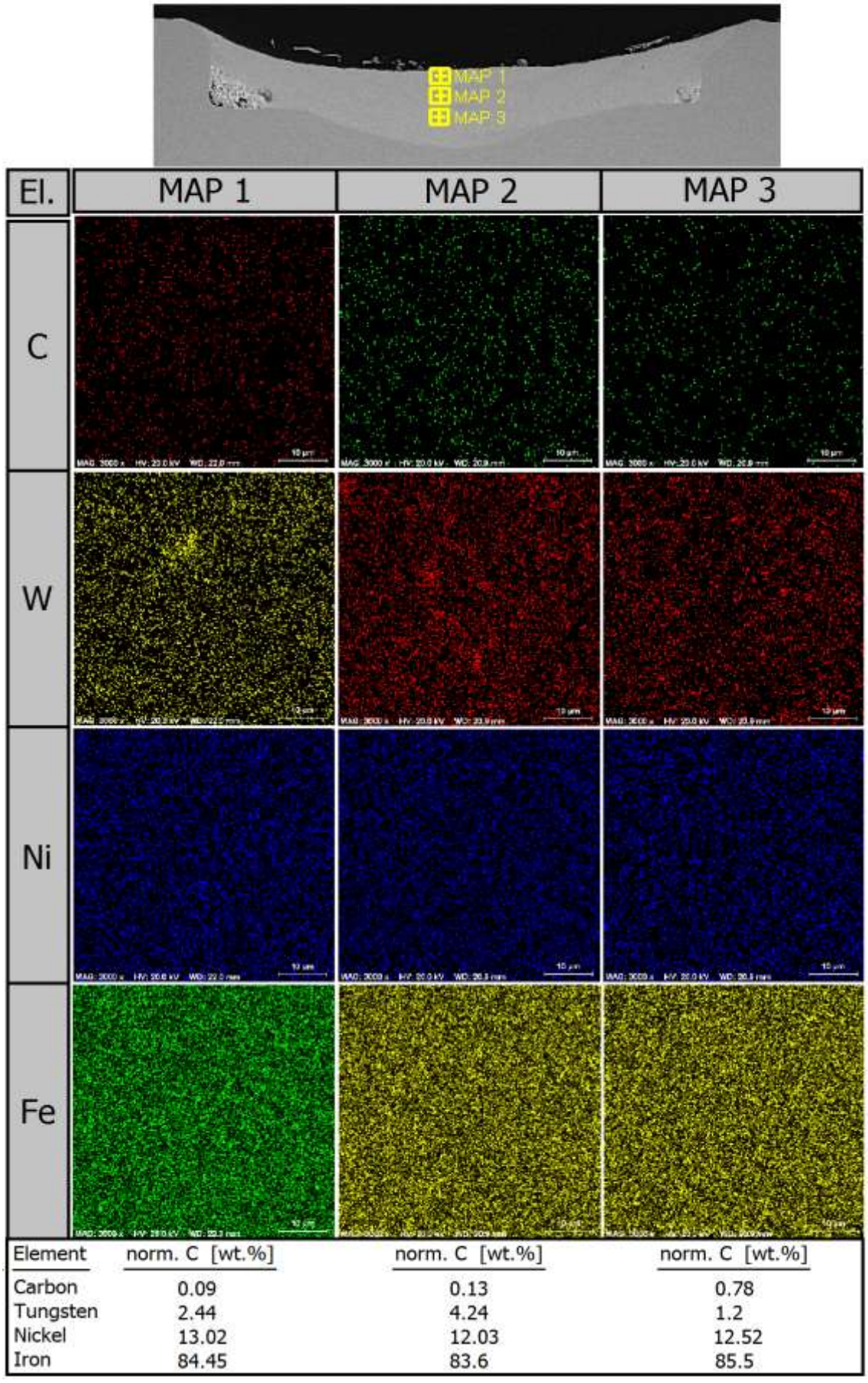

Element	norm. C [wt.%]	norm. C [wt.%]	norm. C [wt.%]
Carbon	0.09	0.13	0.78
Tungsten	2.44	4.24	1.2
Nickel	13.02	12.03	12.52
Iron	84.45	83.6	85.5

Figure (4.11): The EDS map of the C1 sample at different depths along the centerline of the cross section of the clad layer.

It is evident from the figure (4.11) that iron at the three test points was predominant (84.5 wt.% on average) at the expense of other elements (12.5% Ni, 2.6% W and 0.3% C by weight on average), although the pre-placed composite paste of this sample consisted of 70 wt.% Ni-30 wt.% WC and free of iron. This is due to the effect of dilution with the substrate material (low alloy steel). The content of iron was comparable at the three test points (also for nickel), while the content of carbon and tungsten was disparate. When compared to the point of MAP 1, the carbon and tungsten contents notably increased at MAP 2 point. This might be attributed to the relatively high density of the acicular WC in this zone (near Zone 2 in Figures 4.4 and 4.6).

4.3.1 The Effect of Increasing the wt.% of Tungsten Carbide

Microscopy of the C2 sample resulting from increasing the wt.% of WC to 40% revealed in Figure (4.12) that the microstructure of Zone 1 of the clad layer consists of nickel solid solution dendrites with WC particles distributed through the matrix. Figure (4.13) shows the optical and scanning electron microstructures of this zone with higher magnifications, where a notable increase in dendrites was, compared to those that appeared in Zone 1 of the C1 sample (Figure 4.4). This is due to the increased wt.% of tungsten carbides in the pre-placed composite paste, which act as nuclei for dendrites. The density of dendrites slightly increased in Zone 2, therefore, the microstructure of this zone in Figure (4.12) looked like finer to some extent. Figure (4.14) shows the microstructure of Zone 2 at higher magnifications using the OM and SEM. The microscopy of Zone 3 revealed that the dendrites were mostly columnar, especially those appeared in SEM. Figure (4.15) presents the optical and scanning electron microstructures of Zone 3 at higher magnifications. Both the OM and SEM in Figures (4.12 and 4.16) showed that the columnar dendrites were more dominant in Zone 4.

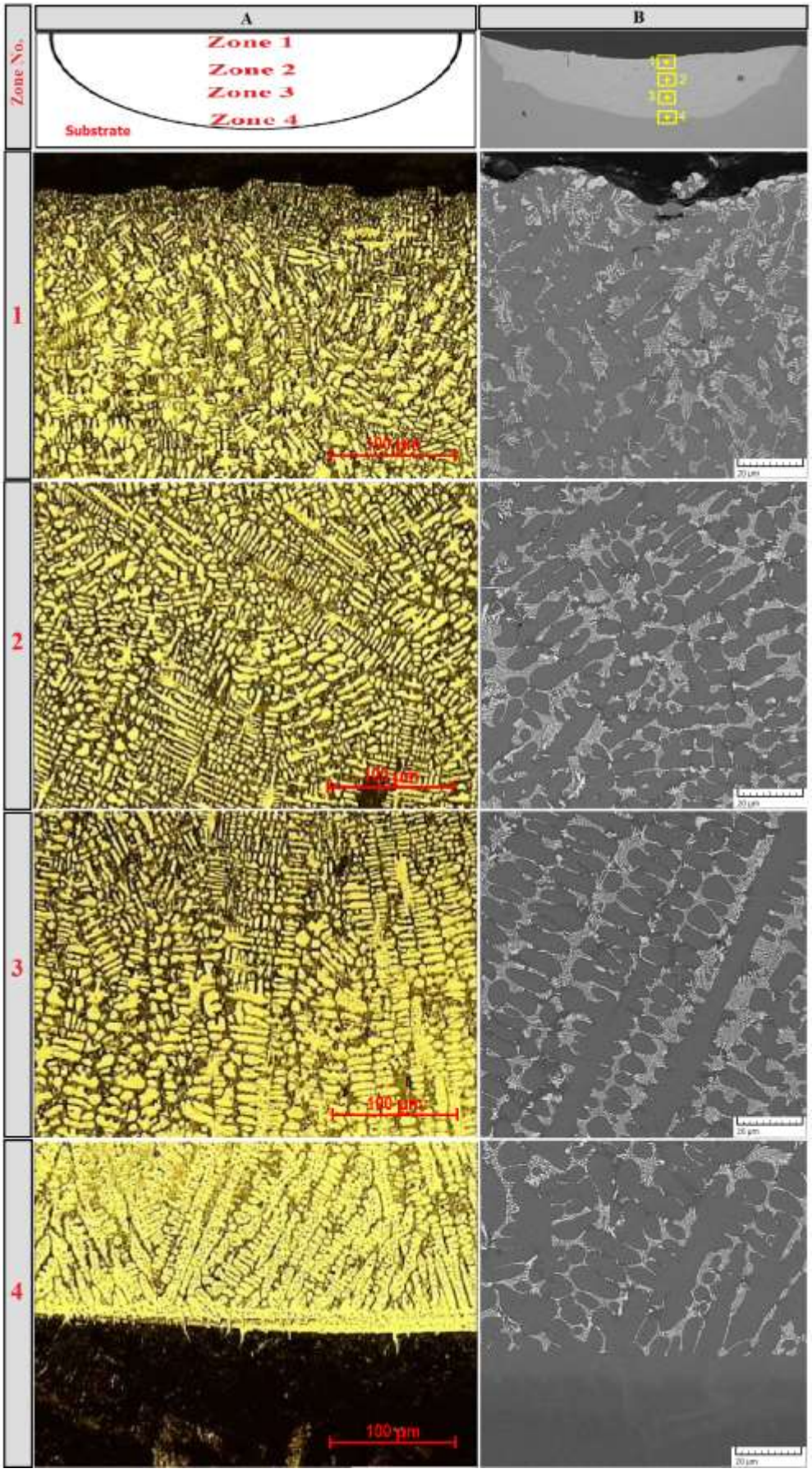

Figure (4.12): Microstructural map of the C2 sample at different depths along the centerline of the cross section of the clad layer using an (A): OM and (B): SEM.

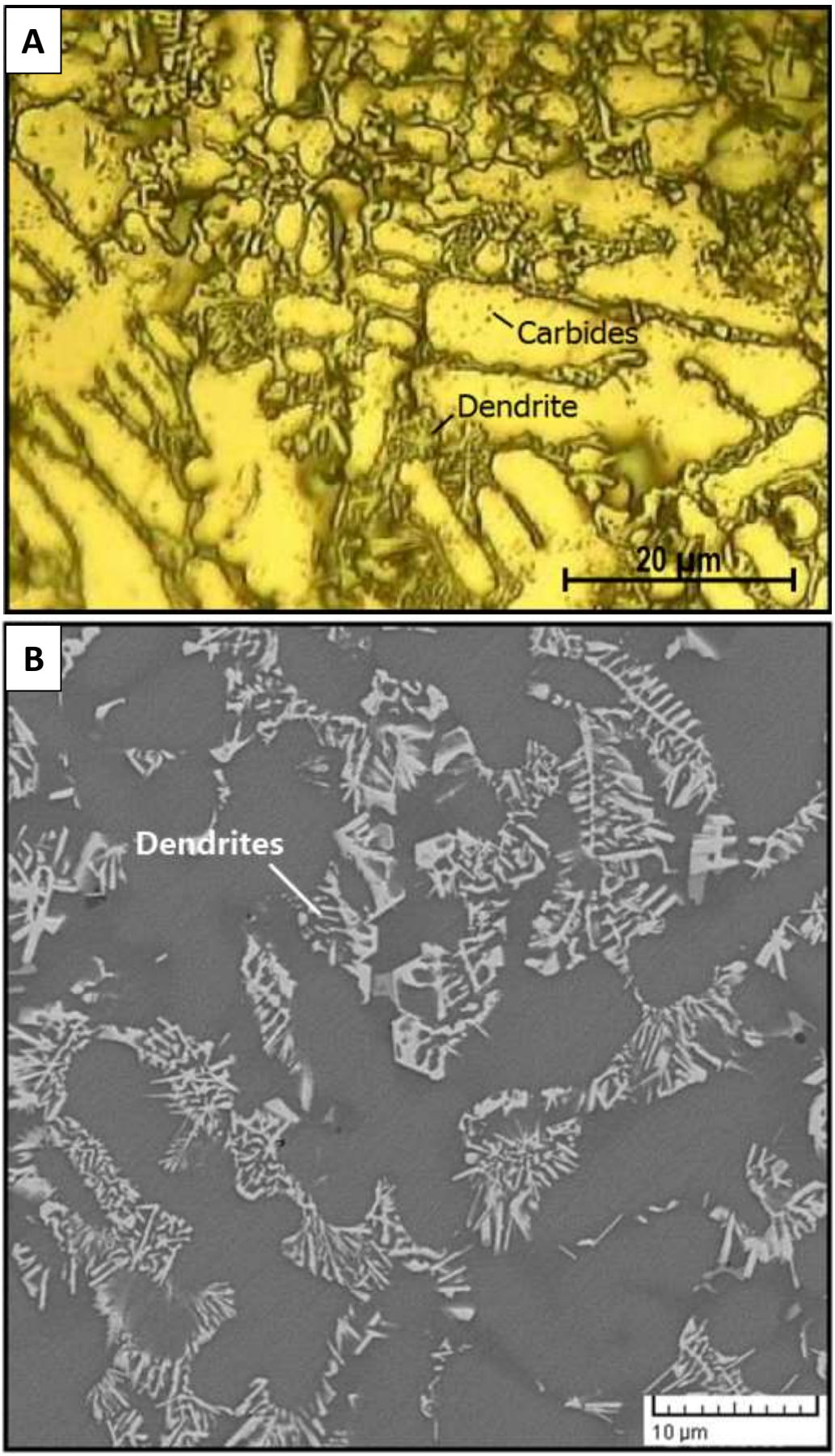

Figure (4.13): Microstructure of Zone 1 of the C2 sample at higher magnifications using an (A): OM and (B): SEM.

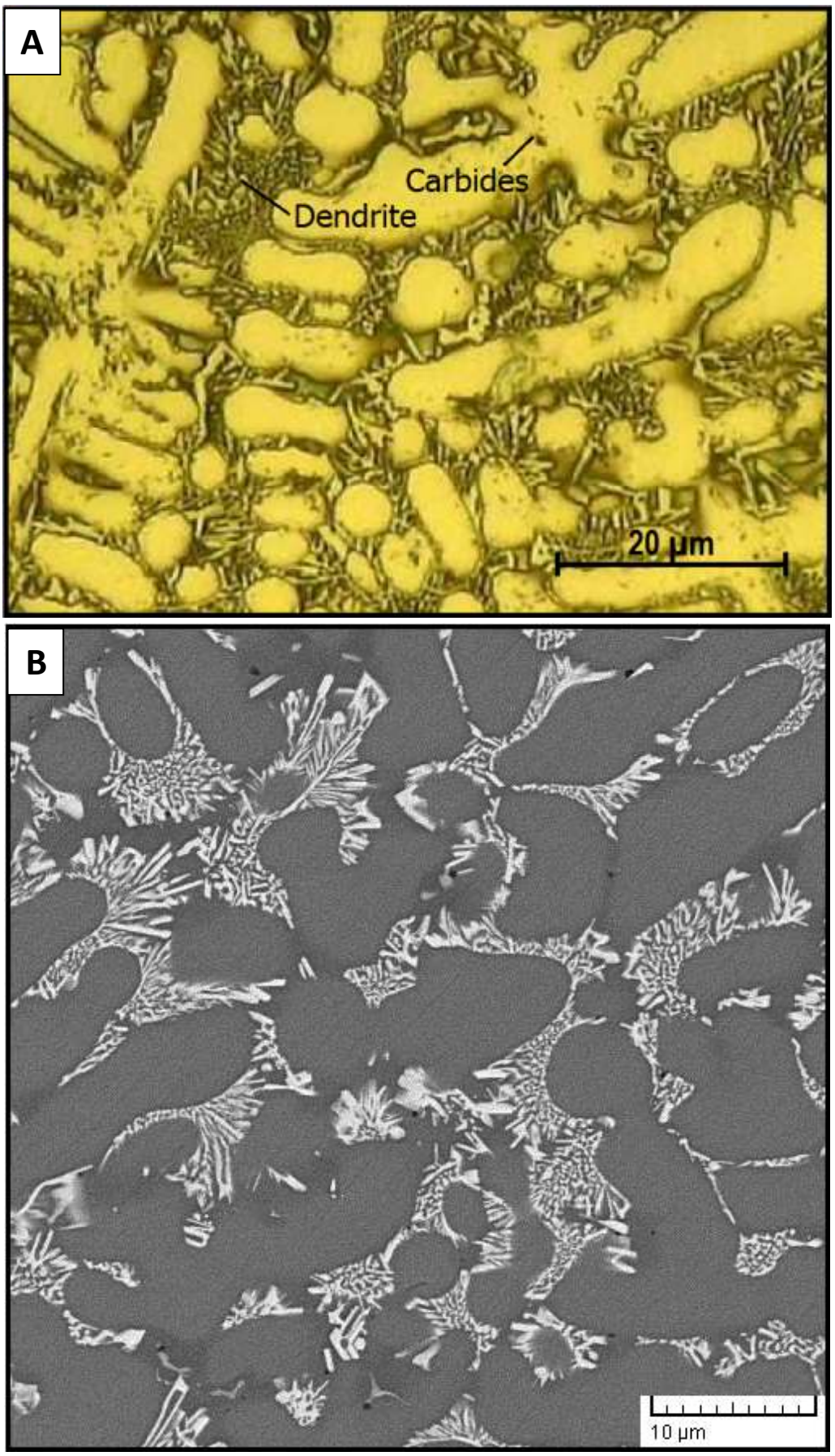

Figure (4.14): Microstructure of Zone 2 of the C2 sample at higher magnifications using an (A): OM and (B): SEM.

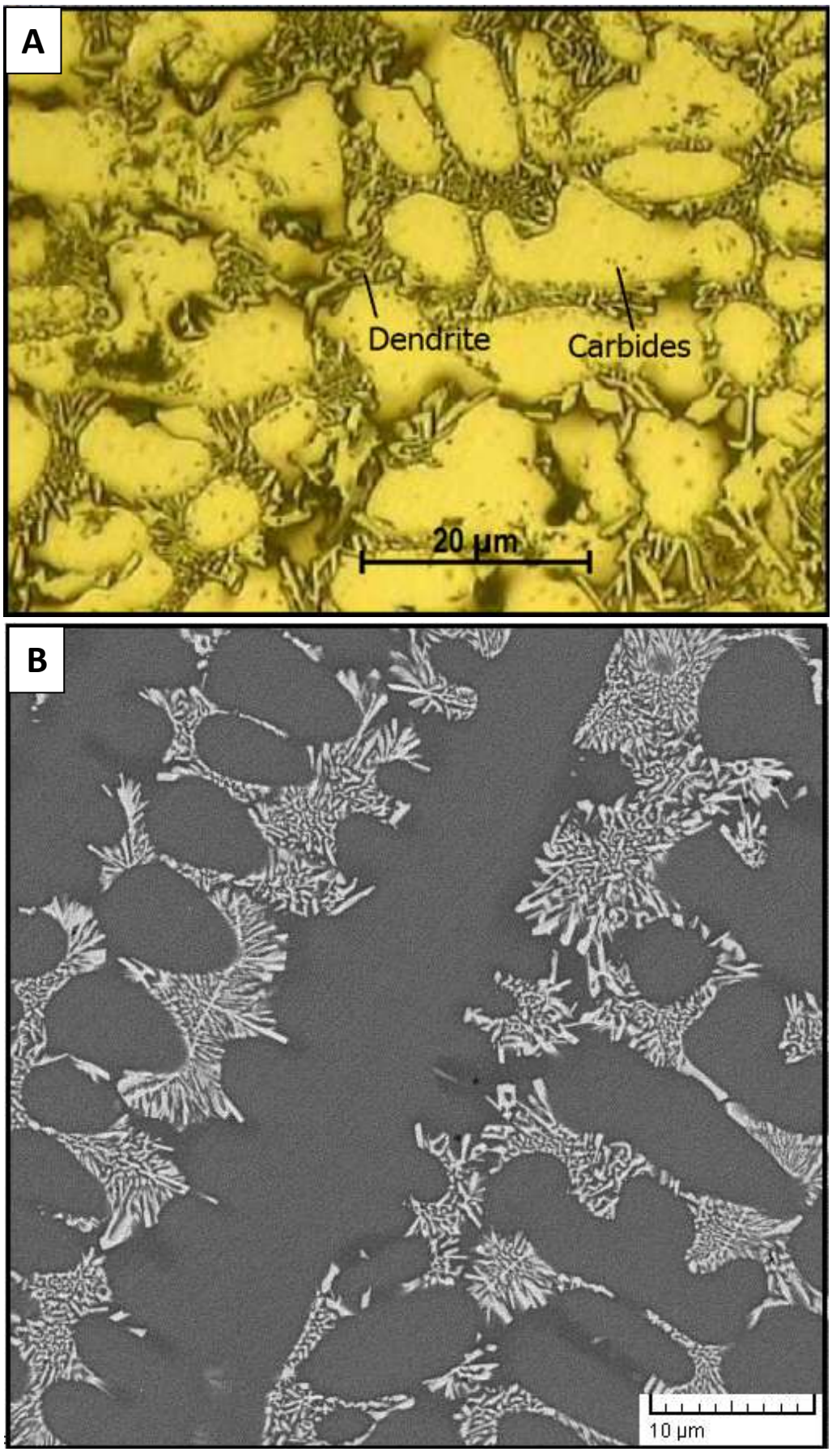

Figure (4.15): Microstructure of Zone 3 of the C2 sample at higher magnifications using an (A): OM and (B): SEM.

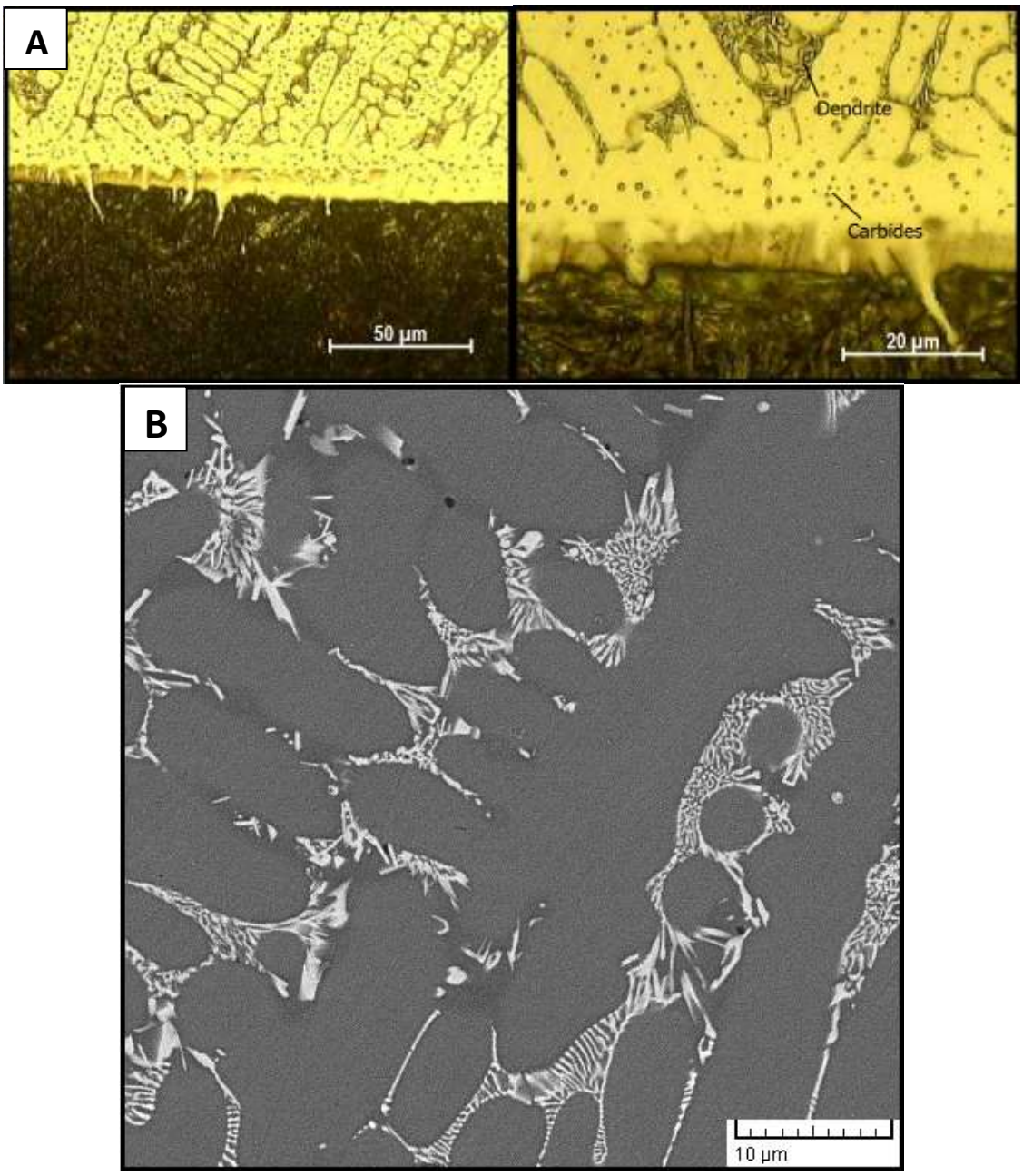

Figure (4.16): Microstructure of Zone 4 of the C2 sample at higher magnifications using an (A): OM and (B): SEM.

It is clearly noted that the columnar grains were more in Zone 4 of this sample compared to those in the corresponding zone of the C1 sample. This might be attributed to the fact that increasing the wt.% of WC increases the cooling rate which enhances the formation of the columnar dendrites [54]. The dilution between the clad layer and the substrate at the interface shown in Figure (4.16A) appears to be less than that occurred in the C1 sample. Figure (4.17) demonstrates the EDS map at different depths along the centerline of the cross section of the C2 clad layer.

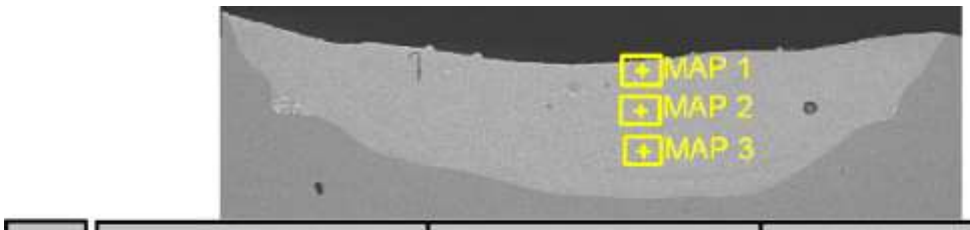

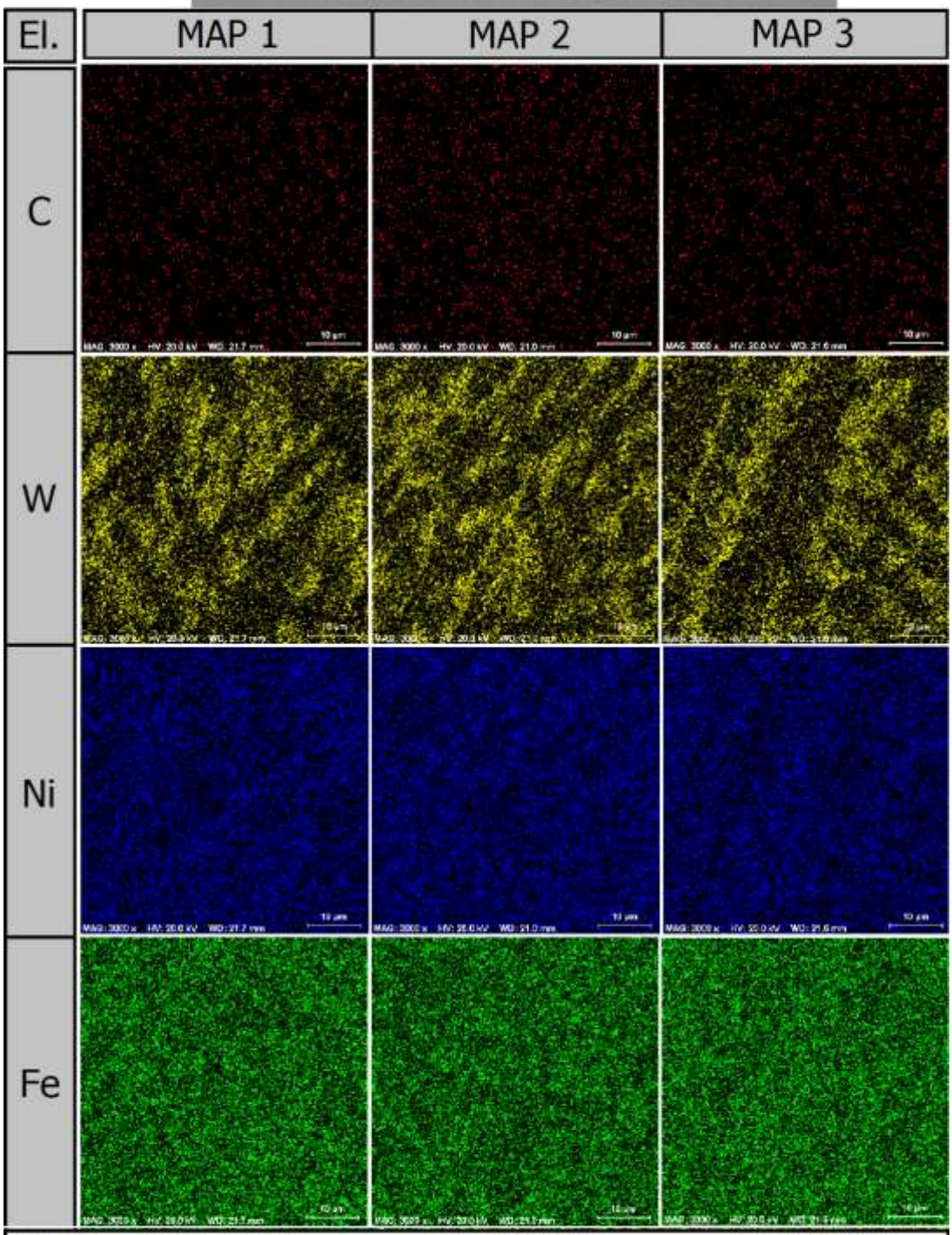

Element	norm. C [wt.%]	norm. C [wt.%]	norm. C [wt.%]
Carbon	0.98	2.82	1.61
Tungsten	20.22	18.75	21.83
Nickel	31.69	32.92	31.67
Iron	47.12	45.50	44.89

Figure (4.17): The EDS map of the C2 sample at different depths along the centerline of the cross section of the clad layer.

It is apparent that the content of each element was comparable at the three test points with averages of 45.8% Fe, 32.1% Ni, 20.3% W and 1.8% C. The iron content in the clad layer of this sample is also more than the other elements, but it is much lower than that in the C1 clad layer. This confirms that the dilution with the substrate material in this sample was lower (Figure 4.16A). The reason behind this might be attributed to the fact that with increasing the wt.% of WC particles in the pre-placed coating layers, the TIG cladding current required is higher [71]. Therefore, with the use of the same current value of the C1 sample, the dilution will be lower. It is also noted that the distribution of the W element at the three test points in Figure (4.17) clearly indicates the locations and orientations of the dendrites shown in SEM Figures (4.13, 4.14 and 4.15). This is because the WC particles serve as nuclei for the dendrites, as mentioned earlier.

Microscopy revealed in Figure (4.18) that the microstructures at the different zones along the cross section of the C3 clad layer are notably finer than those at the corresponding zones of the C2 sample. This could be due to increasing the wt.% of WC in the composite to 50%, which in turn increases the dendrite nuclei and acts as an obstacle to the growth of dendrites [79,80]. Therefore, SEM shows that the proportion of dendrites at the different zones is much more than that which appeared at the corresponding zones of the C2 sample. Figure (4.19) shows the optical and scanning electron microstructures in zones 1 and 2 at higher magnifications which consist of a higher proportion of nickel solid solution dendrites with WC particles distributed through the matrix. The dark regions appeared in the optical microstructural examination of Zone 3 shown in Figure (4.18) are actually dendrites with dense branches. This might be due to the effect of increasing the wt.% of WC, which in turn increases the cooling rate. The SEM of the same zone shows a relatively large sized of WC particles remained intact, without decomposition distributed through matrix.

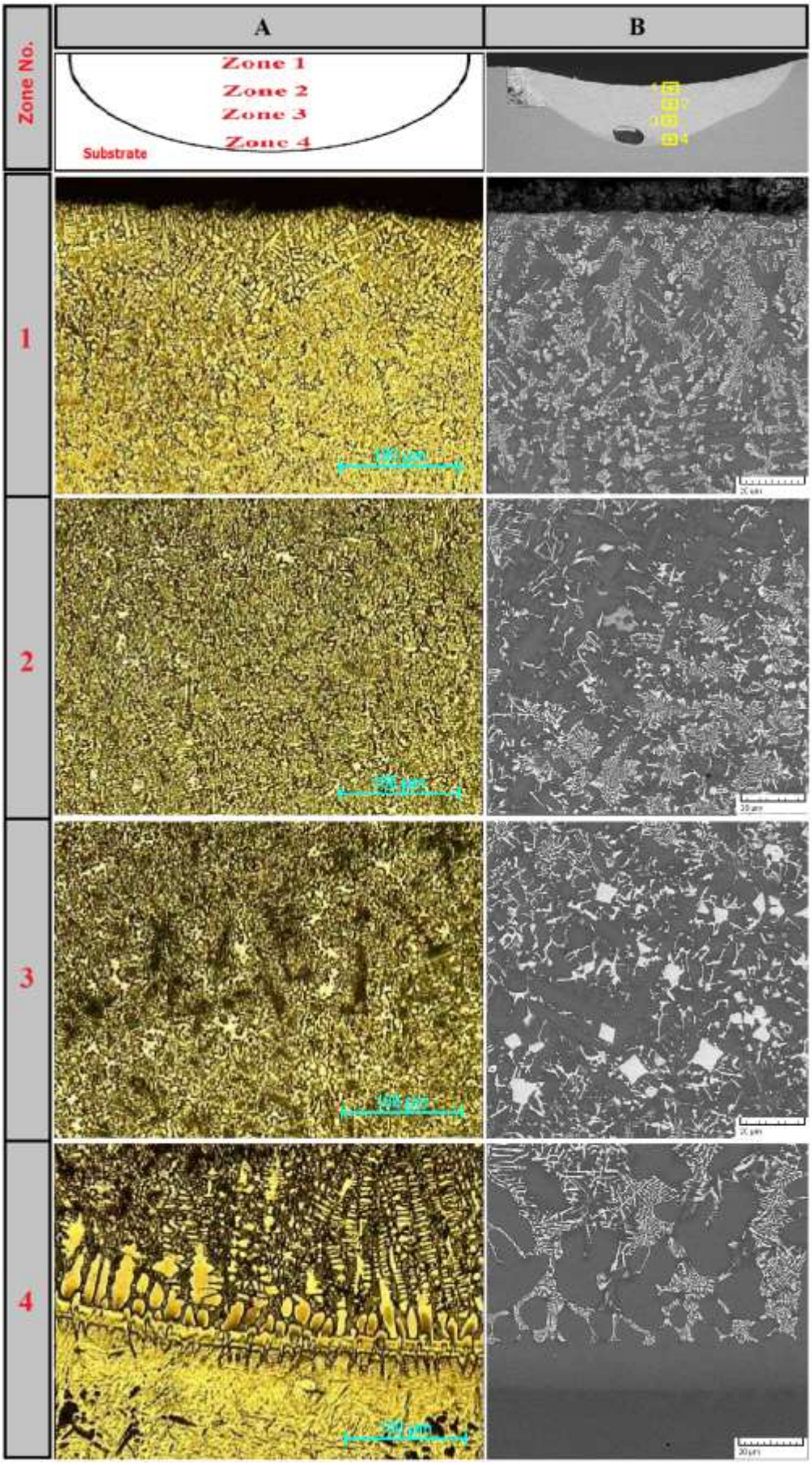

Figure (4.18): Microstructural map of the C3 sample at different depths along the centerline of the cross section of the clad layer using an (A): OM and (B): SEM.

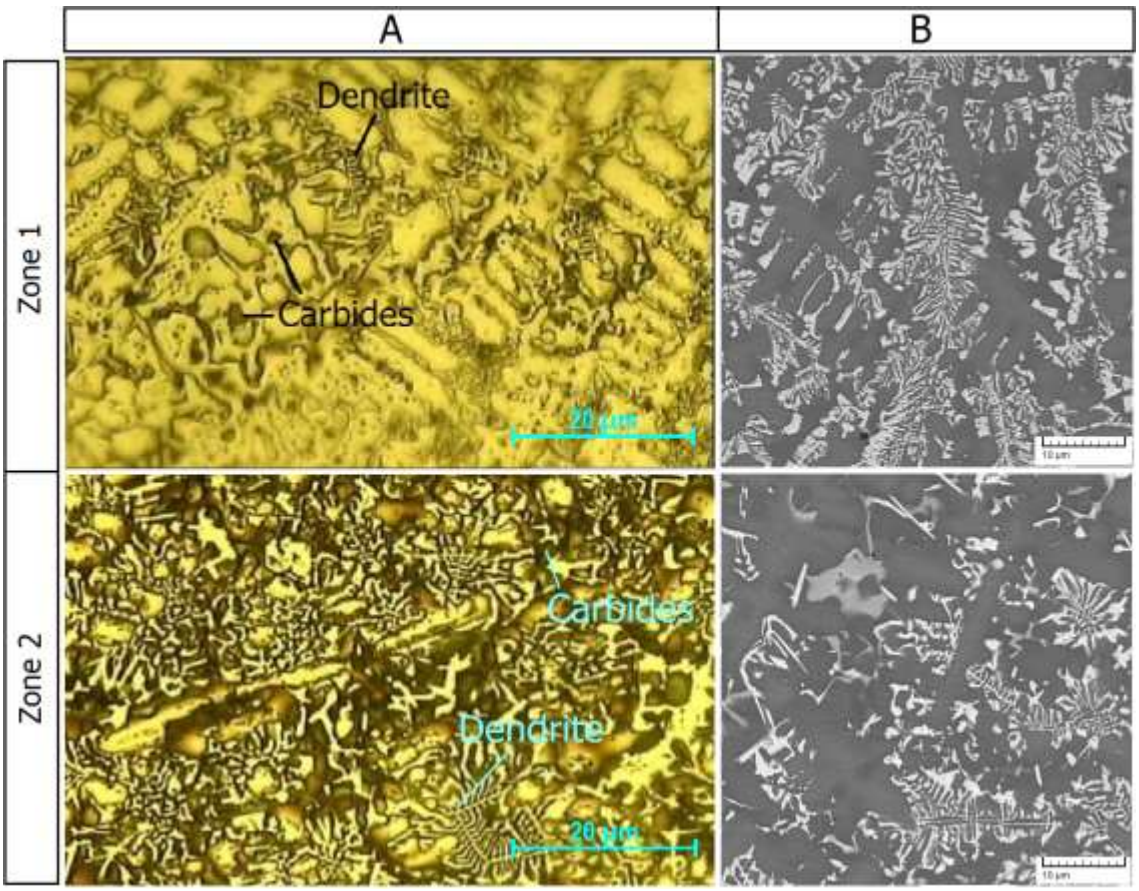

Figure (4.19): Microstructure of Zones 1 and 2 of the C3 sample at higher magnifications using an (A): OM and (B): SEM.

However, some of the finer particles may suffer from decomposition or surface melting during contact with the molten constituents [77,78]. Figure (4.20) presents the optical and scanning electron microstructures of Zone 3 at higher magnifications.

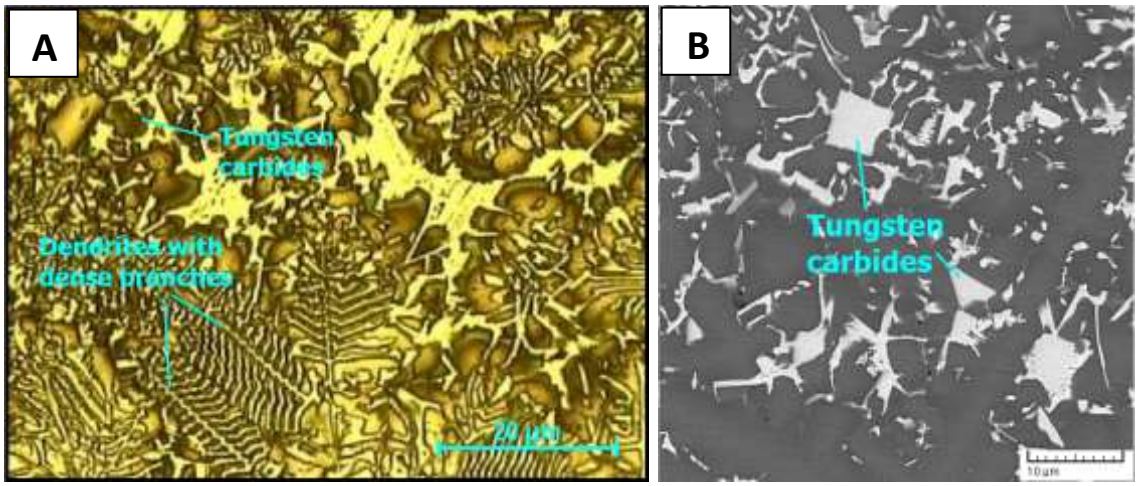

Figure (4.20): Microstructure of Zone 3 of the C3 sample at higher magnifications using an (A): OM and (B): SEM.

The optical microscopy for Zone 4 revealed in Figure (4.18) that the structure at the bottom of the molten pool is firstly planar and dentate towards the top of the pool, and then the structure becomes dendritic with releasing latent solidification heat, as reported in 2018 by Sabzi et al [67]. Figure (4.21) shows the microstructure of Zone 4 at higher magnifications, where the dilution at the interface between the clad layer and the substrate material is very clear, indicating a good bonding between them.

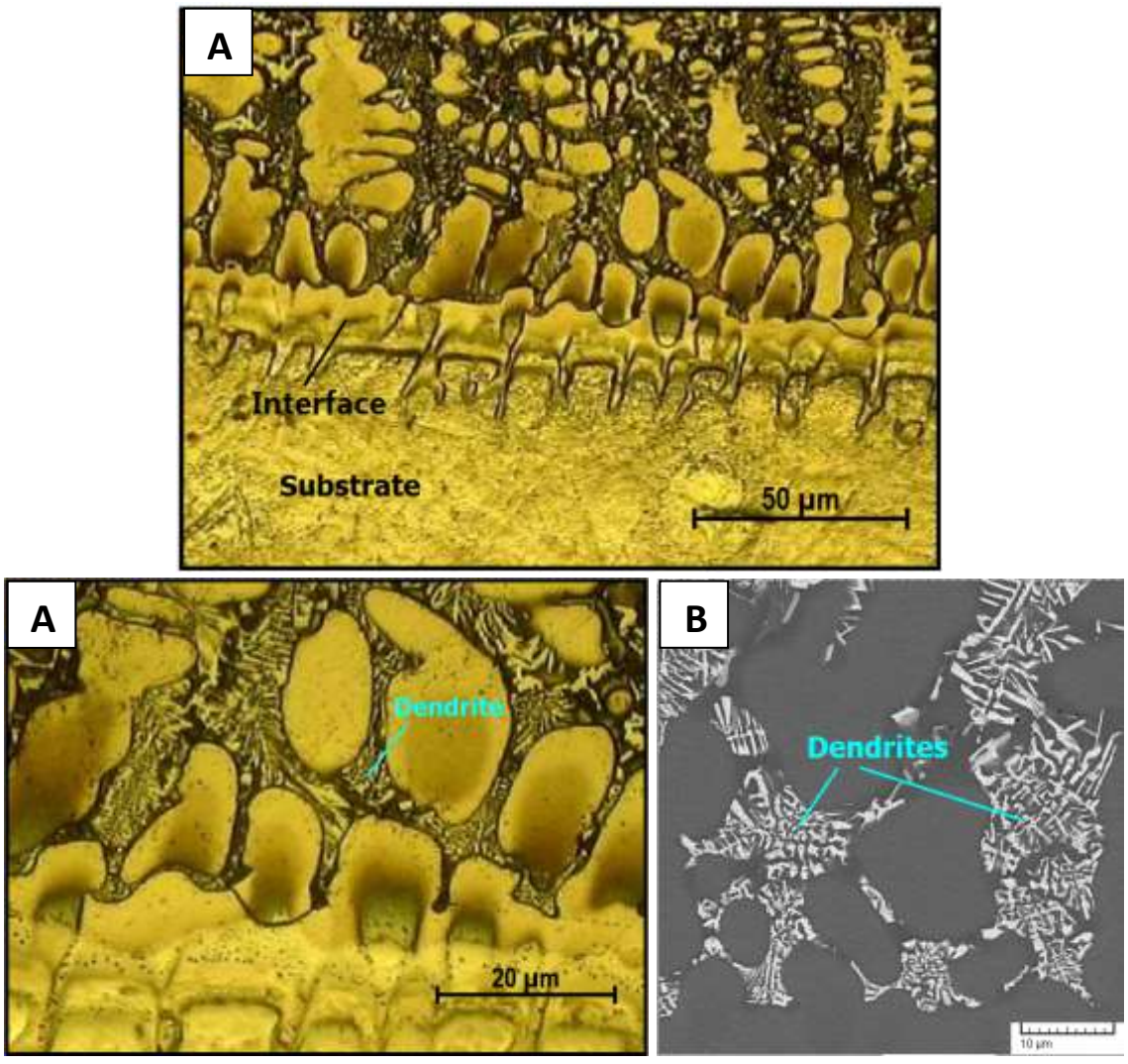

Figure (4.21): Microstructure of Zone 4 of the C3 sample at higher magnifications using an (A): OM and (B): SEM.

The EDS map along the centerline of the cross section of the C3 clad layer shows in Figure (4.22) that the content of each element was comparable at the three test points with averages of 46.1% Fe, 28.3% Ni, 24.6% W and 1.1% C.

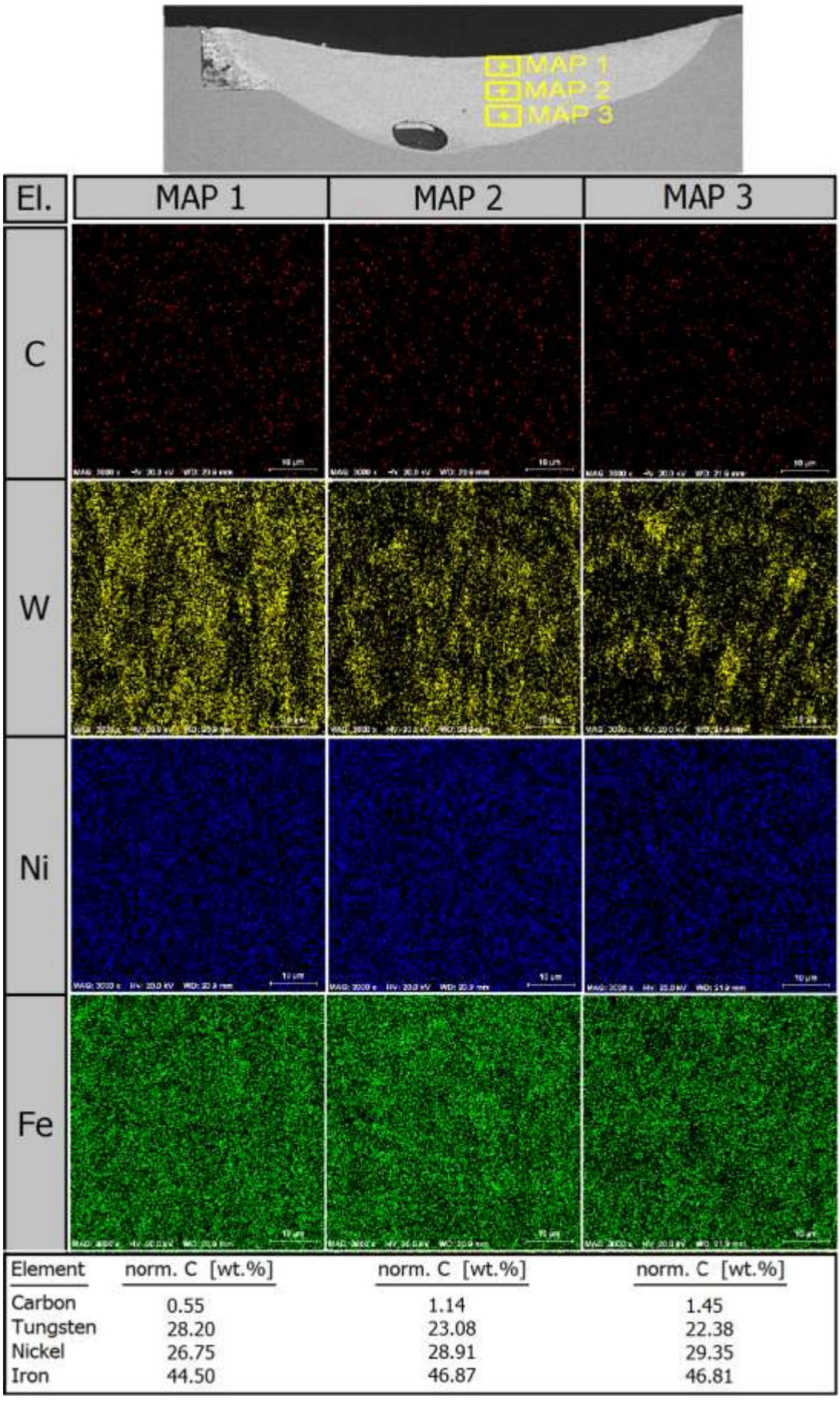

Element	norm. C [wt.%]	norm. C [wt.%]	norm. C [wt.%]
Carbon	0.55	1.14	1.45
Tungsten	28.20	23.08	22.38
Nickel	26.75	28.91	29.35
Iron	44.50	46.87	46.81

Figure (4.22): The EDS map of the C3 sample at different depths along the cross section of the clad layer.

The iron content in the clad layer of this sample is very comparable to that of the C2 sample, indicating the similarity of the dilution ratio, whereas the tungsten content is notably higher at the expense of the nickel content. This is due to the increased wt.% of the WC in the composite of this sample to 50%. As in the C2 sample, the distribution of the W element at the three test points in Figure (4.22) clearly indicates the locations and orientations of the dendrites, as well as the relatively large WC particles distributed through matrix (Zone 3) shown in SEM Figures (4.18 and 4.20).

Increasing the wt.% of WC in the C4 composite to 60% clearly enhanced the proportion of dendrites in the four zones shown in Figure (4.23) compared to the C3 sample. The dendrites were also more densely branched in all four zones. This is attributed to the fact that the increase in the wt.% of WC increases the cooling rate, as already mentioned. As in the C3 sample, some relatively large WC particles appeared with SEM of Zone 3, distributed through the matrix. The OM for Zone 4 revealed in Figure (4.23) that the structure at the clad layer-substrate interface of this sample is somewhat similar to that of the C3 sample. Figure (4.24) shows the optical and scanning electron microstructures of all four zones at higher magnifications, where the increase of dendrites and carbides at the expense of the matrix is very evident.

The EDS map along the centerline of the cross section of the C4 clad layer shows in Figure (4.25) that the content of each element was highly comparable at the three test points with averages of 51.1% Fe, 20.8% Ni, 26.7% W and 1.4% C. Since the wt.% of WC in the composite of this sample increased to 60%, the W content is higher than that of the C3 sample at the expense of the Ni content. So, the dendrites and carbides notably increased at the expense of the matrix (Figures 4.23 and 4.24). The distribution of the W element at the test points indicates the locations and orientations of the dendrites and W-carbides shown in SEM Figures.

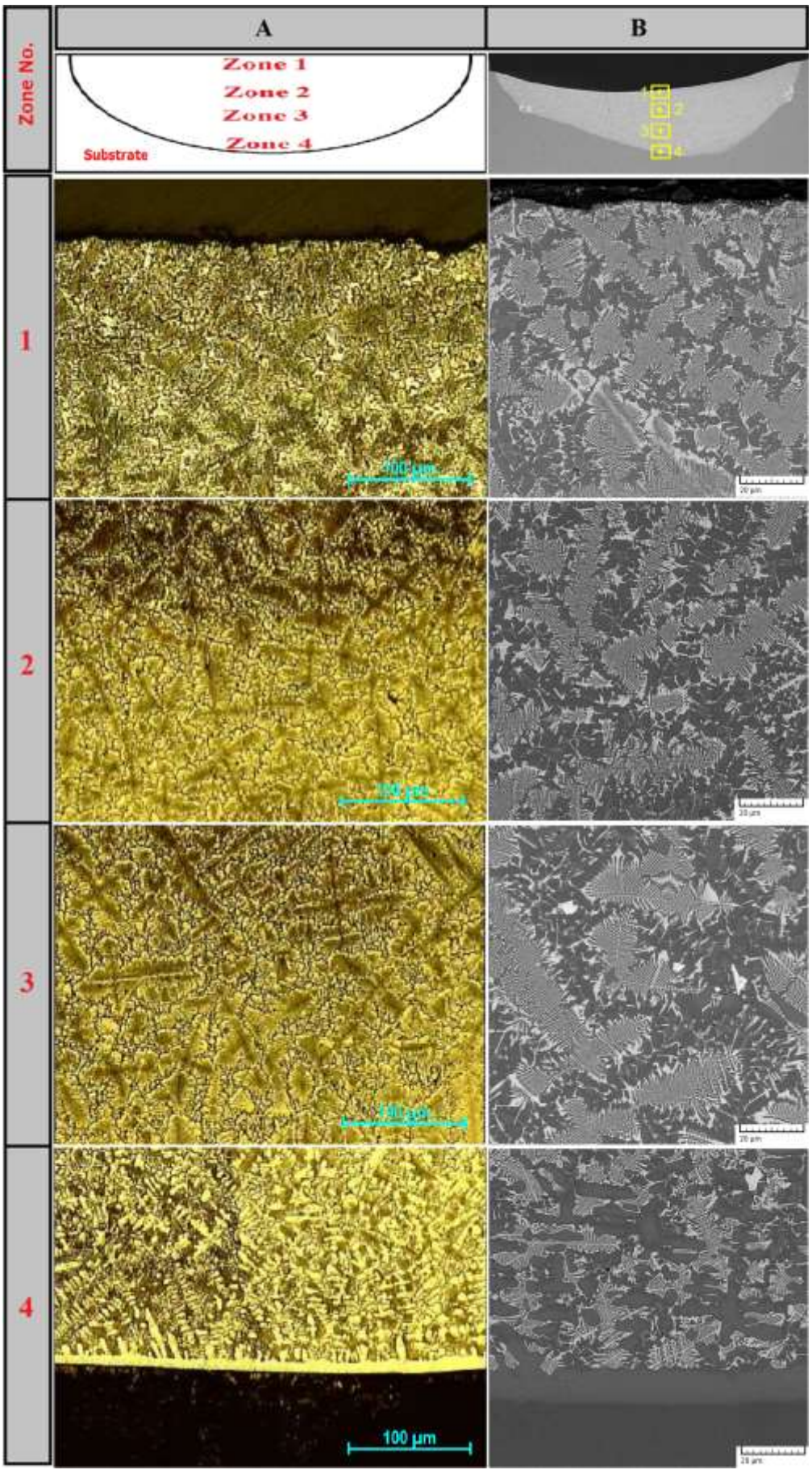

Figure (4.23): Microstructural map of the C4 sample at different depths along the centerline of the cross section of the clad layer using an (A): OM and (B): SEM.

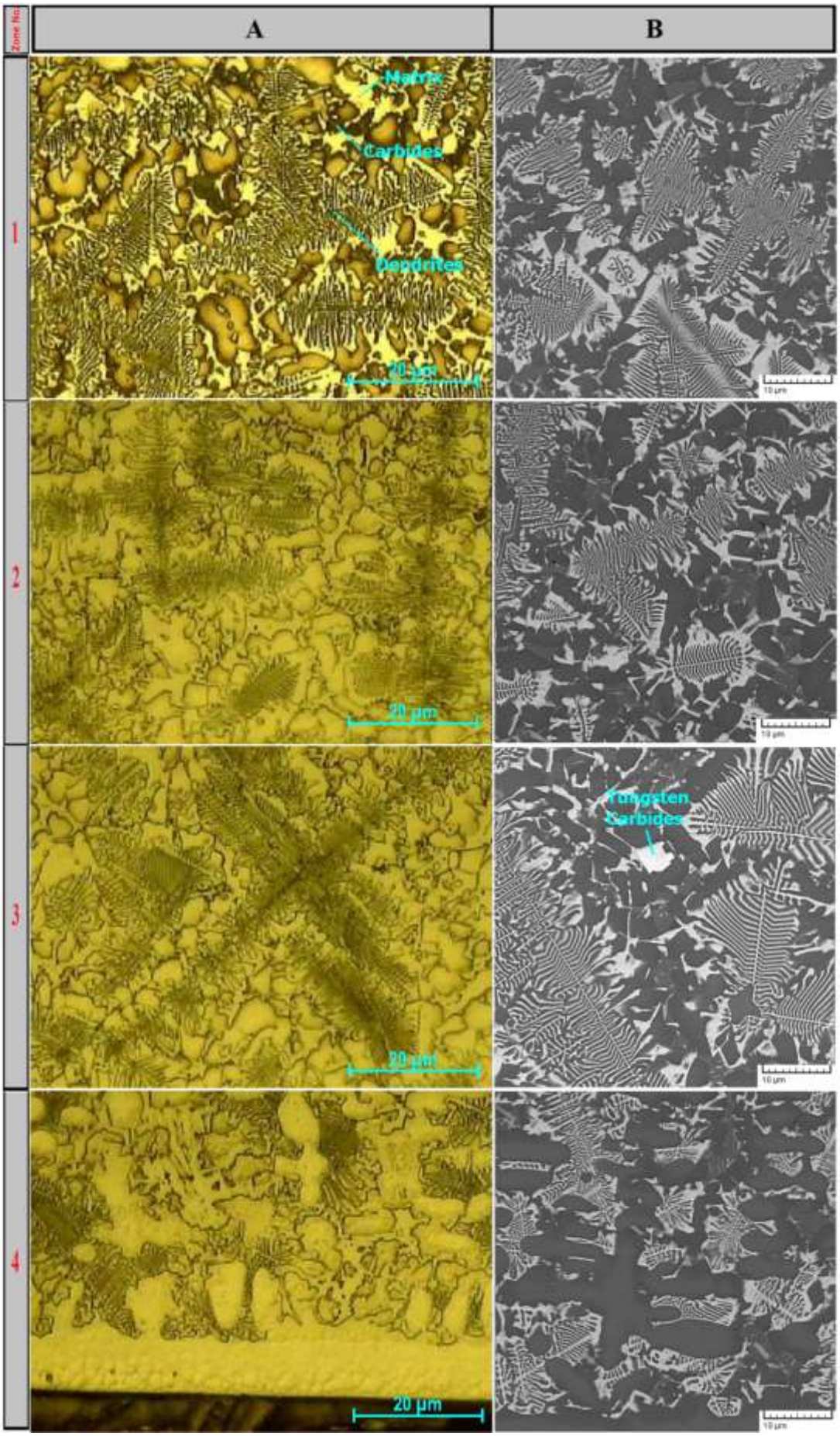

Figure (4.24): Microstructures of the C4 sample in the different zones at higher magnifications using an (A): OM and (B): SEM.

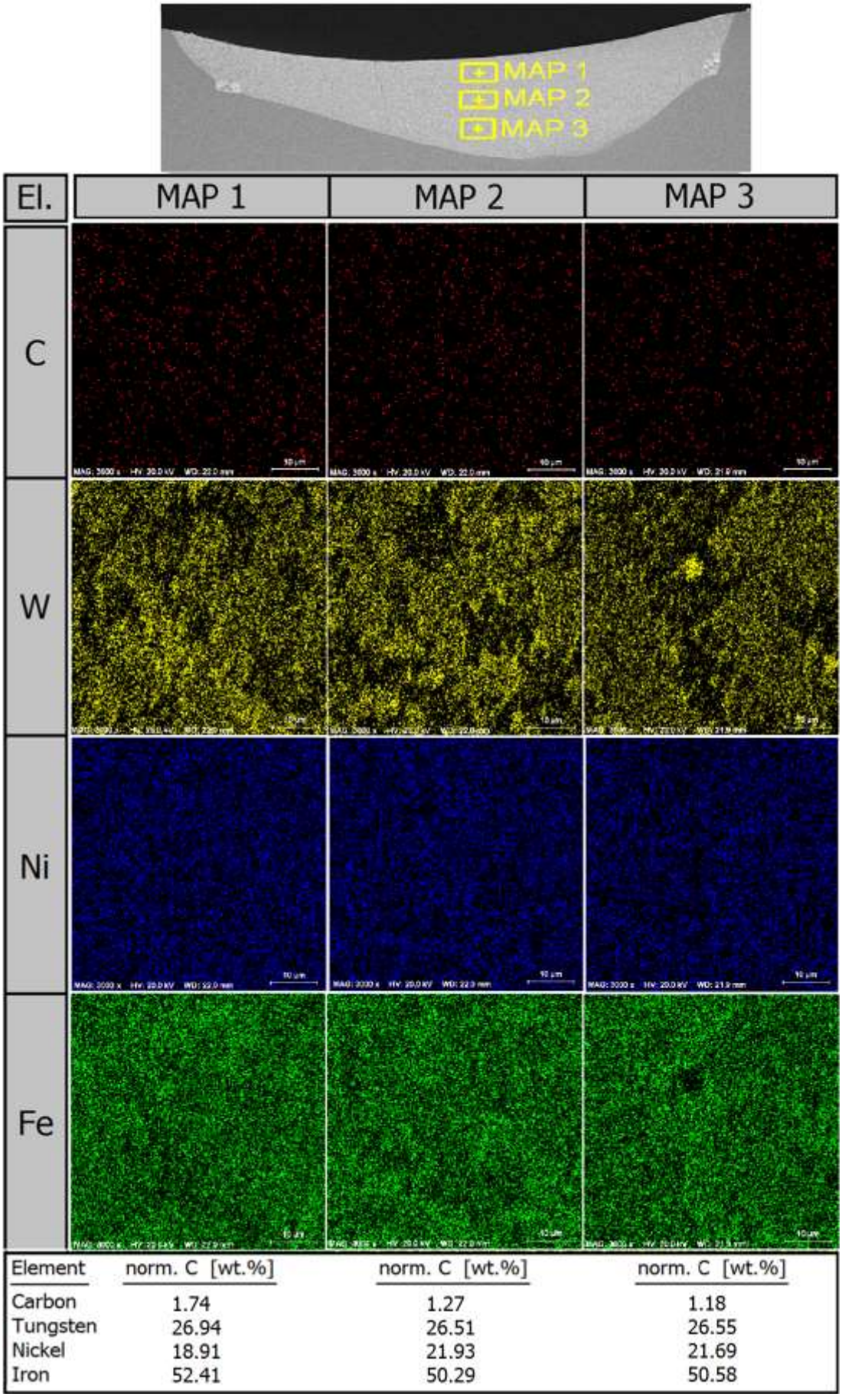

Element	norm. C [wt.%]	norm. C [wt.%]	norm. C [wt.%]
Carbon	1.74	1.27	1.18
Tungsten	26.94	26.51	26.55
Nickel	18.91	21.93	21.69
Iron	52.41	50.29	50.58

Figure (4.25): The EDS map of the C4 sample at different depths along the cross section of the clad layer.

The increase of the WC weight percentage to 70% at the expense of nickel in the composite layer deposited in the C5 sample led to the formation of a microstructure of dendrites finer than what appeared in the C4 as shown in Figure (4.26). In addition, the optical and scanning electron microstructures show that the dendrites were mostly columnar in all four zones. The reason behind these two observations could be the higher cooling rates associated with increasing the wt.% of WC in the composite [54]. Another observation is the relative increase in the proportion of matrix in this sample compared to that observed in the C4 sample. Figure (4.27) shows the optical and scanning electron microstructures of the C5 clad layer with higher magnifications, where the tungsten carbides distributed through the matrix were significantly increased.

The EDS map along the centerline of the cross section of the C5 sample shows in Figure (4.28) that the content of each element at the three test points was highly comparable too with averages of 62.5% Fe, 15.3% Ni, 20.9% W and 1.3% C. It can easily be noted that with increasing the wt.% of WC in the composite of this sample to 70%, the W content is higher than that of the Ni. It is also noted that the average weight percentage of iron is relatively high (62.5%) at the expense of the other elements. This indicates a greater dilution and a higher participation of iron in the matrix. This might explain why the matrix proportion of this sample is higher as shown in Figure (4.27) comparing to the corresponding figure of the C4 sample (Figure 4.24). The distribution of the W element at the three test points indicates the locations and orientations of the columnar dendrites, which appeared clearly in the SEM shown in Figures (4.26 and 4.27).

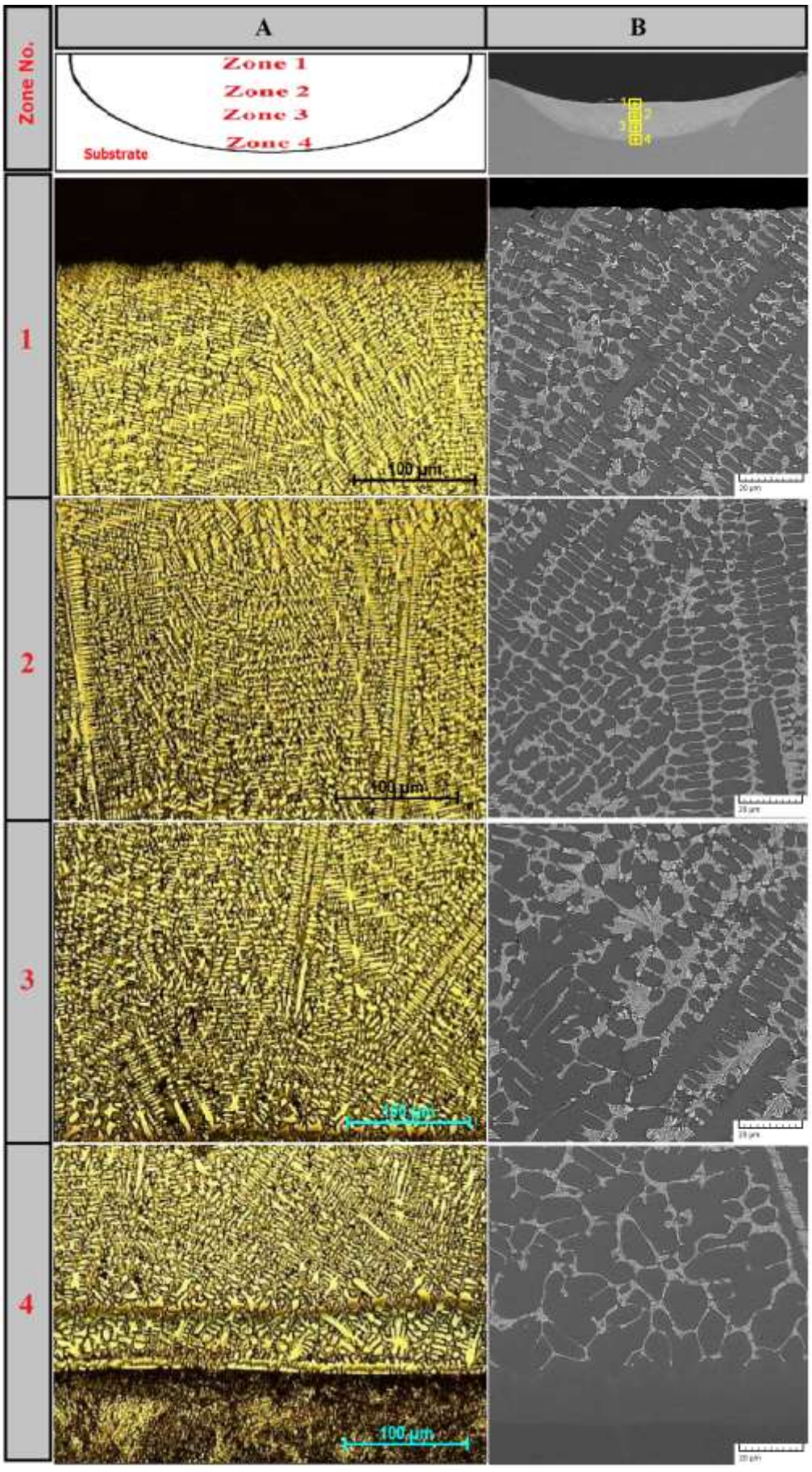

Figure (4.26): Microstructural map of the C5 sample at different depths along the centerline of the cross section of the clad layer using an (A): OM and (B): SEM.

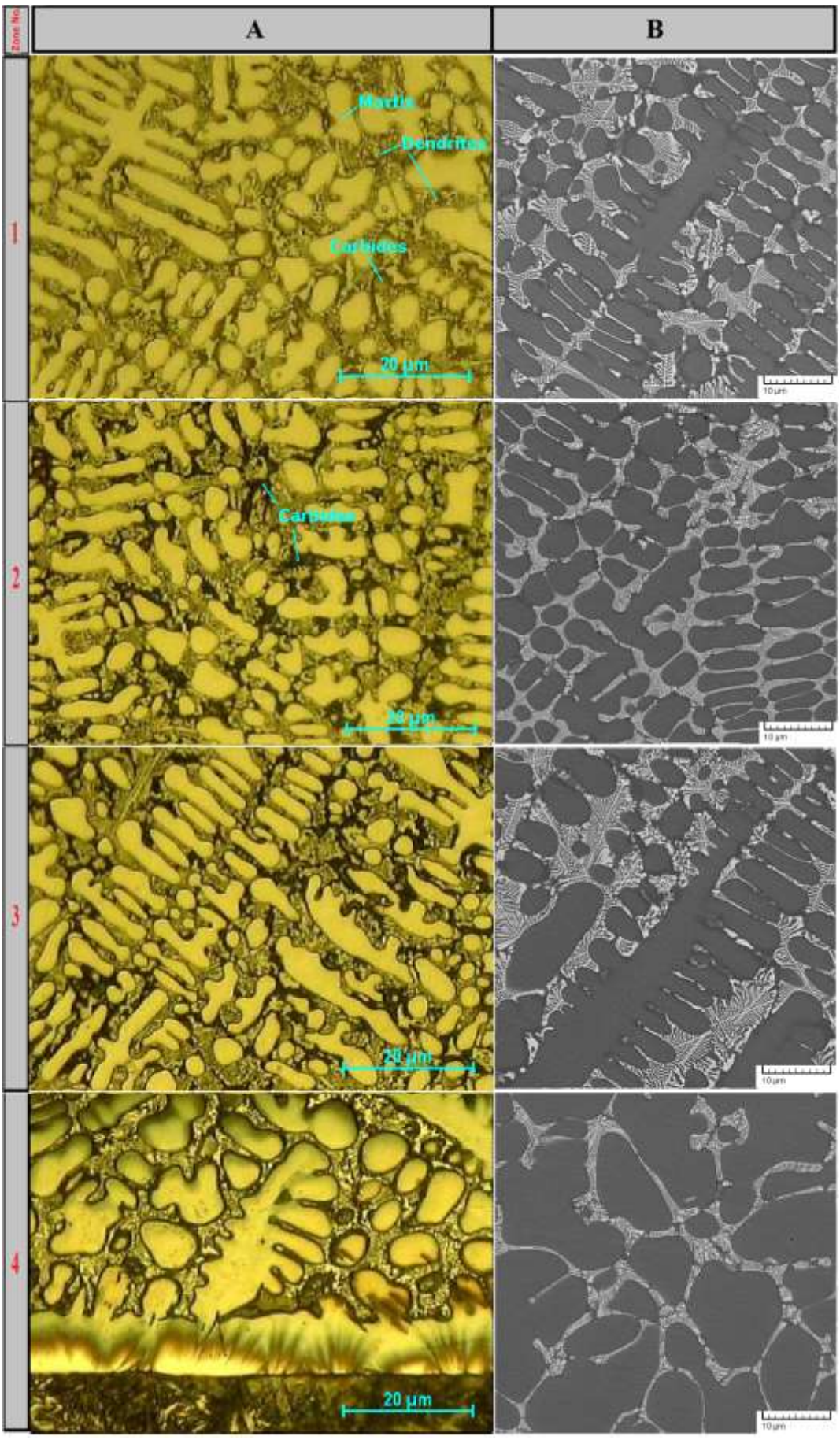

Figure (4.27): Microstructures of the C5 sample in the different zones at higher magnifications using an (A): OM and (B): SEM.

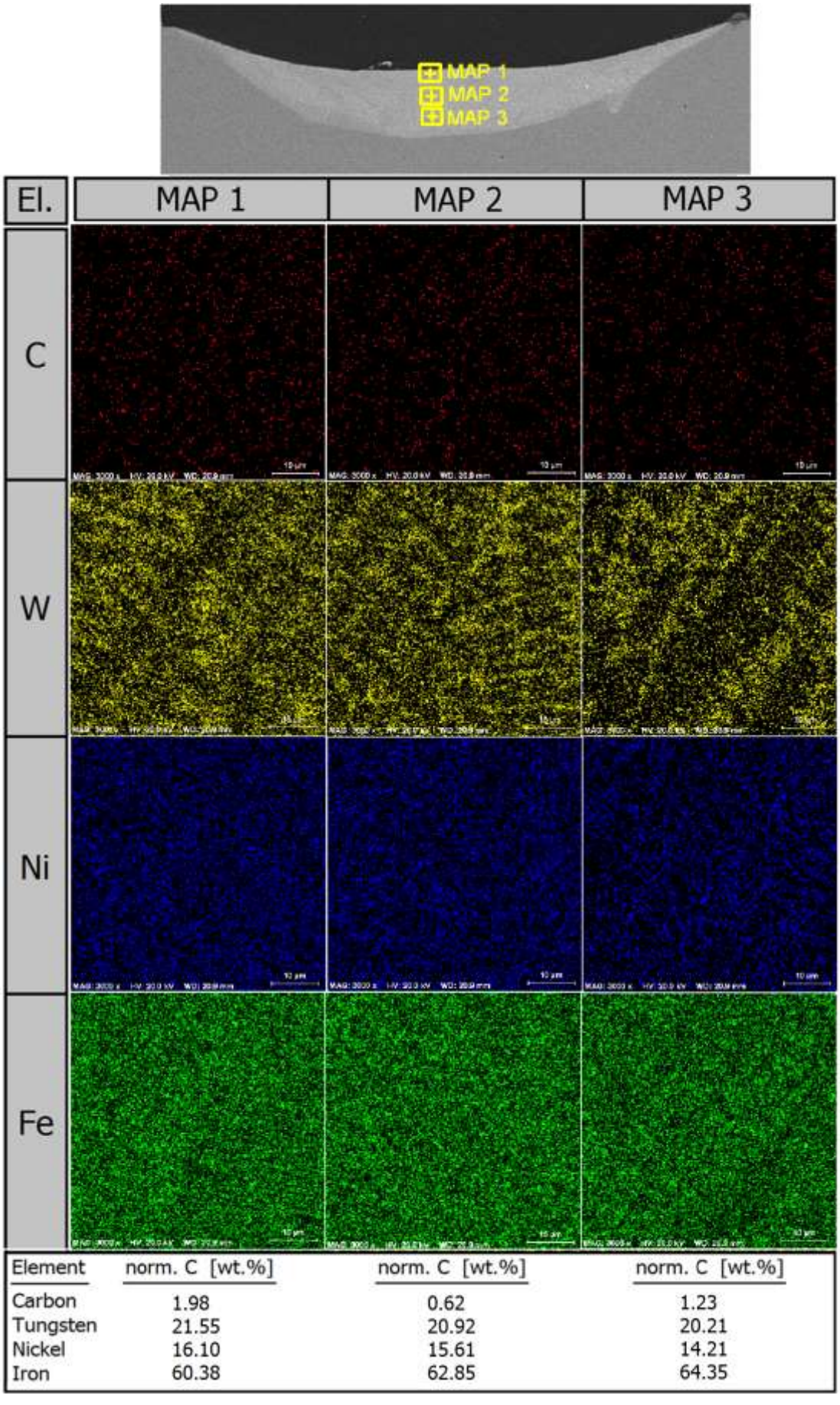

Element	norm. C [wt.%]	norm. C [wt.%]	norm. C [wt.%]
Carbon	1.98	0.62	1.23
Tungsten	21.55	20.92	20.21
Nickel	16.10	15.61	14.21
Iron	60.38	62.85	64.35

Figure (4.28): The EDS map of the C5 sample at different depths along the cross section of the clad layer.

4.3.2 The Effect of Cladding Current Values

With the carbide-nickel composite coatings produced by the TIG cladding technique, the current intensity and as a result the heat input have typically significant effects on the microstructure [75].

By comparing with the C5 sample, C6 was coated with the same pre-placed composite paste (70% WC-Ni), but with the cladding current intensity increased to 130A. Figure (4.29) shows the microstructural map of the C6 sample at different depths along the centerline of the clad layer cross section using the OM and SEM. It is clearly observed that the structure is generally composed of coarser dendrites, and the columnar dendrites are less than those appeared in the C5 clad layer. The reason behind this might be that increasing the TIG cladding current value definitely increases the heat input which in turn reduces the cooling rates experienced by the molten pool. It is well known that low cooling rates allow the grains to grow considerably due to the longer solidification time and thus coarsening the grain structure. This is consistent with Tosun [66] who demonstrated that with the increase of the cladding current intensity (power input), and due to the resulting lower cooling rates, the composite needle-like Ni/WC alloy transforms into a spherical-shaped granular structure. Figure (4.30) shows the optical and scanning electron microstructures of the C6 sample in the different zones at higher magnifications, where the tungsten carbides distributed through the matrix are very evident. This indicates that the increase in the cladding current value to 130A did not lead to decomposition of the tungsten carbide. The figure also showed in Zone 4 that the dilution with the substrate was higher due to the higher current value used with this sample.

The EDS map along the centerline of the C6 cross section shows in Figure (4.31) that the content of each element was highly comparable at the three test points with averages of 56.4% Fe, 13.5% Ni, 28.4% W and 1.7% C.

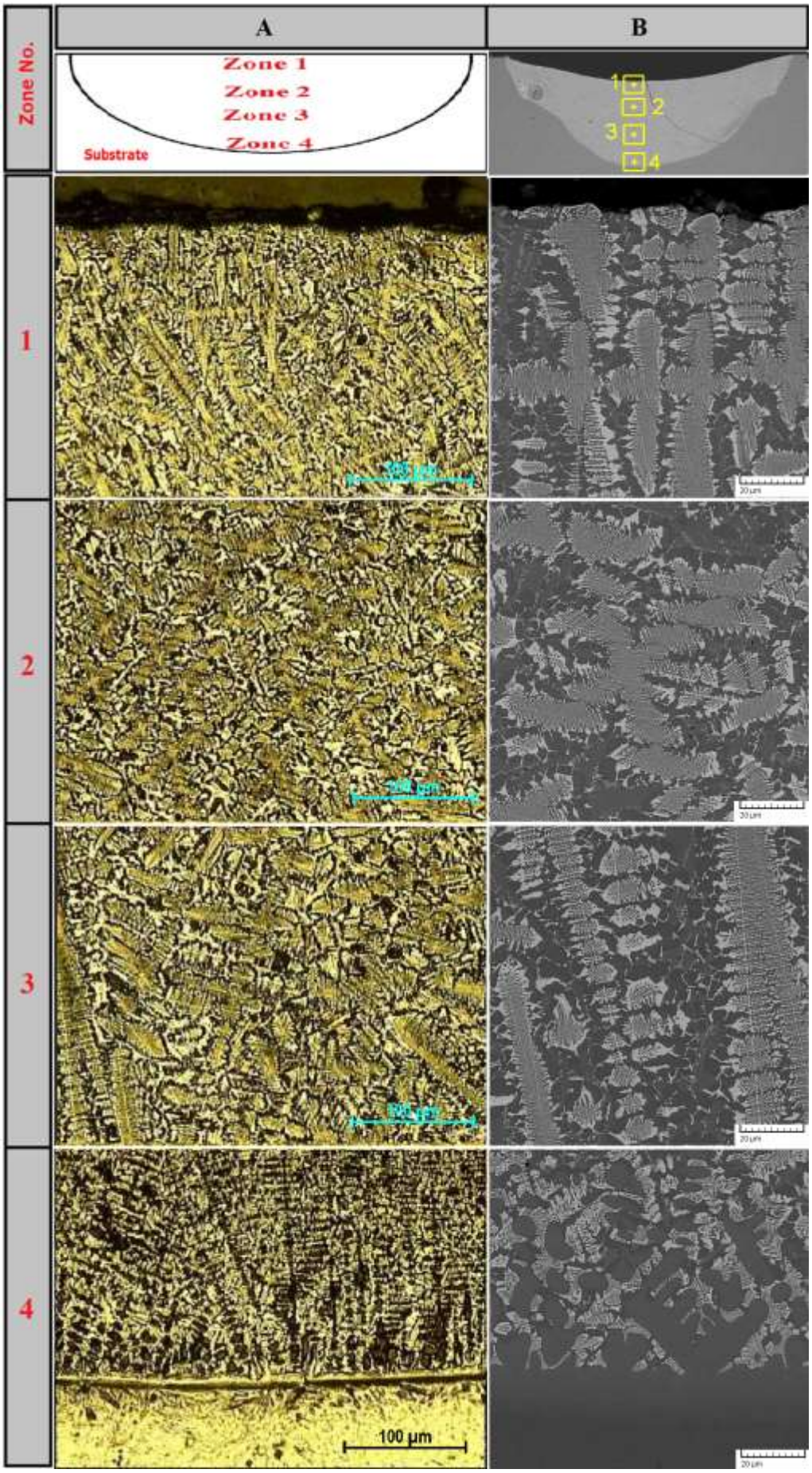

Figure (4.29): Microstructural map of the C6 sample at different depths along the centerline of the cross section of the clad layer using an (A): OM and (B): SEM.

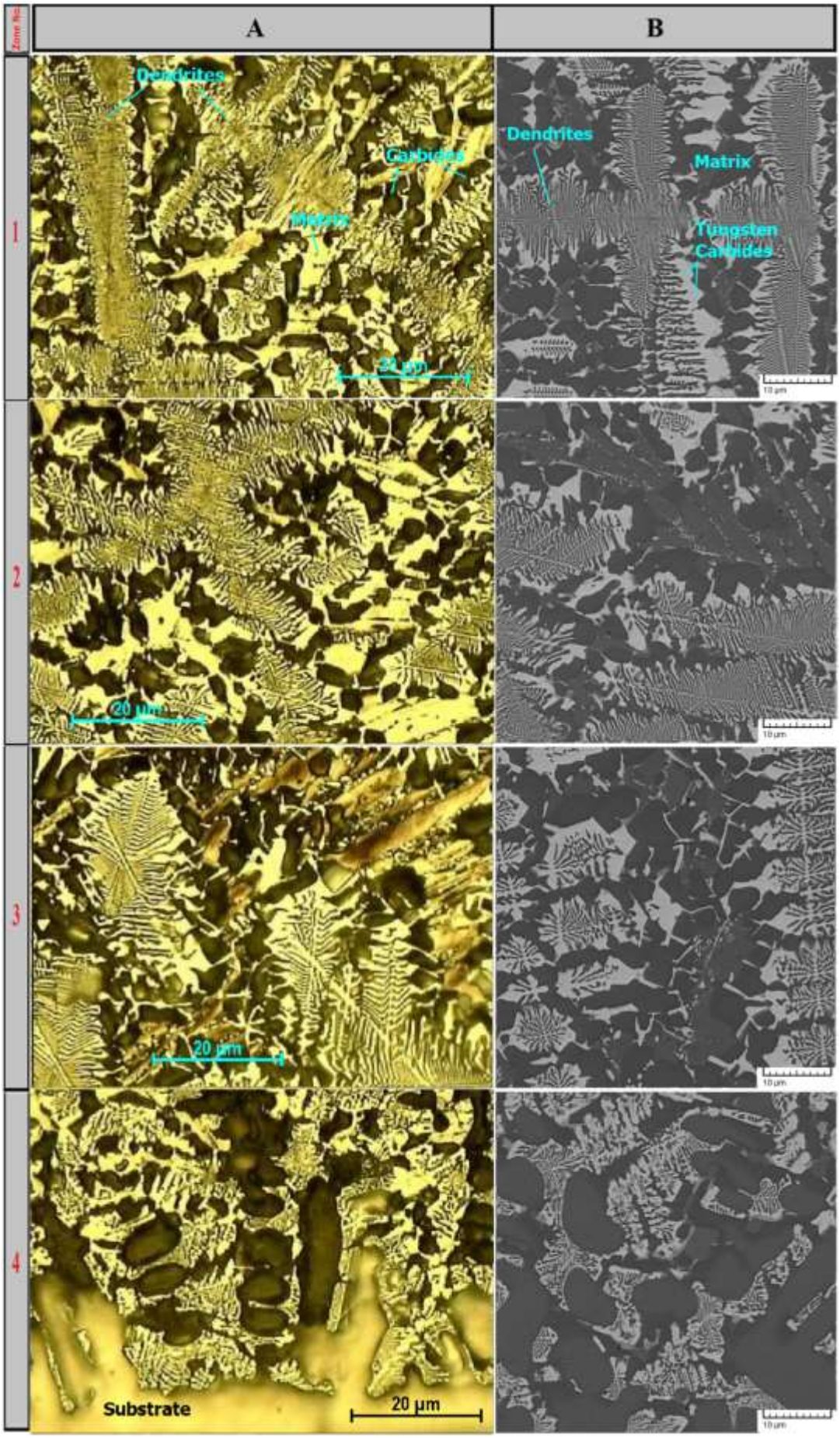

Figure (4.30): Microstructures of the C6 sample in the different zones at higher magnifications using an (A): OM and (B): SEM.

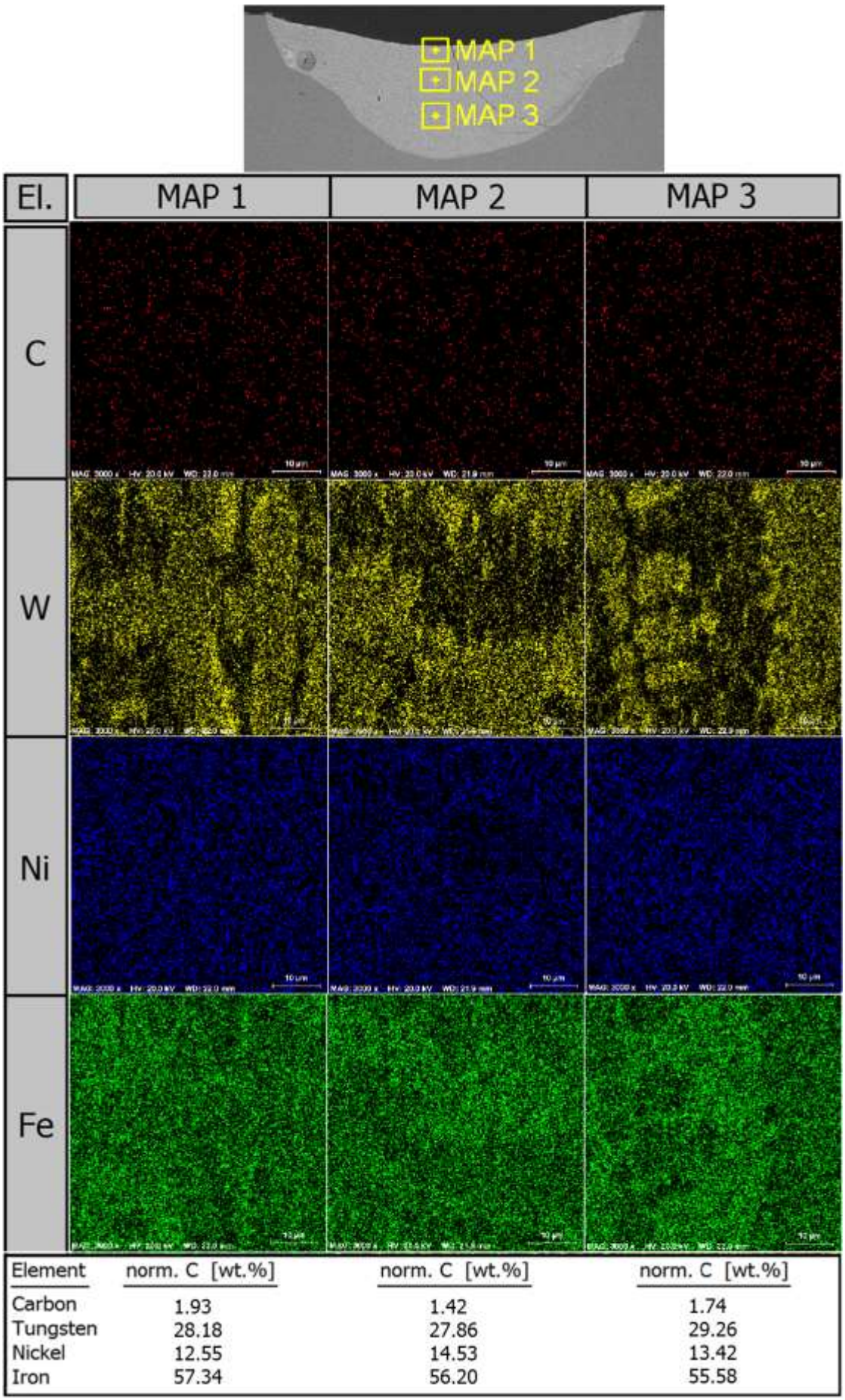

Element	norm. C [wt.%]	norm. C [wt.%]	norm. C [wt.%]
Carbon	1.93	1.42	1.74
Tungsten	28.18	27.86	29.26
Nickel	12.55	14.53	13.42
Iron	57.34	56.20	55.58

Figure (4.31): The EDS map of the C6 sample at different depths along the cross section of the clad layer.

It is evident from Figure (4.31) that the average iron content is still predominant at the expense of other elements due to the effect of dilution with the substrate material (low alloy steel). The figure shows that the distribution of the Fe element at the three test points refers to the matrix locations shown in Figure (4.30) by the SEM, indicating that the iron element is mainly concentrated in the matrix rather than the dendrites. It is also noted that the distribution of the W element at the three test points in Figure (4.31) clearly refers to the locations and orientations of the dendrites in addition to the locations of WC shown by the SEM in Figure (4.30). However, the distribution of carbon and nickel elements appears to be more homogeneous through the microstructures of the clad layers.

The effect of increasing the current value to 140A on the microstructures of the clad layer (C7) at all four zones is shown in Figures (4.32 and 4.33) using OM and SEM. The figures exhibit a very distinct heterogeneity in the microstructures of the four zones. The microscopy for Zone 1 showed densely branched dendrites of nickel solid solution with tungsten carbides segregated at the dendrite boundaries due to the growth of the dendrite branches, which all are distributed through the matrix. In Zone 2, the matrix proportion increased at the expense of dendrites which decreased significantly in Zone 3 with a major predominance of the matrix and tungsten carbides. Increasing the fraction of the matrix and tungsten carbides necessarily reduces the dendrites proportion in the structure. The reason behind this could be that the decrease in cooling rates experienced by the molten pool due to the increased amount of heat being introduced into this sample may provide enough time for the WC particles to sink towards the bottom due to their relatively high density [66]. In addition to the matrix and tungsten carbides, the microscopy for Zone 4 showed dendrites near the clad-substrate interface due to the higher cooling rate to which this region is exposed by the adjacent colder substrate material.

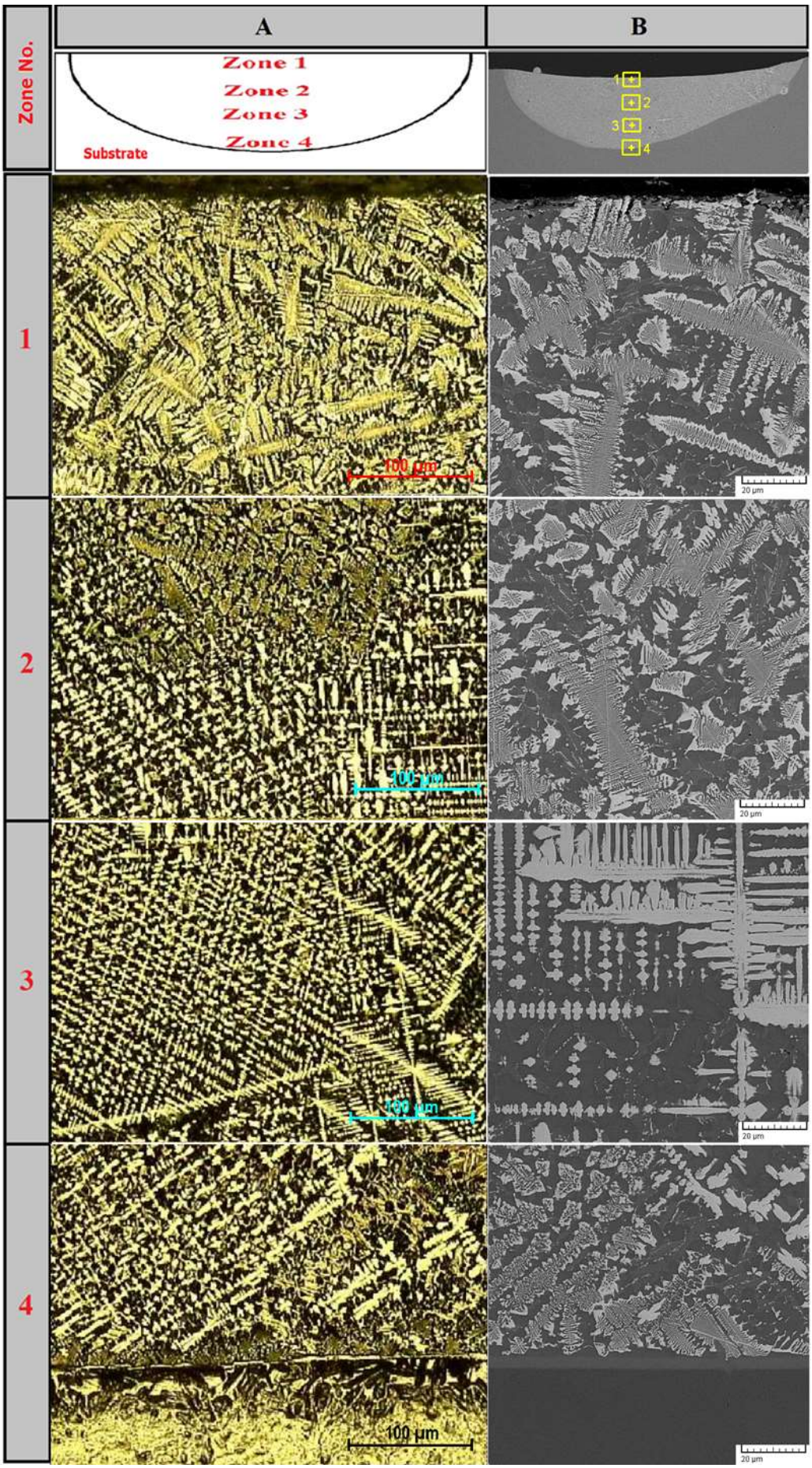

Figure (4.32): Microstructural map of the C7 sample at different depths along the centerline of the cross section of the clad layer using an (A): OM and (B): SEM.

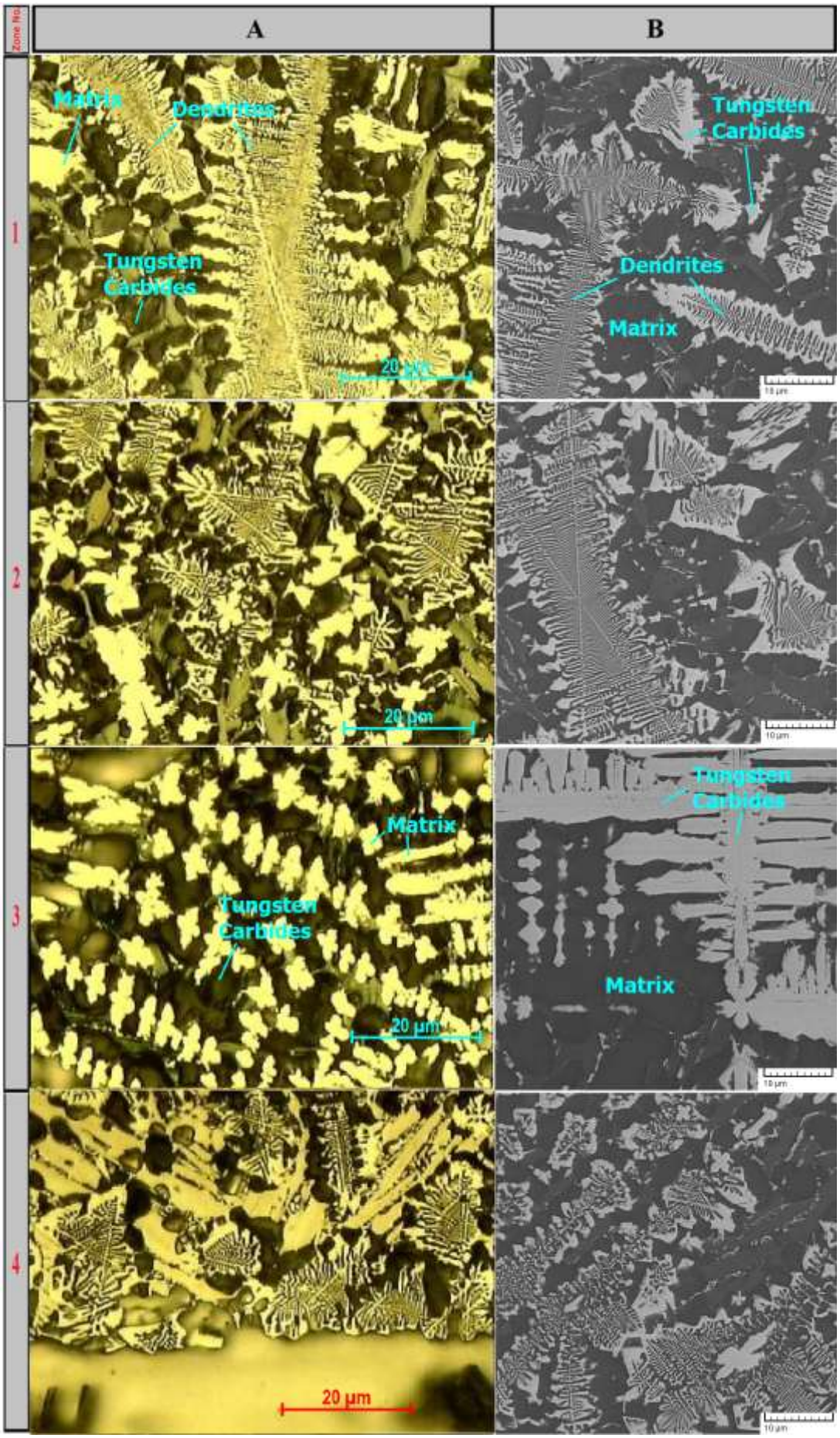

Figure (4.33): Microstructures of the C7 sample in the different zones at higher magnifications using an (A): OM and (B): SEM.

It is clearly observed that increasing the cladding current intensity to 140A was also not sufficient for the decomposition of the tungsten carbide. The EDS map along the centerline of the C7 cross section shows in Figure (4.34) that the content of each element has noticeably varied at the three test points with averages of 51.5% Fe, 15.0% Ni, 32.3% W and 1.3% C. This variation was due to the distinct heterogeneity in the microstructures of the different zones shown in Figures (4.32 and 4.33). It is clear that the average iron content is still more than half of the total constituents of the clad layer due to the effect of dilution with the substrate material. Figure (4.34) shows more clearly that the distribution of the Fe element at the three test points refers to the matrix locations shown in Figure (4.33) by the SEM, which indicates that the iron element is mainly concentrated in the matrix rather than the dendrites. The figure also reveals that the distribution of the W element at the three test points refers more clearly to the locations and orientations of the dendrites in addition to the locations of tungsten carbides shown by the SEM in Figure (4.33). The distribution of the Ni element has decreased while moving from point 1 towards point 3 due to the main predominance of the matrix and tungsten carbides at the expense of nickel solid solution dendrites.

The effect of decreasing the TIG cladding current intensity to 80A on the microstructure of the clad layer (C8 sample) has also been investigated. The macroscopic examination of this sample showed in Figure (4.2) a destroyed coating layer, especially in the middle, due to poor fusion as a result of the insufficient current value used. For the same reason, the C8 sample showed relatively unsuitable interfacial bonding with the substrate. Therefore, a region on the right side of the remaining coating layer shown in Figure (4.2), which contains fewer defects and has some interfacial bonding with the substrate was chosen to investigate the microstructure. Figure (4.35) shows the selected region with the zones under study.

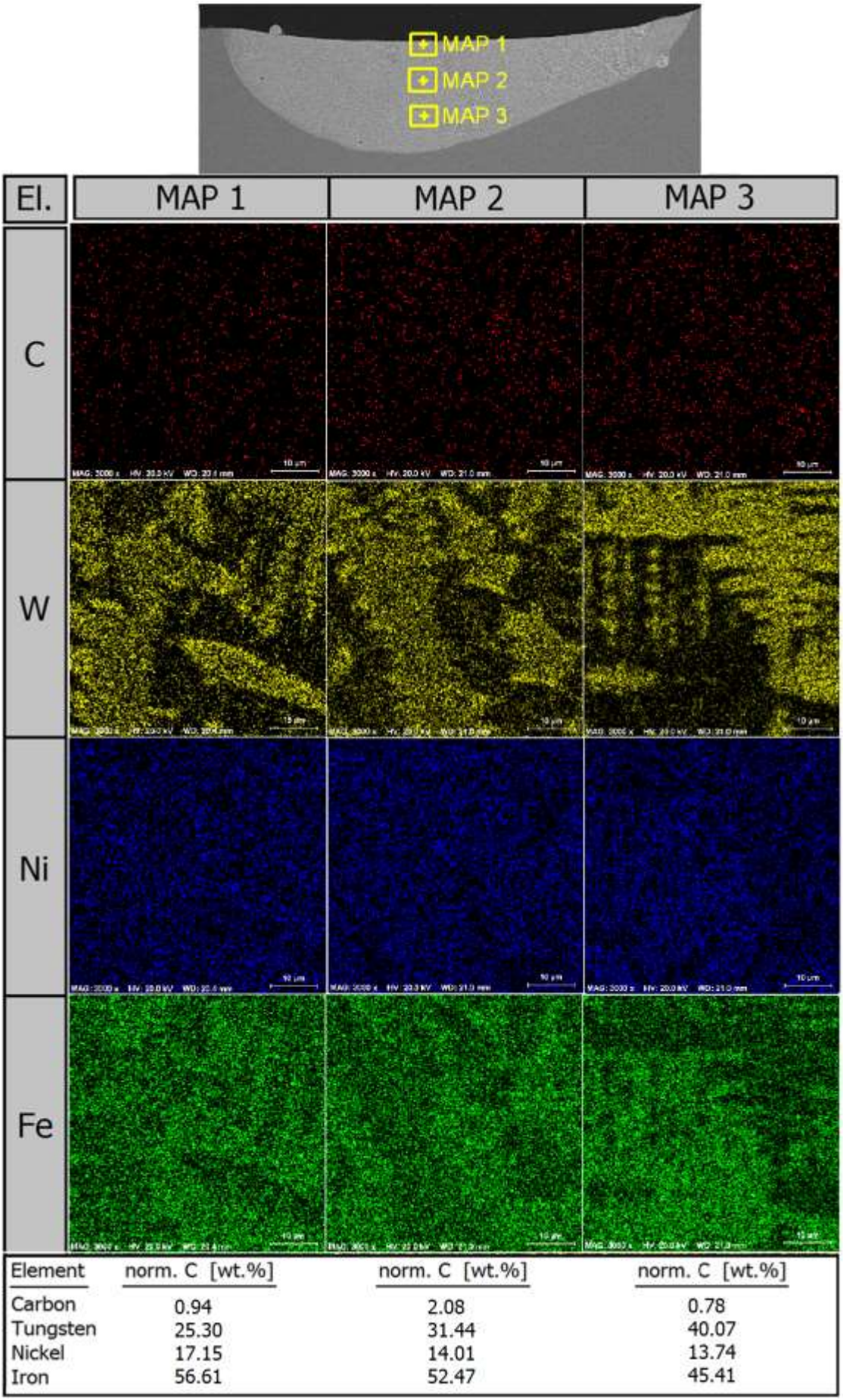

Element	norm. C [wt.%]	norm. C [wt.%]	norm. C [wt.%]
Carbon	0.94	2.08	0.78
Tungsten	25.30	31.44	40.07
Nickel	17.15	14.01	13.74
Iron	56.61	52.47	45.41

Figure (4.34): The EDS map of the C7 sample at different depths along the cross section of the clad layer.

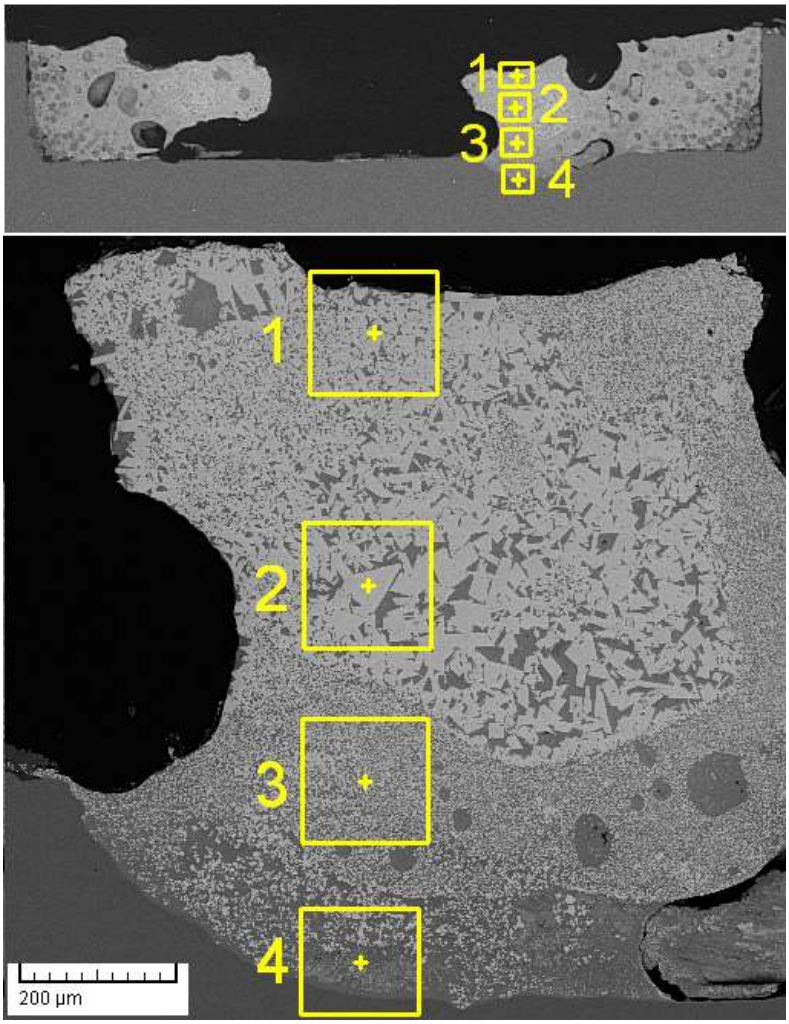

Figure (4.35): Scanning electron microstructure of the selected region under study of the C8 sample at different depths along the cross section of the clad layer.

The microstructural map of this sample showed in Figures (4.36 and 4.37) that the structures of Zones 1, 2 and 3 mainly consist of different particle sized tungsten carbides distributed through a molten Ni-based matrix. The carbide particles were polygonal shaped and intact without decomposition due to the insufficient cladding current value used. The figures also showed that the microstructure of Zone 4, in addition to the WC particles, consists of dendrites of nickel solid solution with iron picked-up from the substrate material. The cooling rate of this sample is higher due to the lower heat input to the substrate as a result of using a lower current value. Figure (4.38) shows the EDS map of the C8 cross section.

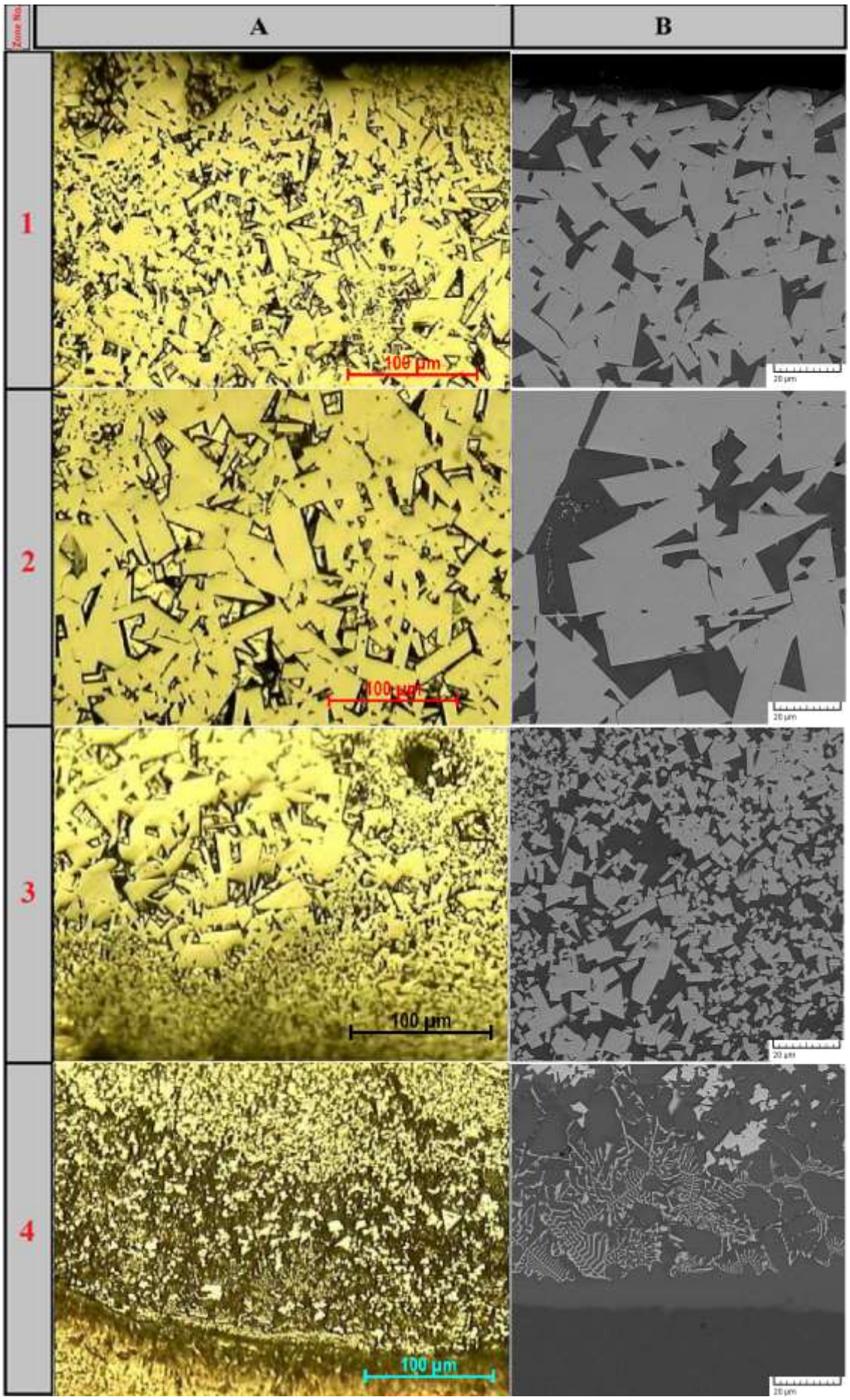

Figure (4.36): Microstructural map of the C8 sample at different depths along the cross section of the clad layer using an (A): OM and (B): SEM.

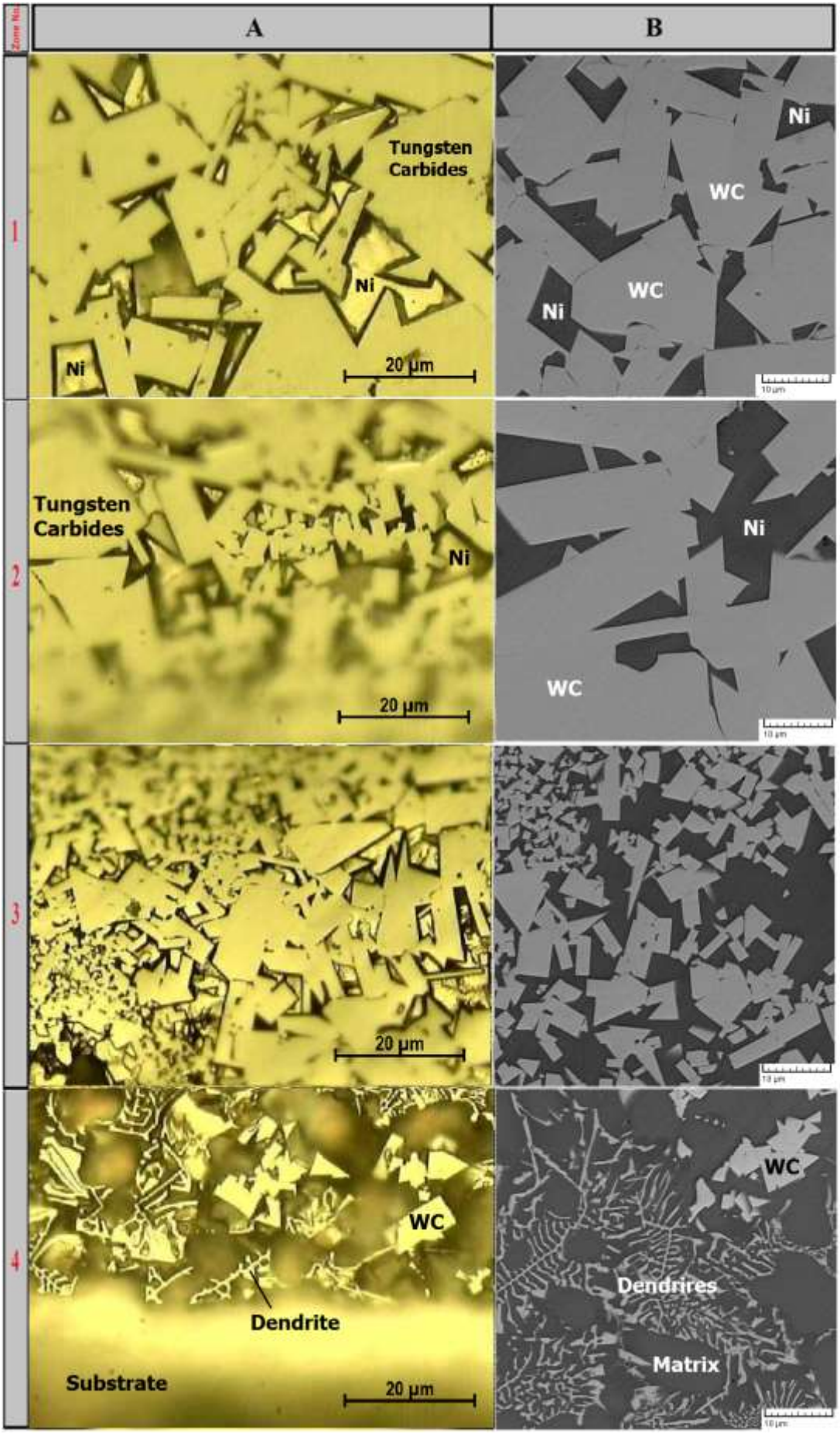

Figure (4.37): Microstructures of the C8 sample in the different zones at higher magnifications using an (A): OM and (B): SEM.

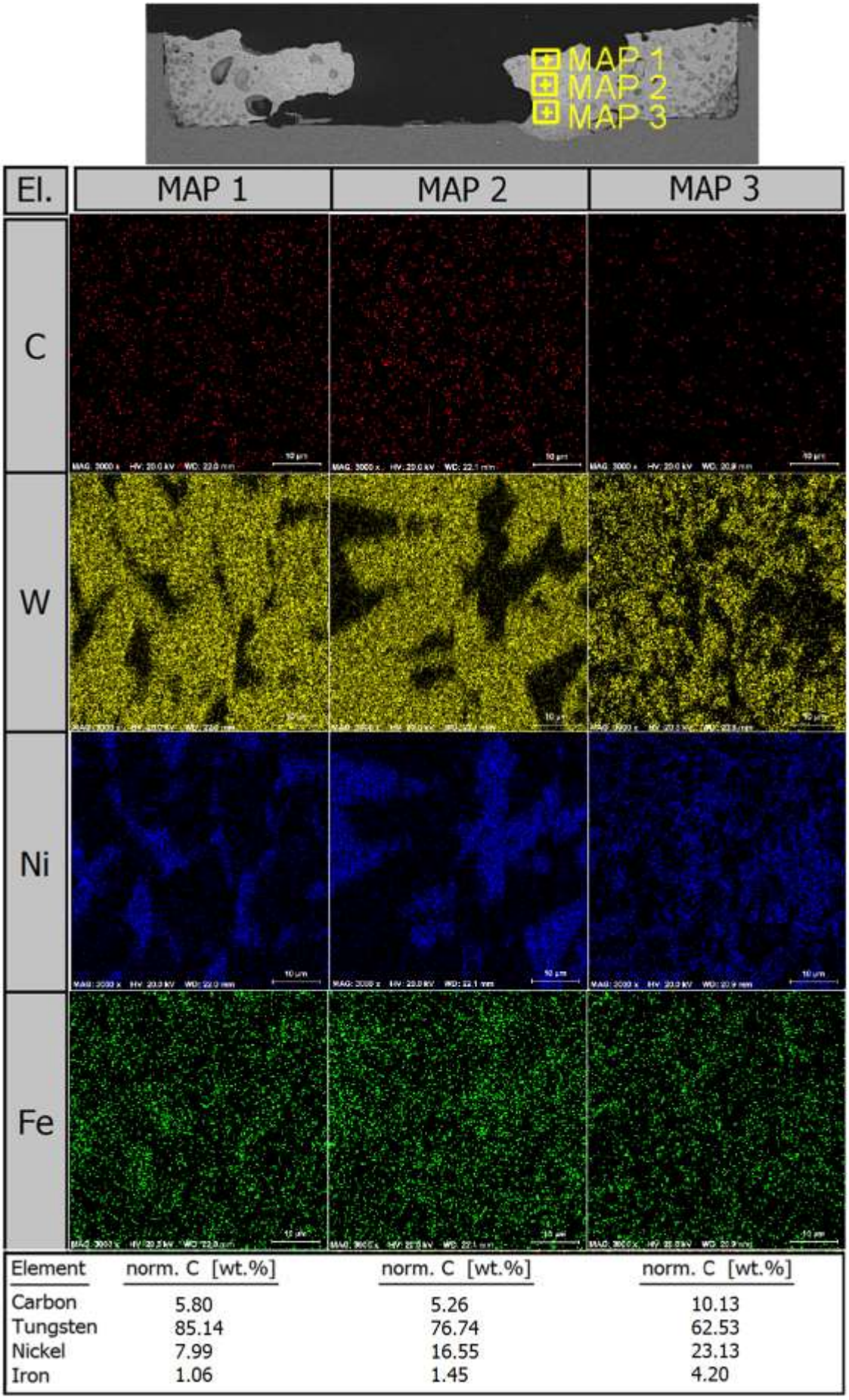

Element	norm. C [wt.%]	norm. C [wt.%]	norm. C [wt.%]
Carbon	5.80	5.26	10.13
Tungsten	85.14	76.74	62.53
Nickel	7.99	16.55	23.13
Iron	1.06	1.45	4.20

Figure (4.38): The EDS map of the C8 sample at different depths along the cross section of the clad layer.

It is clearly observed from the figure that the content of each element has also noticeably varied at the three test points with averages of 2.2% Fe, 15.9% Ni, 74.8% W and 7.1% C. This variation was accompanied by the heterogeneity in the microstructures of the different zones shown in Figures (4.35, 4.36 and 4.37). The average tungsten content is about three-quarters of the total constituents of the clad layer because the microstructure of the different zones consisted mainly of WC particles. The distribution of the W element at the three test points indicates clearly the shapes, sizes and locations of tungsten carbides shown by the SEM in Figure (4.37). While moving from point 1 towards point 3, the decrease in W content was associated with an increase in Ni content. The distribution of the Ni element clearly refers to the Ni-based matrix shown by the SEM in Figure (4.37). The average iron content for the three test points is only about 2.2% of the total constituents of the clad layer, which proves that the dilution that occurred with the substrate material was very little. This is due to poor fusion as a result of the insufficient TIG cladding current value used with this sample, which resulted in poor bonding between the clad layer and the substrate. Figure (4.38) however shows that the distribution of the Fe element at the three test points refers to the Ni-based matrix locations shown in Figure (4.37) by the SEM.

To verify the phases and compounds that make up the coating layers, an X-ray diffraction (XRD) test was conducted for one sample, which is C3. Analysis of the XRD graph (Figure 4.39) with the help of analytical cards (Appendix A) explored different constituents: WC, (Fe,Ni) and Fe_3C. Fe,Ni refers to nickel solid solution dendrites, Fe_3C denotes the matrix, while WC indicates the tungsten carbides distributed through the matrix. It is clearly noted that the XRD analysis has achieved an appropriate matching with the results of microscopy.

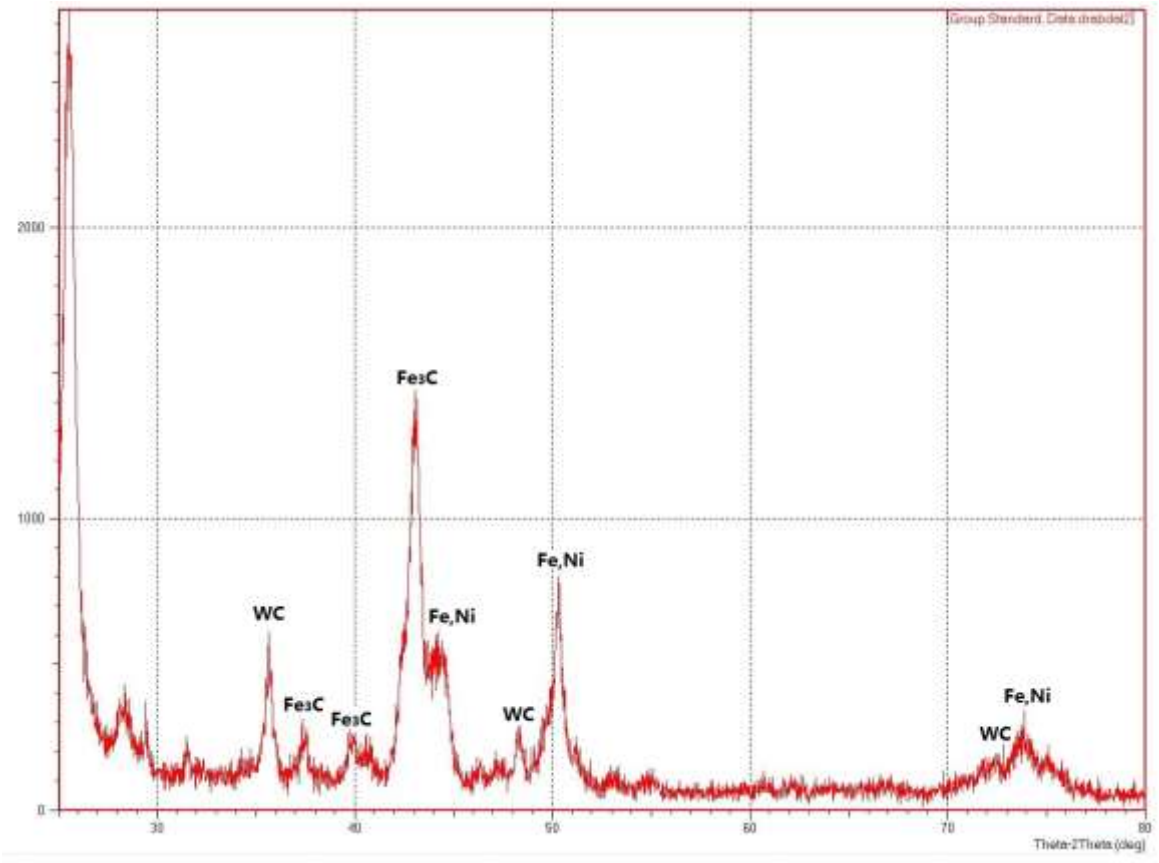

Figure (4.39): XRD graph of the surface of the C3 clad layer sample.

4.4 Micro-hardness Test

As a result of a series of microstructural variations across the clad layers, the hardness was expected to vary as well. Hardness test is the easiest way to evaluate the performance of a clad layer. It is also important as a way to differentiate the different clad layers. Figure (4.39) shows the locations of hardness measurement points distributed at different depths along the centerline of the cross section of the clad layers. Table (4.1) presents the average Vickers micro-hardness values at these locations.

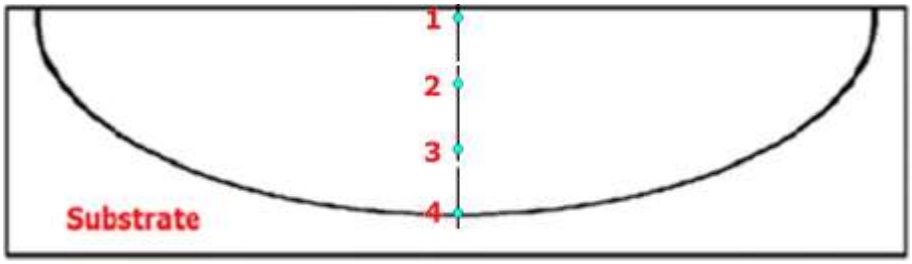

Figure (4.40): Locations of the hardness measurement points at different depths along the centerline of the cross section of the clad layers.

Table (4.1): Average Vickers micro-hardness values at locations shown in Figure (4.39).

Point locations / Sample	1	2	3	4	Average
C1	805.1	232	222.4	249.8	377.3
C2	456.3	782.65	549.35	516.8	576.3
C3	655.55	669.8	755.45	727.87	702.2
C4	422.67	759.84	751.1	1091.29	756.2
C5	556.7	621.8	642.85	414.3	558.9
C6	649.95	522.2	782.6	658.1	653.2
C7	549	745	554.6	403.55	563.0
C8	752.55	892.95	928.55	826.2	850.1

The average hardness value of the last three points (2, 3 and 4) shown in table (4.1) of the C1 sample is about 235HV, which is lower than that of the substrate material (264.5HV). This is because the microstructure at these three points was mostly nickel solid solution grains with a small amount of WC particles distributed through the matrix (Figure 4.7). This could be attributed to the fact that the pre-placed composite of this sample was 30% WC-Ni. On the other hand, the microstructure of the substrate material (low alloy steel) was mostly pearlite as shown in Figure (4.3). The pearlitic structure typically introduces a relatively higher hardness. The 1st point hardness value of the C1 sample (805.1HV) was notably large due to the presence of a dense acicular WC within the matrix there (Figure 4.6). In contrast to the C1 sample, Table (4.1) shows that the hardness values at all measurement points for all other samples were much higher than that of the substrate. This is due to the increased wt.% of hard tungsten carbide in the pre-placed composite paste of these samples. This is consistent with the results obtained by Tosun in 2014 [66], which showed a great improvement in the hardness of the WC-reinforced coating produced by TIG cladding compared to the substrate material (AISI 1010 steel). Figure (4.40) shows the effect of the WC wt.% in the clad layers on the average Vickers micro-hardness of these layers deposited with a TIG cladding current of 120A.

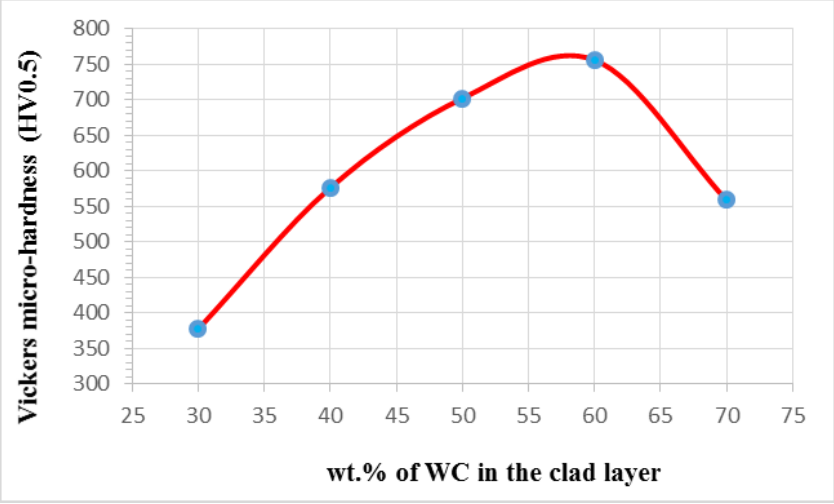

Figure (4.41): The relationship between Vickers micro-hardness and the WC wt.% in the clad layers deposited with a TIG cladding current of 120A.

In general, the hardness across the clad layer and thus the average hardness value of the C2 sample is notably higher than that of the C1 sample. This is due to the notable increase in dendrites in microstructures of this sample compared to those scoped in the C1 sample (Figure 4.12). The hardness value at point 2 of the C2 sample (782.65HV) was much higher than that at point 1 (456.3HV), because the density of dendrites slightly increased, and therefore, the microstructure in this region appeared somewhat finer (Figure 4.12). Refining the grain structure largely improves hardness [83]. The hardness at point 3 of the same sample decreased to (549.35HV) because the dendrites formed in this region were mostly columnar as shown in Figures (4.12 and 4.15). It is well known that hardness decreases with increasing grain size [83]. Consequently, the hardness at point 4 was relatively lower (516.8HV) because both OM and SEM showed that the columnar dendrites there were more dominant (Figures 4.12 and 4.16).

Vickers micro-hardness across the clad layer and therefore the average hardness value of the C3 sample is markedly higher than that of the C2 layer. This is because the microstructures at the different zones along the cross section of the C3 sample were notably finer, and thus the proportion of dendrites was much more than those at the corresponding zones of the C2 sample, as shown in Figure (4.18). The hardness value at point 3 was (755.45HV) the highest across this clad layer. This could be attributed to two reasons, the first being the presence of dendrites with dense branches (Figure 4.20A), and the second reason being the relatively large size of WC particles that remained intact, without decomposition distributed through the matrix of this region (Figure 4.20B).

The average hardness value across the C4 sample increased to (756.2HV). This is because the increase in the wt.% of WC in the composite of this sample to 60% clearly enhanced the proportion of dendrites; the dendrites were also more densely branched (Figure 4.23) compared to the C3 sample.

In addition, as in the C3 layer, some relatively large WC particles appeared distributed through the matrix. In general, the notable increase in hardness across this sample could be attributed to the apparent increase in densely branched dendrites and carbides at the expense of the matrix (Figure 4.24).

Figure (4.40) and Table (4.1) show that the average hardness value across the C5 sample decreased to (558.9HV) as a result of increasing the wt.% of WC in the composite of this sample to 70% at the expense of nickel. Although the microstructure of the dendrites formed in this clad layer was finer (Figure 4.26) than what appeared in C4, the dendrites were mostly columnar. Another reason for this decrease in hardness is the relative increase in matrix ratio in this sample compared to that observed in the C4 sample. The findings for the average Vickers micro-hardness and its relationship to the wt.% of WC in the clad layers were somewhat similar to those revealed in 2016 by Shu et al. [54], using laser cladding, where the higher micro-hardness value of the prepared coatings was up to 755HV_2.

With the carbide-nickel composite coatings produced by the TIG cladding technique, the arc current has noticeable effects on hardness [75]. Figure (4.41) shows the effect of the TIG cladding current value on the average Vickers micro-hardness of the coatings deposited with 70wt.% WC-Ni.

Figure (4.42): The relationship between the average Vickers micro-hardness and the TIG cladding current value for the samples coated with 70wt.% WC-Ni.

It is well known that higher cladding current values increase the heat input and thus reduce the cooling rates to which the molten pool is subjected. Lower cooling rates largely coarsen the grain structure and accordingly reduce the hardness [83]. Therefore, the hardness was expected to decrease with increasing cladding current value due to the coarsening of the grain structures. On the contrary, the average micro-hardness value of the C6 sample increased to (653.2HV) when the cladding current intensity was increased to 130A for the same pre-applied composite paste (70% WC-Ni). This is in agreement with what Tosun found in 2014 [66]. The reason for this unexpected increase in hardness might be that the columnar dendrites in the microstructure of this coating (Figure 4.29) were less than those appeared in the C5 clad layer. Lower cooling rates decrease the proportion of the columnar dendrites. The diversity in the microstructure across the C7 sample as a result of increasing the current value to 140A was reflected in the hardness across this sample with an average of (563HV).

Heterogeneity in the microstructure can lead to inaccurate hardness results, as the indenter of the hardness measuring device may fall on a region densely packed with carbide, giving a higher hardness reading, or it may fall on a matrix, leading to a much lower hardness value.

On the other hand, decreasing the TIG cladding current intensity to 80A significantly increased the average hardness across the C8 sample. The reason behind this remarkable increase in hardness is that the microstructure across this coating layer mainly consists of different particle sized tungsten carbides distributed through a molten Ni-based matrix as in Figures (4.36 and 4.37). The carbide particles were polygonal shaped and intact without decomposition due to the insufficient cladding current value used. The EDS map across this sample showed that the average tungsten content is about three-quarters of the total constituents of the clad layer.

However, this sample showed a destroyed coating layer and fairly unsuitable interfacial bonding with the substrate due to poor fusion as a result of the insufficient cladding current value used.

4.5 Wear Test

Table (4.2) exhibits the weight lost at each sliding distance travelled and the weight loss rate (per meter) of the coating layers, which show different increases in the weight lost with the different distances travelled. It is clearly observed from the table that the rate of weight loss in the C2 sample (1.18×10^{-4}g/m) was greater than that in the C1 (9.08×10^{-5}g/m). This might be attributed to the presence of a dense WC within the matrix at the upper regions of the C1 layer (Figures 4.4-4.6). It is well known that the presence of hard carbide particles (such as tungsten carbide) in a particular region reduces the weight loss (wear rate), and thus increase the wear resistance in that region. Therefore, after passing the upper regions, down to the lower regions of this layer, the weight lost per meter became much more, due to the lower hardness there (points 2, 3 and 4 in Table 4.1).

Table (4.2): Weight lost for samples at each travelled distance.

Sample	Weight lost (g) at distance (m)					Weight loss rate of the sample (g/m)
	600	1200	1800	2400	3000	
C1	0.0298	0.0788	0.1504	0.2179	*	9.08×10^{-5}
C2	0.0667	0.1391	0.2149	0.2829	*	1.18×10^{-4}
C3	0.0481	0.1022	0.1528	0.1813	0.2059	6.86×10^{-5}
C4	0.0201	0.0468	0.0698	0.0918	0.1015	3.38×10^{-5}
C5	0.0244	0.0307	0.0327	0.0330	0.0336	1.12×10^{-5}
C6	0.0110	0.0206	0.0223	0.0254	0.0285	9.50×10^{-6}
C7	0.0041	0.0085	0.0125	0.0172	0.0192	6.40×10^{-6}
C8	0.0040	0.0052	0.0065	0.0074	0.0085	2.83×10^{-6}

* Due to dimensional limited of sample, continuing the test was not possible.

However, due to the limited thickness, or in other words, the consumption of the coated layer, it was not possible to continue the wear test on the C1 and C2 samples beyond the sliding distance of 2400m.

Increasing the wt. of WC to 50% and 60% in the C3 and C4 samples decreased the weight loss rate to 6.86×10^{-5} and 3.38×10^{-5}g/m respectively. This decrease was associated with increasing the average hardness across these samples. Although the average hardness decreased across the C5, this sample introduced a decrease in the rate of weight loss to 1.12×10^{-5}g/m. This indicates that an increase in hardness in a region is not necessarily associated with a decreased rate of weight loss during wear in that region. Increasing the wt.% of WC in the coating layers generally presented a lower rate of weight loss and thus an increase in wear resistance.

It is evident from Table (4.2) and Figure (4.42) that the weight loss mostly decreases while increasing the sliding distance. The reason behind this could be the accumulation of dislocations and the formation of cold work in the layers below the abrasive surface [91,93]. This indicates that the increase in the wt.% of WC reinforcement particles was not so excessive that it reduces the amount of matrix phases between these particles to such an extent that the carbide particles come into contact with each other. This could reduce the supportive effects of the WC particles in decreasing wear rates, and in some cases increases the wear rate as well [94,95].

Figure (4.43) shows the effect of the TIG cladding current intensity on the weight lost at the different sliding distance travelled. Increasing the current value to 130A and 140A for the same pre-applied composite paste (70% WC-Ni) of the C5 sample decreases the weight loss rate and thus the wear rate of the C6 and C7 samples to 9.50×10^{-6} and 6.40×10^{-6}g/m respectively. These decreases were associated with the increased hardness across the coating layers of these samples. Similarly, the significant increase in hardness across the C8 sample was reflected as a remarkable decrease in

the rate of weight loss as a result of decreasing the TIG cladding current intensity to 80A. The reason behind the notable increase in wear resistance of this sample is the major presence of tungsten carbides with various particle sizes distributed through a molten Ni-based matrix (Figures 4.36 and 4.37). As mentioned earlier, the average hard tungsten content was about three-quarters of the total constituents of the clad layer.

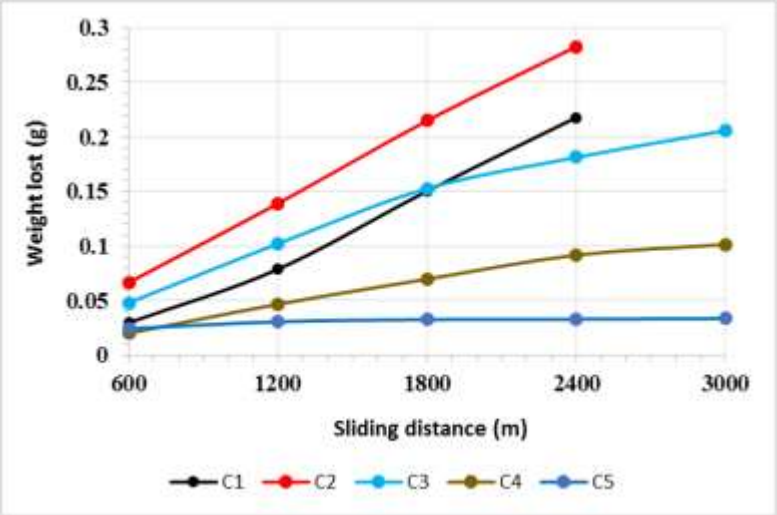

Figure (4.43): The effect of increasing the wt.% of WC in the clad layers deposited with a TIG cladding current of 120A on the weight lost at the different sliding distances.

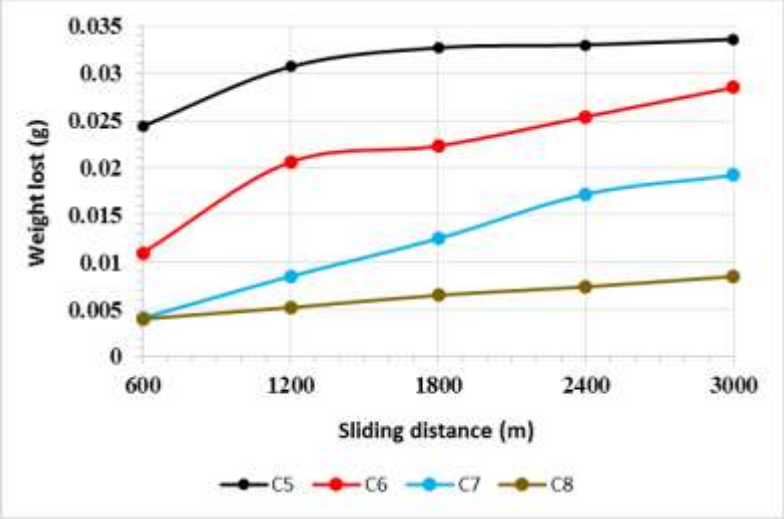

Figure (4.44): The effect of the TIG cladding current intensity on the weight lost at the different travelled sliding distance of the (70% WC-Ni) clad layers.

CHAPTER FIVE:

CONCLUSIONS &

RECOMMENDATIONS

CHAPTER FIVE: CONCLUSIONS & RECOMMENDATIONS

5.1 Conclusions

This study explored the effect of using different wt.% of WC (30, 40, 50, 60 and 70) and various current values (80, 120, 130 and 140A) on WC-Ni composite coatings deposited on low alloy steel substrates using TIG cladding technique. The most important results of this study can be concluded as follows:

1. The microstructures of the clad layers were mainly composed of Ni solid solution dendrites with WC particles distributed through the matrix. Increasing the wt.% of WC at the same current value notably increased the proportion of the dendrites with finer and more densely branched.

2. Increasing the wt.% of WC showed across some clad layers densely branched columnar dendrites with a relatively large sized of WC particles which remained intact, without decomposition distributed through the matrix.

3. The bottom regions of clad layers showed tiny grains at the clad-substrate interface.

4. Increasing the current value introduced coarser dendrites and the columnar dendrites were less, while decreasing the current value to 80A resulted in microstructures of different particle sized tungsten carbides distributed through a molten Ni-based matrix.

5. The defective regions were tiny compared to the whole cross sections of the WC-Ni composite clad layers. Poor fusion and improper interfacial bonding clearly appeared in the clad layer resulting from using 70% WC-Ni and 80A.

6. The average hardness value across the clad layer resulting from the use of 30% WC-Ni and 120A, excluding that at the upper region, was lower than that of the substrate material (264.5HV). In contrast, the hardness values across all other clad layers were much higher than that of the substrate. The highest average hardness value was about 756HV for the clad layer deposited using 60% WC-Ni and 120A.

7. Increasing the current values for MMC increased the hardness to some extent, while the hardness notably increased to about 850HV with the current reduced to 80A.

8. Increasing the wt.% of WC and current value in the MMC generally presented a lower rate of weight loss and thus an increase in wear resistance.

5.2 Recommendations

Lessons learned from this study can be taken into consideration in studies on cladding, and some fields covered in this study could be further improved. The following is a summary of recommendations for further work.

1. Corrosion test can be carried out for the coating layers.

2. Laser cladding technique can be used with the clad layer compositions used in this study.

3. More wt.% of WC might be in pre-placed composite pastes.

4. Studying the effect of travel distance on the microstructure and properties of the clad layers.

5. Investigating the influence of particle size of pre-placed composite powders on the characteristics of the clad layers.

6. Cladding other substrate materials such as austenitic stainless steels.

References

1. Purohit R. K. (2005), *Material Science and Processes*, Scientific Publishers Journals Dept., INDIA.
2. Hashmi M. S. J. (2017), *Comprehensive Materials Finishing: Finish Machining and Net-shape Forming*, Vol 1, IRELAND.
3. Higgins R. A. and Bolton W. (2010), *Materials for Engineers and Technicians*, 5th ed. UK.
4. Talib H. M. (2020), *Investigating the Effect of Nickel Content on Low Alloy High Strength Steel Welds*, M.sc Dissertation, Metallurgical Engineering-Babylon University.
5. Rius-Ayra O. and Llorca-Isern N. (2021), *Surface Modification of Metals and Alloys*, MDPI, Spain.
6. Buytoz S. and Ulutan M. (2006), *In situ synthesis of SiC reinforced MMC surface on AISI 304 stainless steel by TIG surface alloying*, Surface and Coatings Technology, 200(12):3698-3704.
7. Viswanatthan R., Gandy D. and Coleman K., (2004), *Advances in Materials Technology for Fossil Power Plants*, ASM international, America.
8. Timings R. (2008), *Fabrication and Welding Engineering*, Elsevier Ltd, Hungary.
9. Branco R. and Berto F. (2017), *Mechanical Behavior of High Strength Low Alloy Steels*.
10. Totten G. E. (2006), *Steel heat treatment: metallurgy and technologies*, CRC press.
11. Steels L. A. (2001), *High-Strength Low-Alloy Steels*.
12. Tuttle R. (2018), *Alloy Steels*, 1st ed., Saginaw Valley State University, USA.
13. Avner S. H. (1974), *Introduction to physical metallurgy*, Vol. 2, pp. 481-497, New York: McGraw-Hill.
14. Tisza M. (2001), *Physical Metallurgy for Engineers*, ASM International and Freund Publishing House Ltd.
15. Sreeraj P., Kannan T. and Maji S. (2013), *Prediction and optimization of weld bead geometry in gas metal arc welding process using RSM and fmincon*, Journal of Mechanical Engineering, 5(8):154-165.
16. Eroğlu M. and Özdemir N. (2002), *Tungsten-inert gas surface alloying of a low carbon steel*, Surface and Coatings Technology, 154(2):209-217.
17. Buytoz S., Ulutan M. and Yildirim M. M. (2005), *Dry sliding wear behavior of TIG welding clad WC composite coatings*, Applied Surface Science, 252(5):1313-1323.
18. Dossett J. and Totten G. (2013), *Introduction to Surface Hardening of Steels*.
19. Grafen W. and Denhofer B. (2005), *New developments in thermo-chemical diffusion processes*, Surface and Coatings Technology. Vol. 200, pp. 1830-1836, Germany.

20. Davis J. R. and Associates (2002), *Surface Hardening of Steels*, ASM International Materials Park.
21. Zhong M. and Liu W. (2010), *Laser surface cladding: the state of the art and challenges. Proceedings of the Institution of Mechanical Engineers*, Part C: Journal of Mechanical Engineering Science, 224(5):1041-1060.
22. Ariely S., et al. (1993), *Laser surface alloying of steel with TiC, In 8th Meeting in Israel on Optical Engineering*, International Society for Optics and Photonics.
23. Thanigaivelan R., Rajan N. and Argul, T. G. (2022), *Advanced Manufacturing Techniques for Engineering and Engineered Materials*, India.
24. Womersley D. (2003), *Thermal Spraying and Powder Spray Welding Processes for the Hardfacing of Grey Cast Iron*, Materials & Design, Vol. 11, pp. 153-155, UK.
25. Toyserkani E., Khajepour A. and Corbin S. F. (2004), *Laser Cladding*, Canada.
26. Sagar A. and Purohit D. G. (2012), *Some Studies on MIG Hardfacing of Mild Steel Components*, International Journal of Engineering Research and Development, 4(8):42-56.
27. Madadi F., Ashrafizadeh F. and Shamanian M. (2012), *Optimization of pulsed TIG cladding process of stellite alloy on carbon steel using RSM*, Journal of Alloys and Compounds. 510(1):71-77.
28. Kou S. (2003), *Welding metallurgy*, 2nd ed. John Wiley & Sons, Inc., Hoboken, New Jersey.
29. Khan Md. I. (2007), *Welding Science and Technology*, New Age International (P) Ltd., Publishers, New Delhi.
30. Khanna O. P. (1980), *Welding Technology: A textbook for Engineering Students*, Dhanpat Rai and Sons, 1st ed, Delhi.
31. Air Products PLC (1999), *Welder's Handbook for Gas Shielded Arc Welding, Oxy Fuel Cutting & Plasma Cutting*, PDF Conceptual Design & Marketing, 3rd edition.
32. Kumar R. R. (2021), *Manufacturing Technology*, Jyothis Publishers, INDIA.
33. Islak S., Buytoz S., and Karagöz M. (2012), *Microstructural development on AISI 1060 steel by FeW/B4C composite coating produced by using tungsten inert gas (TIG) process*, Indian Journal of Engineering and Materials Sciences, 19(4):253.
34. Ulutan M., Yildirim M. M., Buytoz S. and Celik O. N. (2010), *Microstructure and wear behavior of TIG surface-alloyed AISI 4140 steel*, Tribology Transactions, 54(1):67-79.
35. Cheng F., Lo K., and Man H. (2003), *NiTi cladding on stainless steel by TIG surfacing process Part II. Corrosion behavior*, Surface and Coatings Technology, 172(2):316-321.

36. Emamian A., Corbin S. F., and Khajepour A. (2011), *The influence of combined laser parameters on in-situ formed TiC morphology during laser cladding*, Surface and Coatings Technology, 206(1):124-131.
37. Cheng F., Lo K., and Man H. (2003), *NiTi cladding on stainless steel by TIG surfacing process: Part I. Cavitation erosion behavior*, Surface and Coatings Technology, 172(2):308-315.
38. Buytoz S., Yildirim M. M., and Eren H. (2005), *Microstructural and microhardness characteristics of gas tungsten are synthesized Fe–Cr–C coating on AISI 4340*, Materials Letters, 59(6):607-614.
39. Chen J. H., Chen P. N., Lin C. M., Chang C. M., Chang Y. Y. and Wu W. (2009), *Characterization of multi-element alloy claddings manufactured by the tungsten inert gas process*, Surface and Coatings Technology, 203(20):2983-2988.
40. Mridha S. and Baker T. (2015), *Overlapping tracks processed by TIG melting TiC preplaced powder on low alloy steel surfaces*, Materials Science and Technology, 31(3):337-343.
41. Wang X. H., Zhang M., Zou Z. D., Song S. L., Han F. and Qu S. Y. (2006), *In situ production of Fe–TiC surface composite coatings by tungsten-inert gas heat source*, Surface and Coatings Technology, 200(20):6117-6122.
42. Emamian A., Corbin S. F. and Khajepour A. (2012), *Tribology characteristics of in-situ laser deposition of Fe-TiC*, Surface and Coatings Technology, 206(22):4495-4501.
43. Yan H., Zhang P., Yu Z., Lu Q. Yang S. and Li C. (2012), *Microstructure and tribological properties of laser-clad Ni–Cr/TiB2 composite coatings on copper with the addition of CaF2*, Surface and Coatings Technology, 206(19-20):4046-4053.
44. Berger L. (2015), *Application of hardmetals as thermal spray coatings*, International Journal of Refractory Metals and Hard Materials, Vol. 49, pp. 350-364.
45. Acker K. V., Vanhoyweghen D., Persoons R. and Vangrunderbeek J. (2005), *Influence of tungsten carbide particle size and distribution on the wear resistance of laser clad WC/Ni coatings*, Wear, Vol. 258, pp. 194-202.
46. Ghaziof S. and Gao W. (2015), *Zn–Ni–Al_2O_3 nano-composite coatings prepared by sol-enhanced electroplating*, Applied Surface Science, Vol. 351, pp. 869-879.
47. Mousavi-Anijdan S. H., Sabzi M., Ghobeiti-Hasab M. and Roshan-Ghiyas A. (2018), *Optimization of spot welding process parameters in dissimilar joint of dual phase steel DP600 and AISI 304 stainless steel to achieve the highest level of shear-tensile strength*, Materials Science & Engineering A, Vol. 726, pp. 120–125.

48. Chen W., Wang L. and Gao W. (2012), *Synthesis of Zn–Bi nano-composite coatings by an ionic co-discharge process*, Chemical Engineering Journal, Vol. 192, pp. 242-245.
49. Wang S. and Wei W. J. (2003), *Kinetics of electroplating process of nano-sized ceramic particle/Ni composite, Materials Chemistry and Physics*, 78(3):574-580.
50. Lin Y. C. and Chang K. Y. (2010), *Elucidating the microstructure and wear behavior of tungsten carbide multi-pass cladding on AISI 1050 steel*, J. Mater. Process Technol., Vol. 210, pp. 219–225.
51. Lou D., Hellman J., Luhulima D., Liimatainen J. and Lindroos, V. K. (2003), *Interactions between tungsten carbide (WC) particulates and metal matrix in WC-reinforced composites*. Mater. Sci. Eng. A Struct., Vol. 340, pp. 155–162.
52. Wu P., Du H. M., Chen X. L., Li Z. Q., Bai H. L.and Jiang E. Y. (2004), *Influence of WC particle behavior on the wear resistance properties of Ni WC composite coatings*, Wear, Vol. 257, pp. 142–147.
53. Huang S. W., Nolan D., Brandt M. (2003), *Pre-placed WC/Ni clad layers produced with a pulsed Nd:YAG laser via optical fibres*, Surface and Coatings Technology, Vol. 165, pp. 26-34.
54. Shu D., Li Z., Zhang K., Yao C., Li D., Yuan Y. and Dai Z. (2016), *Phase constituents and growth mechanism of laser in situ synthesized WC reinforced composite coating with W–C–Ni system*, Journal of Materials Research, 32(3):557-565.
55. Zangeneh S., Lashgari H. R., Lopez H. F. and Farahani H. K. (2017), *Microstructural characterization of TIG surface treating in Co-Cr-Mo-C alloy*, Materials Characterization, Vol. 132, pp. 223-229.
56. Sabzi M. and Dezfuli S. M. (2018), *Drastic improvement in mechanical properties and weldability of 316L stainless steel weld joints by using electromagnetic vibration during GTAW process*, Journal of Manufacturing Processes, Vol. 33, pp. 74-85.
57. Hong C., Gu D., Dai D., Cao S., Alkhayat M., Jia Q., Gasser A., Weisheit A., Kelbassa I., Zhong M. and Poprawe R. (2015), *High-temperature oxidation performance and its mechanism of TiC/Inconel 625 composites prepared by laser metal deposition additive manufacturing*, Journal of Laser Applications, 27, S17005.
58. Tavoosi M. and Arjmand S. (2017), *In situ formation of Al/Al3Ti composite coating on pure Ti surface by TIG surfacing process*, Surfaces and Interfaces, Vol. 8, pp. 1-7.
59. Mousavi-Anijdan S. H. and Sabzi M. (2018), *The evolution of microstructure of an high Ni HSLA X100 forged steel slab by thermo-mechanical controlled processing*, Proceeding of the TMS Annual Meeting & Exhibition, pp. 145–156.

60. Kumar S., Ghosh P. K. and Kumar R. (2017), *Surface modification of AISI 4340 steel by multipass TIG arcing process*, Journal of Materials Processing Technology, Vol. 249, pp. 394-406.
61. Lailatul P. H. and Maleque M. A. (2017), *Surface Modification of Duplex Stainless Steel with SiC Preplacement Using TIG Torch Cladding*, Procedia Engineering, Vol. 184, pp. 737-742.
62. Kumar R., Ghosh P. K. and Kumar S. (2017), *Thermal and metallurgical characteristics of surface modification of AISI 8620 steel produced by TIG arcing process*, Journal of Materials Processing Technology, Vol. 240, pp. 420-431.
63. Ghadami F., Sohi M. H. and Ghadami S. (2015), *Effect of TIG surface melting on structure and wear properties of air plasma-sprayed WC–Co coatings*, Surface and Coatings Technology, Vol. 261, pp. 108-113.
64. Çelik O. N., Ulutan M., Gaşan H., Er Ü. and Buytoz S. (2011), *Effects of graphite content on the microstructure and wear properties of an AISI 8620 steel surface modified by tungsten inert gas (TIG)*, Surface and Coatings Technology, 206(6),1423-1429.
65. Cheng F. T., Lo K. H. and Man H. C. (2003), *NiTi cladding on stainless steel by TIG surfacing process: Part I. Cavitation erosion behavior*, Surface and Coatings Technology, 172(2–3),308-315.
66. Tosun G. (2014), *Ni–WC Coating on AISI 1010 Steel Using TIG: Microstructure and Microhardness,* Arab J Sci Eng, Vol. 39, pp. 2097–2106.
67. Sabzi M., Dezfuli S. M. and Far S. M. (2018), *Deposition of Ni-tungsten carbide nanocomposite coating by TIG welding: characterization and control of microstructure and wear/corrosion responses*, Ceramics International, 44(18):22816-22829.
68. Rasool G. and Stack M. M. (2014), *Wear maps for TiC composite based coatings deposited on 303 stainless steel*, Tribology International, Vol. 74, pp. 93–102.
69. Man H. C., Zhang S., Cheng F. T. and Yue T. M. (2002), *In situ synthesis of TiC reinforced surface MMC on Al6061 by laser surface alloying*, Scripta Materialia, 46(3):229–234.
70. Nowotny S., Berger L. M. and Spatzier J. (2014), *Coatings by laser cladding*, In: Sarin V. K., Mari D. and Llanes L. (Eds.), Comprehensive Hard Materials, Elsevier Ltd., pp.507–525.
71. Pawlowski L. (1999), *Thick laser coatings: a review*, Journal of Thermal Spray Technology, Vol. 8, pp. 279–295.
72. Paul C.P., Mishra S. K., Tiwari P. and Kukreja L. M. (2013), *Solid-Particle Erosion Behaviour of WC/Ni Composite Clad layers with Different Contents of WC Particles*, Optics & Laser Technology, Vol. 50, pp. 155–162.

73. Zhang J., Wu G., Yao J. and Wang Y. (2016), *Microstructure evolution and wear resistance of Ni-coated WC composite coating fabricated by laser cladding*, Laser Institute of America, Vol. 510.
74. Cui C., Guo Z., Wang H. and Hu J. (2007), *In situ TiC particles reinforced grey cast iron composite fabricated by laser cladding of Ni–Ti–C system*, Journal of Materials Processing Technology, 183(2-3):380–385.
75. Viswanathan A., Sastikumar D., Kamachimudali U., Kumar H. and Nath A.K. (2007), *TiC reinforced composite layer formation on Al–Si alloy by laser processing*, Surface Engineering, 23(2):123-128.
76. Lancaster J. F. (1980), *Metallurgy of Welding*, 3rd ed. (Allen and Unwin, London UK).
77. Ma H., Li Y. and Wang J. (2006), *Analysis of the microstructure of Cr–Ni surface layers deposited on Fe3Al by TIG*, Materials Characterization, 57(4–5):419-423.
78. Benyounis K. Y., Fakron O. M. A., Abboud J. H., Olabi A. G. and Hashmi M. J. S. (2005), *Surface melting of nodular cast iron by Nd-YAG laser and TIG*, Journal of Materials Processing Technology, 170(1-2):127-132.
79. Tijo D., Masanta M. and Kumar Das A. (2018), *In-situ TiC-TiB2 coating on Ti-6Al-4V alloy by tungsten inert gas (TIG) cladding method: Part-I. Microstructure evolution*, Surface and Coatings Technology, Vol. 344, pp. 541-552.
80. Saroj S., Kumar Sahoo C., Tijo D., Kumar K. and Masanta M. (2017), *Sliding abrasive wear characteristic of TIG cladded TiC reinforced Inconel825 composite coating*, International Journal of Refractory Metals and Hard Materials, Vol. 69, pp. 119-130.
81. Harsha S., Dwivedi D. K. and Agarwal A. (2008), *Influence of CrC addition in Ni–Cr–Si–B flame sprayed coatings on microstructure*, microhardness and wear behaviour. Int. J. Adv. Manuf. Tech. Vol. 38, pp. 93–101.
82. Sahoo C.K. and Masanta M. (2015), *Effect of pulse laser parameters on TiC reinforced AISI 304 stainless steel composite coating by laser surface engineering process*, Optics and Lasers in Engineering, Vol. 67, pp. 36-48.
83. Eroglu M., Aksoy M. and Orhan N. (1999), *Effect of coarse initial grain size on microstructure and mechanical properties of weld metal and HAZ of a low carbon steel*, Mater. Sci. Eng. A Struct., Vol. 269, pp. 59-66.
84. Gural A., Bostan B. and Ozdemir A. T. (2007), *Heat treatment in two phase region and its effect on microstructure and mechanical strength after welding of a low carbon steel*, Mater. Design, Vol. 28, pp. 897-903.
85. Surender M., Basu B. and Balasubramaniam R. (2004), *Wear characterization of electrodeposited Ni–WC composite coatings*, Tribol. Int. Vol. 37, pp. 743-749.

86. Hyung K. J., Goun J. H. and Yong L. K. (2015), *Simulation of solid particle erosion in WCNi coated wall using CFD*, Journal of Materials Processing Technology, Vol. 224, pp. 240-245.
87. Hefnawy A., Elkhoshkhany N. and Essam A. (2018), *Ni–TiN and Ni-Co-TiN composite coatings for corrosion protection: Fabrication and electrochemical characterization*, Journal of Alloys and Compounds, Vol. 735, pp. 600-606.
88. Balu P., Kong F., Hamid S. and Kovacevic R. (2013), *Finite element modeling of solid particle erosion in AISI 4140 steel and nickel–tungsten carbide composite material produced by the laser-based powder deposition process*, Tribology International, Vol. 62, pp. 18-28.
89. Stack M. M. and Peña D. (2001), *Mapping erosion of Ni–Cr/WC-based composites at elevated temperatures: some recent advances*, Wear, 251(1-12):1433-1443.
90. Tam K. F., Cheng F. T. and Man H. C. (2002), *Cavitation erosion behavior of laser-clad Ni–Cr–Fe–WC on brass*, Materials Research Bulletin, 37(7):1341-1351.
91. Zhang D. and Zhang X. (2005), *Laser cladding of stainless steel with Ni–Cr3C2 and Ni-WC for improving erosive–corrosive wear performance*, Surface and Coatings Technology, 190(2–3):212-217.
92. Yuan J., Zhu Y., Zheng X., Ji H. and Yang T. (2011), *Fabrication and evaluation of atmospheric plasma spraying WC-Co-Cu-MoS2 composite coatings*, J. Alloys Comp, Vol. 509, pp. 2576-2581.
93. Wan W., Xiong J. and Liang M. (2017), *Effects of secondary carbides on the microstructure, mechanical properties and erosive wear of Ti(C,N)-based cermets*, Ceramics International,43(1), Part B:944-952.
94. Shatov A. V., Ponomarev S. S. and Firstov S. A. (2008), *Fracture of WC–Ni cemented carbides with different shape of WC crystals*, International J. of Refractory Metals and Hard Materials, 26(2):68-76.
95. Hussainova I., Antonov M. and Zikin A. (2012), *Erosive wear of advanced composites based on WC*, Tribology International, 46(1):254-260.
96. Sahoo C.K. and Masanta M. (2017), *Microstructure and mechanical properties of TiC-Ni coating onAISI304 steel produced by TIG cladding process*, Journal of Materials Processing Technology, Vol. 240, pp. 126-137.
97. Technical committee, Indian institute of Welding, Bangalore branch (1977), *Welding Metallurgy, technology and quality assurance*, Venue: Bangalore.
98. Amani J. (2011), *Effect of Submerged Arc Welding Parameters on the Microstructure of SA516 and A709 Steel Welds.*
99. د .عبد الرزاق اسماعيل خضر و د.نوفل محمد حسين (1993)، تكنولوجيا اللحام، الجامعة التكنولوجية.

100. Kuppan T. (2000), *Heat Exchanger Design Handbook*, Marcel Dekker, Inc.
101. Zhong M., Liu W., Chen Y., Sun H. and Zhang Y. (2004), *Synthesizing of WC/Ni hard alloy coating by laser cladding with powder feeding and the growth morphology of WC crystals*, Laser Institute of America, China.
102. Wan D., Liu H., Hu D. and Cai L. (2007), *Morphology and mechanical characteristics of pulse laser coating texturing WC-Ni alloying layers*, School of Mechanical and Power Engineering, China.
103. Paul C.P, Mishra S.K., Tiwari P., Kukreja L.M. (2013), *Solid-Particle Erosion Behavior of WC/Ni Composite Clad layers with Different Contents of WC Particles*, Optics & Laser Technology, INDIA.
104. http://bbnsteelplate.com/news/astm-a36-steel-equivalent-indian-standardis-is2062_928.html.
105. Jordan L. and Swanger W. H. (1980), *The properties of pure nickel*, Bureau of standards. J Res. doi, 10, 6028.
106. Rajesh K. R. (2016), *Basics of Mechanical Engineering*, 2nd ed., Juthis Puplishers, India.
107. Brandt M., Huang S. W. and Samandi M. (2003), *Deposition of WC/Ni clad layers with a pulsed Nd:YAG laser*, Journal of Laser Applications, 15(1):31-36.
108. Xu J. S., Zhang X. C., Xuan F. Z., Tian F., Wang Z. D. and Tu S. T. (2013), *Tensile properties and fracture behavior of laser cladded WC/Ni composite coatings with different contents of WC particle studied by in-situ tensile testing*, Materials Science and Engineering A Vol. 560, pp.744–751.
109. Xu J. S., Zhang X. C., Xuan F. Z., Wang Z. D. and Tu S. T. (2012), *Microstructure and Sliding Wear Resistance of Laser Cladded WC/Ni Composite Coatings with Different Contents of WC Particle*, JMEPEG, Vol. 21, pp. 1904–1911.
110. Weng Z., Wang A., Wu X., Wang Y. and Yang Z. (2016), *Wear resistance of diode laser-clad Ni/WC composite coatings at different temperatures*, Surface and Coatings Technology, Vol. 304, pp. 283–292.
111. Guo C., Chen J., Zhou J., Zhao J. and Wang L. (2012), *Effects of WC–Ni content on microstructure and wear resistance of laser cladding Ni-based alloys coating*, Surface and Coatings Technology, Vol. 206, pp. 2064–2071.
112. Bansal A., Zafar S. and Sharma A. K. (2015), *Microstructure and Abrasive Wear Performance of Ni-WC Composite Microwave Clad*, JMEPEG, Vol. 24, pp. 3708‑3716.
113. Tehrani H. M., Shoja-Razavi R., Erfanmanesh M., Hashemi S. H. and Barekat M. (2020), *Evaluation of the mechanical properties of WC-Ni composite coating on an AISI 321 steel substrate*, Optics and Laser Technology, Vol. 127, pp. 1-16.

114. Yuan Z. X. Yu Z. -S. Tan P. and Song S. -H. (1999), *Effect of rare earths on the carburization of steel*, Materials Science and Engineering: A, 267(1):162-166.
115. Wang K. L., Zhang Q. B., Sun M. L. Wei X. G. and Zhu Y. M. (2001), *Rare earth elements modification of laser-clad nickel-based alloy coatings*, Applied Surface Science, 174(3–4):191-200.
116. Farahmand P., Liu S., Zhang Z. and Kovacevic R. (2014), *Laser cladding assisted by induction heating of Ni–WC composite enhanced by nano-WC and La_2O_3*, Ceramics International, 40(10):15421-15438.
117. Eroglu M. and Ozdemir N. (2002), *Tungsten-inert gas surface alloying of a low carbon steel*, Surf. Coat. Technol. Vol. 154, pp. 209–217.
118. Li Y., Bai P., Wang Y., Hu J. and Guo Z. (2009), *Effect of TiC content on Ni/Ti Ccomposites by direct laser fabrication*. Materials and Design, 30(9):1409–1412.
119. Sahoo C.K. and Masanta M. (2017), *Microstructure and mechanical properties of TiC-Ni coating onAISI304 steel produced by TIG cladding process*, Journal of Materials Processing Technology, Vol. 240, pp. 126-137.
120. Yi D., Yu P., Hu B., Liu H., Wang B. and Jiang Y. (2013), *Preparation of nickel-coated titanium carbide particulates and their use in the production of reinforced iron matrix composites*. Materials and Design, Vol. 52, pp. 572–579.
121. Peng D.-X., Kang Y. and Huang Y.-J. (2014), *Microstructure and tribological propertiesof gas tungsten arc clad TiC composite coatings on carbon steel*, Industrial Lubrication and Tribology, 66(5): p. 609–617.
122. Rasool G. and Stack M.M. (2014), *Wear maps for TiC composite based coatings deposited on 303 stainless steel*, Tribology International, Vol. 74, pp. 93–102.
123. Desale G.R., Paul C.P., Gandhi B.K. and Jain S.C. (2009), *Erosion wear behavior of laser clad surfaces of low carbon austenitic steel*, Wear, 266(9-10): p. 975–987.
124. Yazdi R. and Kashani-Bozorg S.F. (2015), *Microstructure and wear of in-situTi/(TiN+TiB) hybrid composite layers produced using liquid phase process*, Materials Chemistry and Physics, Vol. 152, pp.147–157.
125. Liu Y.H., Li J. and Xuan F.Z. (2012), *Fabrication of TiC reinforced Ni based coating by laser cladding*, Surface Engineering, 28(8): p. 560-563.
126. Zhu Y. C., Yukimura K., Ding C. X. and Zhang P. Y. (2011), *Tribological properties of nanostructured and conventional WC-Co coatings deposited by plasma spraying*, Thin Solid Films, Vol. 388, pp. 277-282.

Appendix A

35-0772 Quality: *
CAS Number: 61027-57-4
Molecular Weight: 179.55
Volume[CD]: 155.38
Dx: 7.675 Dm:
S.G.: Pnma (62)
Cell Parameters:
a 5.091 b 6.743 c 4.526
α β γ
SS/FOM: F30=154(.0052, 37)
I/Icor:
Rad: CuKa1
Lambda: 1.5405981
Filter: Graph
d-sp: diffractometer
Mineral Name:
Cohenite, syn

Fe3 C
Iron Carbide
Ref: Natl. Bur. Stand. (U.S.) Monogr. 25, 21, 72 (1985)

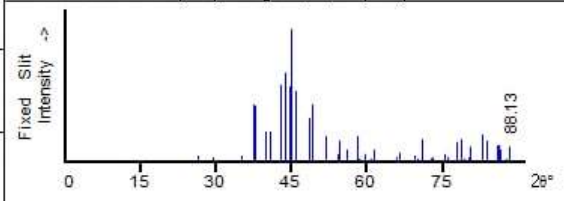

2θ	int-f	h	k	l	2θ	int-f	h	k	l	2θ	int-f	h	k	l
26.410	4	0	2	0	54.398	15	2	3	0	75.889	3	0	3	3
29.513	3	1	1	1	56.004	8	2	1	2	77.901	14	4	0	1
35.233	4	2	0	0	57.992	19	3	0	1	78.592	16	1	3	3
37.633	43	1	2	1	58.398	2	2	3	1	79.436	2	4	1	1
37.743	41	2	1	0	59.744	5	3	1	1	80.349	3	2	4	2
39.798	22	0	0	2	60.824	2	1	3	2	80.533	11	2	5	0
40.632	22	2	0	1	61.260	8	2	2	2	83.023	20	3	3	2
42.879	57	2	1	1	61.423	6	1	4	1	83.547	1	3	4	1
43.742	67	1	0	2	64.816	1	3	2	1	83.892	15	2	5	1
44.569	56	2	2	0	66.001	3	1	1	3	85.806	6	0	0	4
44.992	100	0	3	1	66.457	6	2	4	0	85.982	12	1	5	2
45.861	53	1	1	2	69.501	4	2	3	2	86.179	12	3	0	3
48.398	5	0	2	2	70.020	2	2	4	1	86.537	9	0	6	0
48.588	32	1	3	1	70.824	17	1	2	3	87.682	2	3	1	3
49.115	43	2	2	1	72.813	2	2	0	3	88.129	11	4	3	0
51.813	19	1	2	2	73.147	3	0	5	1					
54.184	5	2	0	2	75.420	5	3	2	2					

25-1047 Quality: *
CAS Number: 12070-12-1
Molecular Weight: 195.86
Volume[CD]: 20.76
Dx: 15.669 Dm:
S.G.: P$\bar{6}$m2 (187)
Cell Parameters:
a 2.906 b c 2.837
α β γ
SS/FOM: F14=29(0.035, 14)
I/Icor:
Rad: CuKa1
Lambda: 1.54056
Filter:
d-sp:
Mineral Name:
Unnamed mineral, syn [NR]

W C
Tungsten Carbide
Ref: Bind, McCarthy, G., Penn State Univ, University Park, PA, USA, ICDD Grant-in-Aid, (1973)

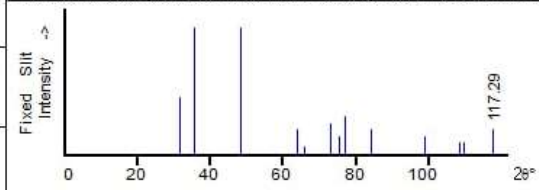

2θ	int-f	h	k	l	2θ	int-f	h	k	l	2θ	int-f	h	k	l
31.474	45	0	0	1	73.064	25	1	1	1	108.18	10	2	1	0
35.626	100	1	0	0	75.442	14	2	0	0	109.02	1	0	0	3
48.266	100	1	0	1	77.101	30	1	0	2	109.71	10	2	0	2
63.979	20	1	1	0	84.015	20	2	0	1	117.29	20	2	1	1
65.701	6	0	0	2	98.734	14	1	1	2					

23-0297 Quality:
CAS Number:
Molecular Weight: 56.93
Volume[CD]: 46.50
Dx: 8.132 Dm: 7.800
S.G.: Fm3m (225)
Cell Parameters:
a 3.596 b c
α β γ
SS/FOM: F 5=7(0.138, 5)
I/Icor:
Rad: CoKa
Lambda: 1.7902
Filter:
d-sp:
Mineral Name:
Taenite

(Fe , Ni)
Iron Nickel
Ref: Goldschmidt, Metallurgia, 40, 103 (1949)

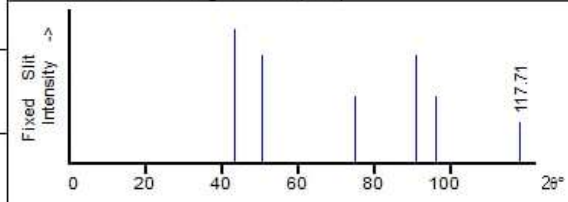

2θ	int-f	h	k	l	2θ	int-f	h	k	l	2θ	int-f	h	k	l
43.472	100	1	1	1	74.677	50	2	2	0	95.940	50	2	2	2
50.673	80	2	0	0	90.673	80	3	1	1	117.71	30			

ملخص البحث

أصبحت معالجة أسطح السبائك الفولاذية في الوقت الحاضر ضرورة في المجالات العلمية والصناعية، وتعتبر التكسية بأستخدام قوس التنكستن المحمي بالغاز الخامل (TIG) إحدى الطرق الفعالة لمعالجة أسطح هذه السبائك. تهدف هذه الدراسة إلى تقصي تأثير الطلاءات المركبة من كربيد التنكستن والنيكل (WC–Ni) المترسبة باستخدام تكسية TIG على خصائص سطح الركائز الفولاذية المنخفضة السبائك. تهدف الدراسة الحالية أيضًا إلى استكشاف تأثير النسبة الوزنية من كربيد التنكستن في الطلاءات المركبة WC–Ni، ومدخلات الحرارة المقابلة لشدة تيار تكسية TIG على هذه الخصائص. تم استخدام عجينة مركبة مجهزة مسبقا بسمك 1 ملم و بنسب وزنية مختلفة من WC (30، 40، 50، 60 و 70٪) لترسيب طبقات الطلاء باستخدام قيم تيار مختلفة (80، 120، 130، 140 أمبير). كشفت النتائج عن ترابط بيني متميز بين طبقة الطلاء والركيزة في جميع العينات المطلية باستثناء تلك التي أظهرت طبقة تكسية مدمرة ناتجة عن ترسيب مادة مركبة من 70٪ WC مع النيكل باستخدام تيار مقداره 80 أمبير. كانت المناطق المعيوبة صغيرة مقارنة بالمقاطع العرضية الكاملة لطبقات التكسية. أظهر فحص المجهر الضوئي و الماسح الإلكتروني العديد من البنى المجهرية المختلفة عبر طبقات التكسية، معظمها شجيرات محلول جامد من النيكل مع جسيمات WC موزعة داخل الارضية. استنادًا إلى معدلات التبريد وكثافة WC في المادة المركبة، كانت الشجيرات في المواقع المختلفة عبر طبقات التكسية قليلة أو كثيفة، أنعم أو اخشن، متساوية المحاور أو طولية، متفرعة بكثافة أو أقل كثافة. بالإضافة إلى الحبيبات الطولية الكبيرة، كانت الحبيبات الصغيرة جدا عند السطح البيني سائدة على جوانب الطلاء. كما ظهرت جسيمات كبيرة الحجم نسبيًا من WC والتي بقيت سليمة دون تحلل موزعة بصورة غير متجانسة داخل ارضية بعض طبقات التكسية. ومع ذلك، فإن زيادة شدة تيار التكسية لم تكن كافية لتحلل WC. أثبت التحليل

الطيفي المشتت للطاقة أن عنصر الحديد الذي تم انحلاله من مادة الركيزة إلى البركة المنصهرة كان يتركز بشكل أساسي في الارضية بدلاً من الشجيرات، بينما يشير توزيع عنصر W بوضوح إلى مواقع واتجاهات الشجيرات.

زادت صلادة فيكرز المجهرية بشكل ملحوظ مع زيادة محتوى WC في مركب طبقة الطلاء. أعلى قيمة صلادة كمعدل كانت HV756 وهي لطبقة الطلاء المترسبة بنسبة وزنية مقدارها 60٪ من WC في المركب وبتيار مقداره A120، أي حوالي 2.9 مرة من صلادة مادة الركيزة. زيادة قيم التيار إلى A130 و A140 لطبقات الطلاء المترسبة بنسبة 70٪ WC أدت إلى زيادة الصلادة إلى حد ما، بينما زادت الصلادة بشكل ملحوظ إلى HV850 مع تقليل التيار إلى A80. لم تكن زيادة الصلادة في منطقة ما مترافقة بالضرورة مع انخفاض معدل فقدان الوزن أثناء البلى في تلك المنطقة. تؤدي زيادة النسبة الوزنية من WC في طبقات الطلاء بشكل عام إلى انخفاض معدل فقدان الوزن وبالتالي زيادة مقاومة البلى. أدت زيادة قيمة التيار إلى A130 و A140 لطبقة الطلاء المترسبة بنسبة 70٪ من WC إلى تقليل معدل فقدان الوزن (9.5×10^{-6} و 6.4×10^{-6} g/m على التوالي). انخفاضا ملحوظا في معدل فقدان الوزن كان نتيجة لتقليل شدة تيار تكسية TIG إلى A80 (مع 70٪ نسبة وزنية من WC) ، وهو في العينة التي أظهرت طبقة طلاء مدمرة وترابطًا بينيًا غير مناسب إلى حد ما مع الركيزة. عموما، فقد انخفض فقدان الوزن في الغالب مع زيادة مسافة انزلاق اختبار البلى.

وزارة التعليم العالي والبحث العلمي
جـــــامـــعـــة بـــابـــــل
كـــلـــيـــة هـــنـــدســة الـمـواد
قـســم هـــنـــدســة الـــمـعـــادن

التكسية الصلدة للفولاذ الواطئ السبائكي بالمادة المركبة تنكستن–نيكل بأستخدام قوس التنكستن الكهربائي المحمي بالغاز الخامل

رسالة مقدمة إلى

قسم هندسة المعادن في كلية هندسة المواد/جامعة بابل وهي
جزء من متطلبات نيل شهادة الماجستير في هندسة المواد/هندسة المعادن

من قبل

حوراء نجم عبدعون مجيد

بإشـــــراف

أ.م.د. عبد السميع جاسم عبد الزهرة الكلابي

1444 هـ 2023 م